Discontinuous Galerkin Modeling of Wave Propagation in Damaged Materials

Quriaky Gomez Carrero

UNIVERSITÉ PARIS 13 - SORBONNE PARIS CITE

THÈSE

pour obtenir le grade de

DOCTEUR DE L'UNIVERSITÉ PARIS 13

Spécialité: Mécanique des Matériaux

Préparée au **Laboratoire des Sciences et des Procédés de Matériaux**

Dans le cadre de l'**Ecole Doctorale Galilée**

par

Quriaky GOMEZ

Présentée et soutenue publiquement le21 juin 2017

Discontinuous Galerkin Modeling of Wave Propagation in Damaged Materials

JURY

M.	PICU Catalin	Professeur, Rensselaer Polytechnic Institute	Rapporteur
M.	UENISHI Koji	Professeur, Tokyo University	Rapporteur
M.	CAMPILLO Michel	Professeur, Université de Grenoble-Alpes	Président
M.	ERZAR Benjamin	Chercheur, CEA Gramat	Examinateur
M.	JIA Xiaoping	Professeur, Université Paris Est	Examinateur
M.	LI Jia	Professeur, Université Paris 13	Examinateur
M	IONESCU Ioan	Professeur, Université Paris 13	Directeur de thèse

Abstract

A discontinuous Galerkin (DG) technique for modeling wave propagation in damaged (brittle) materials is developed in this thesis. This subject is of great interest in dynamics of materials or in solid Earth geophysics. The numerical approach of this thesis will be related only to the DG method but there are two different types of mechanical models for describing the damaged materials which are considered. In the first one, called "micro-mechanics based damage model" and studied in the first part of the thesis, the micro-cracks are introduced through a damage parameter (crack density parameter) which can increase under the loading wave. The heterogeneity is a material one (the mechanical model loses its isotropy and homogeneity but the geometric homogeneity is preserved). In the second one, called the "cracked solid" or "cracked material" studied in the second part of this thesis, the micro-cracks, describing the damage of the material, are introduced as a "geometric heterogeneity" in an isotropic and homogeneous elastic solid. This geometric heterogeneity induces a loss of both (global) isotropy and (global) homogeneity of the elastic solid. The two models are diametral opposite but they show like a mirror of the physical reality, where both geometric and material heterogeneities are present.

In the first part is analyzed the coupling between the damage evolution and the wave propagation. Since the loading wave, propagating into the material, produces damage and changes the propagation properties of the material, the mechanical damage processes cannot be separated from the wave propagation process. The (local) damage model for brittle materials used in this part is rather general and covers a wide spectrum of the micro-mechanics-based damage models. Stability criteria for dynamic and quasi-static processes point out that for a given continuous strain history the quasi-static or dynamic problems are unstable or ill-posed (multiplicity of material responses) and whatever the selection rule is adopted, shocks (time discontinuities) will occur. A critical crack density parameter, which distinguishes between stable and unstable behaviors, is computed.

For homogeneous strain-driven processes at intermediate and low rates of deformation, sharp stress drops related to the material instabilities could be expected. On the contrary, for high rates of deformation, the strain-stress curve depends strongly on the rate of deformation but only a smooth stress drop is expected.

A new numerical scheme associated to the boundary value problem of the wave propagation was proposed. To solve the associated nonlinear hyperbolic problem an explicit leapfrog type scheme for the time discretization was used. To capture the instabilities a semi-implicit Euler method and a micro-scale time step were used. A DG method with a centered flux choice was considered for the spatial discretization. To test the numerical scheme a new (nontrivial) analytical solutions for a 1-D problem was constructed. Using the exact solution the accuracy of the numerical scheme and its time step/mesh size sensitivity has been analyzed. The centered scheme flux choice works well as far as the macro-scale solution is smooth and the dynamic processes (at the microscopic scale) are very well approximated. For quasi-static processes (at the microscopic scale), the solution exhibits shocks and a specific shock capturing flux choice have to be used.

Numerical tests showed that the one dimensional stress pulse is flatter (larger length and smaller amplitude) when the flaw density increases while the length of the pulse is less affected by the initial crack length. In the anti-plane configuration, in the direction of the micro-cracks the material is hardly damaged and the

initial circular wave is propagating much slower than in the orthogonal direction. Even if the cracks' systems have different orientations, the final snapshot still shows an important anisotropy. For isotropic loadings, the choice of only three directions with the same initial properties, ensures an isotropic damage behavior.

Numerical tests for the blast wave propagation illustrated the role played by the micro-cracks orientation. The friction in the damage model has also a non-negligible influence on the amplitude and on the speed of the loading wave. If several orientations of the micro-cracks are considered an additive effect of the damage is present without an important interplay between the micro-cracks families.

In the second part of the thesis the wave propagation in (damaged) materials with a nonlinear micro-structure (micro-cracks in frictional contact) was investigated. The numerical scheme developed here makes use of the explicit leapfrog scheme in time and a centered flux choice for the inner element face. The nonlinear conditions on the micro-cracks are treated by using an augmented Lagrangian technique, with a reasonable additional computational cost.

This technique was used to compare the effective wave velocity in a damaged material obtained by direct DG computation and by the analytical formula, deduced form the effective elasticity of a cracked solid theory. The over-all wave speed is slower than the theoretical speed and the difference is very important for large values of the crack density parameter. If the wave length is of order of the crack length, the wave speed is strongly dependent on wavelength, but for a large wavelength the wave speed depends only on the crack density parameter.

Finally, to illustrate the numerical scheme the wave generated by a blast in a cracked material was analyzed. The crack orientation affects the wave propagation and its scattering. The friction phenomena between the faces of the micro-cracks are affecting the wave propagation only for the mode II behavior.

Notations

General Notations

a : scalar variable

$\boldsymbol{a}$: vector/tensor variable

$\boldsymbol{n}$: external unit normal

$a_n = \boldsymbol{a} \cdot \boldsymbol{n}$ normal component of vector $\boldsymbol{a}$

$\sigma_n = \sigma\boldsymbol{n} \cdot \boldsymbol{n}$ normal component ofstress vector $\boldsymbol{\sigma n}$

$\boldsymbol{a}_T = \boldsymbol{a} - a_n\boldsymbol{n}$ tangential component of vector $\boldsymbol{a}$

$\boldsymbol{\sigma}_T = \boldsymbol{\sigma n} - \sigma_n\boldsymbol{n}$ tangential component of stress vector $\boldsymbol{\sigma n}$

$\dot{\boldsymbol{a}}$ time derivative of $\boldsymbol{a}$

$\boldsymbol{a} \cdot \boldsymbol{b} = a_i b_i$ scalar product of vectors $\boldsymbol{a}, \boldsymbol{b}$

$\boldsymbol{A} : \boldsymbol{B} = A_{ij}B_{ij}$ scalar product of two tensors $\boldsymbol{A}, \boldsymbol{B}$

Domain

$\mathcal{D}$: domain in $\mathbb{R}^3$

Ω domain in $\mathbb{R}^2$

$\partial\mathcal{D}$: domain boundary

Σ : internal boundary

Σ_v : part of the external boundary where velocity condition is imposed

Σ_σ : part of the external boundary where stress condition is imposed

Dynamic Model

$\boldsymbol{u}$: displacement

$\boldsymbol{v}$: velocity

$\boldsymbol{\varepsilon} = \boldsymbol{\varepsilon}(\boldsymbol{u}) = \frac{1}{2}(\nabla\boldsymbol{u} + \nabla^t\boldsymbol{u})$: small deformation tensor

$\boldsymbol{\sigma}$: stress tensor

$\boldsymbol{b}$: mass forces

$\mathcal{E}$: Stiffness tensor

$\mathcal{A}$: Compliance tensor

c_P : P-wave velocity

c_S : S-wave velocity

c_0 : reference wave velocity

μ_f : friction coefficient

η : flaw density

ρ : crack density/ damage parameter

Material parameters

E : Young modulus

ν : Poison ratio

G : Shear modulus

λ, μ: Lamé coefficients

ρ^{mass} : mass density

Damage Evolution

τ : generic stress (one dimension)

τ^c : critical stress

γ : generic strain (one dimension)

γ^c : critical strain

l_i : radius (half length) for circular cracks of family i

l_i^0 : initial radius (half length) of family i

$\mathcal{K}_i$: damage criterion function of family i

$\mathcal{L}_i$: damage rate of family i

$K_d^I, K_d^{II}, K_d^{III}$: Dynamic stress intensity factor in different modes

K^I, K^{II}, K^{III} : Static stress intensity factor in different modes

K_c : Critical stress intensity factor

c_m : crack growth velocity

A_0, C : compliance coefficients

ρ^c : critical crack density parameter

l^c : critical micro-crack radius

M_Q: microscopic evolution index

M_Q^c : critical microscopic evolution index

Mathematical Functions

div : divergency

$\min(\cdot)$: minimum function

∇ : gradient

∇^t : transposed gradient

$[x] = x^+ - x^-$: jump of x

$[x]_- = (|x| - x)/2$: negative part of x

$[x]_+ = (x + |x|)/2$: positive part of x

Numerical Implementation

Δt : time step (macro-scale)

δt : time step (micro-scale)

$\mathcal{F}_v^k$: velocity flux

$\mathcal{F}_\sigma^{k-\frac{1}{2}}$: stress flux

Acrimonious

CFL: Courant-Friedrichs-Lewy condition

NIC: non interacting cracks scheme

DS: Differential scheme

SCS: Self consistent scheme

SIF: Stress intensity factor

CONTENTS

CHAPTER 1

GENERAL INTRODUCTION

Discontinuous Galerkin (DG) methods form a class of numerical techniques that can be considered as finite element methods supporting discontinuities in the test spaces. These methods can also be thought of as finite volume methods where the approximate solution is expressed by polynomial instead of constant functions. An overview of the principal mathematical aspects of DG methods can be found in the recent book of Ern [37]. In 1973 Reed and Hill [102] presented the first discontinuous Galerkin method in the framework of the hyperbolic neutron transport equation. The year after, Lesaint [77], Lesaint and Raviart [78] produced the first analysis for steady first order PDEs. Later, Chavent and Cockburn [26] expanded the method to time-dependent hyperbolic PDEs using the forward Euler scheme for time discretization. At the beginning of the 1970s, Nitsche introduced the Discontinuous Garlekin method to PDEs with diffusion using penalty methods [92]. Advances using this technique were done by Babuska [9], Babuska and Zlamal [10], Douglas and Dupont [39], Baker [11], Wheeler [124], and Arnold [4]. The implementation of numerical fluxes in the Discontinuous Garlerkin methods can be traced back to the late 1990s in the oeuvre of Bassi and Rebay on the Navier-Stokes equations [14] and of Cockburn and Shu on convection-diffusion systems [28]. A complete analysis of Discontinuous Galerkin methods for the elliptic equation is given in the paper of Arnold, Brezzi, Cockburn, and Marini [5].

Discontinuous Galerkin methods are associated to (nonlinear) initial and boundary value problems which develop discontinuities (in time and/or in space). Their solutions could have a complicated structure near such discontinuities. The numerical techniques for these

problems have to guarantee that the approximate solution is physically relevant and not to induce spurious oscillations. All these difficulties were successfully addressed during the remarkable development of the high-resolution finite difference and finite volume schemes for nonlinear hyperbolic systems by means of suitably defined numerical fluxes and slope limiters. Since DG methods assume discontinuous approximate solutions, they can be considered as generalizations of finite volume methods. As a consequence, the DG methods incorporate the ideas of numerical fluxes and slope limiters into the finite element frame-work.

One of the main advantages of the DG methods over classical finite volume and finite difference methods is that they are very well suited for handling complicated geometries and that they require an extremely simple treatment of the boundary conditions. Another advantage of the DG methods is that they can easily handle adaptivity strategies and that the degree of the approximating polynomial can be easily changed from one element to another. Finally DG methods of arbitrarily high formal order of accuracy can be obtained by suitably choosing the degree of the approximating polynomials and they are highly parallelizable.

The large majority of numerical schemes that treat wave propagation in complex media uses the finite-difference method (see for instance [121, 106, 105, 122, 54]). Nevertheless, FDMs suffer from some critical issues that are inherent to the underlying Cartesian grid, such as parasite diffractions in cases where the boundaries have a complex topography. That is why a lot of attention have been done in the last decade to the development of the DG techniques for the numerical techniques associated to elastodynamics and seismic wave propagation (see for instance [29, 18, 17, 30, 41, 40, 54, 71, 116, 46]).

The aim of this thesis is to develop a DG technique for modeling wave propagation in damaged (brittle) materials. This subject is of great interest in dynamics of materials or in solid Earth geophysics. Understanding the rock wave velocities variations is very important in extracting the information on the mechanical state of the rock from seismic and seismological data. In the oil industry, this has a direct bearings on the quantification of the oil content. In seismology, the mechanical properties of the surrounding rock of a fault can be associated to precursory phenomena (as earthquake nucleation) related to earthquakes predictability. On the other hand, it is of significant importance in dynamics of materials related to engineering and defense issues, the role played by the waves propagation associated to high rate loadings (blast, explosions, etc) in the stiffness reduction of elastic bodies, due to the development or presence of many disordered micro-cracks.

Even if the numerical approach of this thesis will be related only to the DG method, we

will consider two different types of mechanical models for describing the damaged materials. In the first one, called "micro-mechanics based damage model" and studied in the first part of the thesis, the micro-cracks are introduced through a damage parameter (crack density parameter) which can increase under the loading wave. The heterogeneity is a material one (the mechanical model looses its isotropy and homogeneity but that the geometric homogeneity is preserved). In the second one, called the "cracked solid" or "cracked material" studied in the second part of this thesis, the micro-cracks, describing the damage of the material, are introduced as a "geometric heterogeneity" in an isotropic and homogeneous elastic solid. This geometric heterogeneity induces a loss of both (global) isotropy and (global) homogeneity of the elastic solid. The lengths (radii) of micro-cracks do not change (no crack growth) under the loading wave, but on the micro-cracks (internal) interface of a unilateral frictional contact is considered. The two models are diametral opposite but they show like a mirror of the physical reality, where both geometric and material heterogeneities are present. At the end of the thesis, in chapter 14, a comparison of these two models illustrates the blast wave.

Finally, we have to mention that all the numerical results presented in this thesis were obtained with "homemade" codes developed in FreeFem++ [59], which is a high level integrated development environment for numerically solving of partial differential equations.

Part I

Damage and wave propagation

CHAPTER 2

INTRODUCTION

Brittle (or quasi-brittle) materials, as ceramics, concretes, rocks, and many others, are more and more used in civil and defense applications as well as in earthquake modeling. The main feature of these materials is a high compressive strength, which increases with the confinement and with the loading rate, in the same time as well as a low tensile strength. Moreover, at high strain rates or sufficiently low temperature even ductile materials exhibit a "brittle" behavior. Modeling damage and failure of brittle materials has become increasingly important in order to appropriately design structures containing brittle materials, to avoid catastrophic failures, or to model the mechanical behavior of fault zones. The effects of damage are particularly important in geo-mechanical models of phenomena that involve high levels of stress such as earthquakes, underground explosions, and meteorite impacts.

Brittle materials contain a large number of defects as micro-voids or micro-cracks, making predictive modeling difficult. A number of models, used in mechanical engineering or in geophysics, are simple empirical models. But there are a lot of micro-mechanics-based models that provide more accurate descriptions of material responses. Some of the latter models are now available in engineering analysis codes. They assume that the macroscopic damage of the material is the result of the response of all the penny-shaped micro-cracks (with different sizes and orientations) to the stress field.

The aim of this part is to analyze the coupled phenomena between the damage evolution and the wave propagation. This coupling is working in both senses: the loading wave, propagating into the material, produces damage and changes the propagation properties of

the material. In this way the mechanical damage processes cannot be separated from the wave propagation process. The micro-crack growth is activated in some privileged directions according to the applied macroscopic loading. That is why we have to use anisotropic models.

We used in the following chapters a discontinuous Galerkin numerical scheme for the numerical integration of the damage model. Why a discontinuous Galerkin approach ? The first reason is related to the damage models. In many damage models the damage evolution laws are written in terms of the stress field, hence the accuracy of computed stress is essential to have a good numerical integration. Between the numerical techniques associated to the elastodynamics equations only finite differences (FD) and discontinuous Galerkin (DG) techniques have the same approximation level for the stress and for the velocities fields. The second reason is related to the fact that damage phenomena are sometimes associated to time and space discontinuities (or instabilities). These difficulties can be successfully be addressed by using high-resolution FD or DG schemes with a suitably defined numerical fluxes and slope limiters. However, in contrast to the FD schemes, DG methods are very well suited to handling complicated geometries.

After a first chapter dedicated to a short overview of the local damage models in brittle materials we give a stability analysis of the constitutive law under a strain driven process. We continue with the presentation of the numerical scheme and we analyze its capacities to approach an exact solution for high and moderate strain rates. The following two chapters will consider the one dimensional and the two dimensional anti-plane wave propagation. Finally we will illustrate the numerical scheme with some numerical results related to blast wave propagation.

CHAPTER 3

SHORT OVERVIEW OF DAMAGE MODELS

The aim of this section is to give a short overview of (anisotropic) damage models. Since this topic was, and still is, a very prolific area of research from different scientific fields (solid mechanics, material science, micro-mechanics, aerospace and civil engineering, solid Earth geophysics, etc) a huge quantity of models was accumulated in the last 50 years. That is why this incomplete overview will focus only on some aspects of brittle materials (local) damage models, related to the next sections.

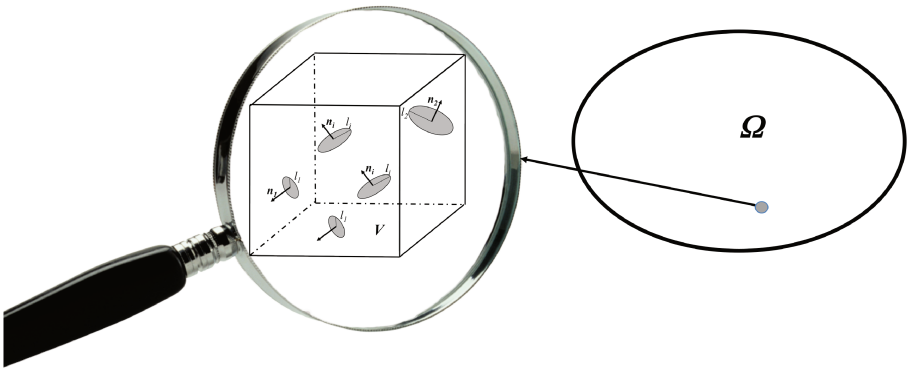

Figure 3.1: Schematic representation of a representative volume V with N types of circular micro-cracks of radius l_i oriented through the normals $\boldsymbol{n}_i$, $i = 1, ...N$.

First let introduce the crack density parameter, which is the main "geometric" parameter used to model damage in brittle materials. Let us suppose that the material contains, in a representative volume V (or in an area A for the two dimensional problems), a population of

N types of circular micro-cracks of radius (half-length in 2D) l_i oriented through the normals vectors $\boldsymbol{n}_i$, $i = 1, ...N$ (see Figure 3.1). The crack density parameter (introduced in [22]) ρ_i is defined as a function of the micro-cracks area (radius or length for circular cracks)

$$\rho_i = \rho(l_i) = \frac{M_i}{V} l_i^3 = \eta_i l_i^3, \quad \text{in } 3D, \qquad \rho_i = \rho(l_i) = \frac{M_i}{A} l_i^2 = \eta_i l_i^2, \quad \text{in } 2D,$$

where M_i is the number of cracks of type i in the volume V (area A) and $\eta_i = M_i/V$ ($\eta_i = M_i/A$) is the flaw density. The crack density parameter is an equivalent (micro-scale) non-dimensional parameter to the micro-crack radius (half-length in 2D) l_i through

$$l_i = l(\rho_i) = (\rho_i/\eta_i)^{1/3}, \quad \text{in } 3D, \qquad l_i = l(\rho_i) = \sqrt{\rho_i/\eta_i}, \quad \text{in } 2D,$$

In the special case $N = 1$ we will distinguish two situations: one family of "parallel cracks" (PC) and "random crack" (RO) orientations.

The principal geometric parameters as the flaw density η, the micro-cracks' radius l and the micro-cracks' orientations $\boldsymbol{n}$ are the micro-mechanics based inputs of the material. These inputs are generally considered as deterministic variables which describe the state of the material. An important step froward was done by Graham-Brady [53] and Huq et al. [65] which proposed a technique for assigning probability distributions to these geometric parameters.

In order to define a damage model we have to state two equations. The first one gives an estimation of effective elastic properties of cracked materials and relates the (macro-scale) stresses $\boldsymbol{\sigma}$ and the (macro-scale) strains $\boldsymbol{\varepsilon}$, trough a linear or non-linear elastic law depending on the (micro-scale) damage variables $\rho_1, ..., \rho_N$. The second one describes the evolution of damage (micro-scale) parameters $\rho_1, ..., \rho_N$ as a function of the (macro-scale) stress $\boldsymbol{\sigma}$ or of the strains $\boldsymbol{\varepsilon}$.

3.1 Effective elasticity of a cracked solid

It is possible to distinguish two classes of micro-mechanical approaches: direct approach and homogenization-based (Eshelby type) approach for heterogeneous materials. The direct approach is generally based on the analysis of displacement discontinuity induced by micro-cracks and on the fracture mechanics for the propagation of cracks.

The direct approach is used in various works on the determination of the effective properties of micro-cracked materials (Nemat-Nasser and Hori [90], Krajcinovic [75], Kachanov [70], Renaud et al. [103]) and in micro-mechanical models (Andrieux et al. [1], Gambarotta and Lagomarsino [52] and Pensé and Kondo [96]). The mathematical formulation of direct micro-mechanical models is relatively simple and does not involve a rigorous upscaling procedure.

We shall also distinguish between the stress-based and strain-based formulations. Stress-based micro-mechanical (anisotropic) damage models take into account (in situ) stresses and pore pressure as key factors for mechanical modeling of damage. They can be written in a general form as

$$\boldsymbol{\varepsilon} = \boldsymbol{\mathcal{A}}(\boldsymbol{\sigma}, \rho_1, ..., \rho_N), \tag{3.1}$$

A typical example, used in this paper (see Gambarotta and Lagomarsino [52] and Kachanov [69] to cite only some), called the "non-interacting cracks method" (NIC) is given in the Appendix. But other direct approaches use the so called "method of effective matrix" (see [69]) to model the crack interactions on a given crack family. Among them we can distinguish the "self-consistent schemes" (SC) developed by Budiansky and O'Connell [22] for random crack orientations, by Hoening [61] for parallel cracks and by Hori and Nemat-Nasser [62] for frictional cracks. The "differential schemes " (see MacLaughlin [86], Hashin [58]), denoted by DS, increase the crack density in small steps and the effective matrix is recalculated at each step. In the appendix we have given the expressions of the Young modulus for one family of micro-cracks (parallel cracks).

We shall suppose in the next following for a given crack density distribution $\rho_1, ..., \rho_N$ the nonlinear elastic constitutive equation (3.1) can be inverted to get the stress as nonlinear function of the strain

$$\boldsymbol{\sigma} = \boldsymbol{\mathcal{E}}(\boldsymbol{\varepsilon}, \rho_1, ..., \rho_N). \tag{3.2}$$

This general expression of the effective elasticity is the starting point of strain-based micro-mechanical anisotropic damage models. This last approach is phenomenological but strongly motivated by the micro-mechanics analysis (see Halm and Dragon [55, 56], Bargellini et al [12, 13]).

The effective properties of cracked materials could also be obtained by following the method based on the Eshelby inhomogeneous inclusion solution (see Eshelby [45, 44], Mura [88]). Using the Eshelby-based homogenization procedure for random heterogeneous materi-

als Deudé et al. [36] and Dormieux et al [38] have built a different approach by considering the cracked material as a matrix-inclusion composite. Ponte-Castaneda and Willis [24] have improved the existing Eshelby-based inclusion models by introducing a new tensor which accounts for the spatial distribution of inclusions. This method was adapted by Zhu et al [131, 130, 132] to get effective properties of cracked materials and to analyze the role of the homogenization scheme (see Appendix chapter 15 for the expressions of the Young and shear moduli for one family of micro-cracks).

3.2 Damage evolution

To complete the damage model let us formulate the evolution of the effective cracked solid (i.e. equations modeling the evolution of each micro-crack type $i = 1, .., .N$ defined by its radius $l = l_i$ and its normal $\boldsymbol{n}_i$). In what follows we restrict ourselves to the cracks whose orientation remains constant (i.e. $\dot{\boldsymbol{n}}_i = 0$). Two types of micro-scale evolutions will be considered: quasi-static and dynamic.

3.2.1 Quasi-static evolution

First, let us first describe the micro-scale quasi-static evolution. For each type of micro-crack we shall consider a negative scalar function $\mathcal{K}^i = \mathcal{K}^i(\rho_i, \boldsymbol{\sigma})$, called "damage criterion function". If $\mathcal{K}^i = \mathcal{K}^i(\rho_i, \boldsymbol{\sigma})$ is negative, the damage (crack density parameter ρ, crack radius/length l) is not growing, but micro-cracks could propagate for $\mathcal{K}^i = 0$. More precisely, the damage evolution law can be expressed through the complementary conditions :

$$\dot{\rho}_i \geq 0, \quad \mathcal{K}^i(\rho_i, \boldsymbol{\sigma}) \leq 0, \quad \mathcal{K}^i(\rho_i, \boldsymbol{\sigma})\dot{\rho}_i = 0, \qquad \text{for all } i = 1, ...N. \tag{3.3}$$

The above nonconservative condition $\dot{\rho}_i \geq 0$, stating the damage irreversibility, can be reformulated for non-smooth (discontinuous) time dependence of the crack radius (length). Indeed, if we assume that the crack density parameter $t \to \rho_i(t)$ is non decreasing then the time derivative $\dot{\rho}_i$ exits in a weak sense (distributions, bounded measures).

It is a difficult task to find a unified criterion for the damage evolution. A first type of damage criterion could be obtained from the microscopic considerations. If we suppose that micro-cracks are not interacting and they have only a self similar growth, we can use the Griffith theory to get a criterion for the micro-crack growth under the macroscopic

stress $\boldsymbol{\sigma}$. One can find in the Appendix chapter 18 the expressions of $\mathcal{K}$ for simple cases in different configurations. These expressions are much more complicated for the growth and interaction of tensile wing cracks nucleated at the tips of a micro-crack. They were obtained by Ashby and Samis [7], Deshpande and Evans [35], Bath et al [20, 21] by incorporating results from many other studies of mode I wing cracks nucleated and driven by mode II sliding (see Kachanov [70], Nemat-Naser and Hori [90], Ashby and Hallam [8], Jeyakumaran and Rudnicki [66] and others). Paliwal and Ramesh [95] and Hu et al. [63] have a different approach for tensile wing cracks by using the superposition principle to compute $\mathcal{K}(\rho, \boldsymbol{\sigma})$(for details see Chapter 18 of the Appendix).

The second type of damage criterion is obtained by integrating the results obtained in micro-mechanical analysis into the thermodynamic framework, classically used for the macroscopic formulation (see for instance Zhu et al [131, 130, 132]). To do this one can introduce the elastic potential $W(\boldsymbol{\varepsilon}, \rho_1, ..., \rho_N)$ and its conjugate $W^*(\boldsymbol{\sigma}, \rho_1, ..., \rho_N)$ such that (3.1) and (3.2) can be written as

$$\boldsymbol{\varepsilon} = \frac{\partial W^*}{\partial \boldsymbol{\sigma}}(\boldsymbol{\sigma}, \rho_1, ..., \rho_N), \qquad \boldsymbol{\sigma} = \frac{\partial W}{\partial \boldsymbol{\varepsilon}}(\boldsymbol{\varepsilon}, \rho_1, ..., \rho_N).$$

Using thermodynamic force $\mathcal{F}_i$ associated to the family i, defined as $\mathcal{F}_i = \dfrac{\partial W^*}{\partial \rho_i}$ (or $\mathcal{F}_i = \dfrac{\partial W}{\partial \rho_i}$), the damage criterion is introduced as $\mathcal{K}^i(\rho_i, \boldsymbol{\sigma}) = \mathcal{F}_i(\rho_i, \boldsymbol{\sigma}) - \mathcal{R}_i(\rho_i)$, where $\mathcal{R}_i$ represents the "material resistance" to the micro-cracks family i growth of micro-cracks belonging to family i (damage evolution).

3.2.2 Dynamic evolution

For very high deformation rates, the above rate independent constitutive law for damage evolution has to be reconsidered by using a model able to describe the dynamics of micro-cracks propagation. The general equation for dynamic damage could be written as follows

$$\dot{\rho}_i = \mathcal{L}^i(\rho_i, \boldsymbol{\sigma}). \tag{3.4}$$

Particular expressions of $\mathcal{L}^i$ can be obtained from the quasi-static damage criterion function $\mathcal{K}^i$. Indeed, the micro-crack propagation criterion is commonly given through a "dynamic stress intensity factor" K_d^i instead of the "static stress intensity factor" K^i (see

[50, 49, 32])). Since the first one is obtained from the second one, the expression of the damage rate $\mathcal{L}$ yields (see for instance Paliwal and Ramesh [95], Hu et al. [63] and the Appendix chapter 18 for details).

To ensure the compatibility between quasi-static and dynamic damage evolution criteria (i.e. $\mathcal{L}(\rho, \boldsymbol{\sigma}) = 0$ for $\mathcal{K}(\rho, \boldsymbol{\sigma}) \leq 0$) one can suppose that there exists an increasing positive non-dimensional function $\varphi_i : [0, 1] \to R_+$ with $\varphi_i(0) = 0$ which gives the crack growth rate $\dot{l}_i$:

$$\frac{d}{dt} l(\rho_i) = c_m \varphi_i([\frac{\mathcal{K}^i(\rho_i, \boldsymbol{\sigma})}{\alpha + \mathcal{K}^i(\rho_i, \boldsymbol{\sigma})}]_+), \quad \text{for all } i = 1, ...N, \tag{3.5}$$

where $[x]_+ = (x + |x|)/2$ is the positive value function, c_m is associated to the "micro-scale" crack growth velocity and $\alpha > 0$ is a non-dimensional constant. We remark that using this expression of the micro-crack propagation speed we get the rate of the crack density parameter, given by

$$\dot{\rho}_i = \mathcal{L}^i(\rho_i, \boldsymbol{\sigma}) = \frac{c_m}{l'(\rho_i)} \varphi_i([\frac{\mathcal{K}^i(\rho_i, \boldsymbol{\sigma})}{\alpha + \mathcal{K}^i(\rho_i, \boldsymbol{\sigma})}]_+), \quad \text{for all } i = 1, ...N. \tag{3.6}$$

But the compatibility between quasi-static and dynamic damage evolution criteria can be obtained asymptotically by using a power law (see for instance Deshpande and Evans [35] and the Appendix chapter 16 for details).

Another type of dynamic approach of the damage evolution makes use of the probabilistic approach to derive the evolution law of the damage variables on a continuum level. The Denoual-Forquin-Hild model (Denoual and Hild [33], Forquin and Hild [48]) is based on the description of micro-mechanisms activated during the dynamic fragmentation process. It depicts the random distribution of defects in the microstructure, the onset, the propagation of unstable cracks and the obscuration of critical defects in the vicinity of cracks. Zinszner et al. [133] and Erzar and Forquin [43] use the method provided in Denoual and Hild [34] (see also Hild et al. [60])to derive a random critical stress.

3.3 Quasi-static versus dynamic

Let us discuss now the choice of dynamic vs. the quasi-static damage evolution laws. For that let us consider a strain driven problem with a given rate of deformation $\dot{\epsilon}_c$ and a final

characteristic strain ϵ_f. The loading characteristic time is $T^{load} = \frac{\epsilon_f}{\dot{\epsilon}_c}$ while, as it follows from (3.5), the micro-scale characteristic time is $T^{micro} = \frac{L^{micro}}{c_m}$, where L^{micro} is the micro-scale length scale (characteristic radius of a micro-crack). It is clear now that if $T^{load} >> T^{micro}$ then the quasi-static model has to be used. In contrast, for very high rate of deformations $\dot{\epsilon}_c$, the loading characteristic time could be of order of the micro-scale characteristic time ($T^{load} \approx T^{micro}$) and we have to use the dynamic model of damage. In this case, the dynamics of micro-cracks growth play an important role in the macro-scale deformation.

Let us notice that micro-scale quasi-static regime can be present even for a macro-scale dynamic process. Indeed, having in mind that the macro-scale process is dynamic if $T^{load} \approx T^{macro} = \frac{L^{macro}}{c_P}$ (c_P is the P-wave speed and L^{macro} is the macro-scale characteristic length) and the fact that c_m is of order of c_P we deduce that $T^{load} >> T^{micro}$ is compatible with $L^{macro} >> L^{micro}$.

CHAPTER 4

DAMAGE MATERIAL STABILITY

4.1 Introduction

One challenging phenomenon in brittle materials is related to the instabilities associated to the material softening, which occurs due to accumulation of damage. Since damage models are describing micro-cracks growth, which is generally an unstable phenomenon, it is natural to expect some loss of stability on the associated micro-mechanics based models. If the model accurately captures the material behavior, then this can be due to the unstable nature of the brittle material itself. If the model does not take strain-rate or spatially nonlocal effects into account this material instability can cause to the associated initial and boundary value problem to be unstable or ill-posed. This often leads to lack of convergence upon mesh refinement in numerical solutions.

The aim of this section is to analyze the stability of the damage constitutive law under a strain driven process. To do that we restrict ourselves to the stability of the equilibrium configurations but we consider a rather general approach of damage. Further we will investigate the case of one family of micro-cracks for NIC effective elasticity associated to a self-similar growth of micro-cracks under a stress far field.

In both cases (quasi-static and dynamic) we say that $\boldsymbol{\varepsilon}^0, \boldsymbol{\sigma}^0, \rho_1^0, .., \rho_N^0$ is an equilibrium configuration if

$$\boldsymbol{\varepsilon}^0 = \boldsymbol{\mathcal{A}}(\boldsymbol{\sigma}^0, \rho_1^0, ..., \rho_N^0), \quad \text{and} \quad \mathcal{K}^i(\rho_i^0, \boldsymbol{\sigma}^0) \leq 0, \quad \text{for all } i = 1, ...N. \tag{4.1}$$

4.2 Quasi-static stability analysis

Let us define here what we mean by a stable equilibrium configuration in a quasi-static strain-driven process. Since the problem is non-smooth we have to use a more elementary definition. We say that an equilibrium $\boldsymbol{\varepsilon}^0, \boldsymbol{\sigma}^0, \rho_1^0, .., \rho_N^0$ is *stable* if for all neighborhood V of $(\boldsymbol{\sigma}^0, \rho_1^0, .., \rho_N^0)$ there exists a neighborhood W of $\boldsymbol{\varepsilon}^0$ such that for all continuous strain-path $t \to \boldsymbol{\varepsilon}(t)$ in W, with $\boldsymbol{\varepsilon}(0) = \boldsymbol{\varepsilon}^0$, there exists a continuous material response in V, i.e. there exists a continuous time evolution $t \to (\boldsymbol{\sigma}(t), \rho_1(t), .., \rho_N(t)) \in V$, with $\boldsymbol{\sigma}(0) = \boldsymbol{\sigma}^0, \rho_1(0) = \rho_1^0, .., \rho_N(0) = \rho_N^0$, satisfying (3.1) and

$$\dot{\rho}_i(t) \geq 0, \quad \mathcal{K}^i(\rho_i(t), \boldsymbol{\sigma}(t)) \leq 0, \quad \mathcal{K}^i(\rho_i(t), \boldsymbol{\sigma}(t))\dot{\rho}_i(t) = 0, \tag{4.2}$$

for all $i = 1, .., N$. We say that a strain-driven quasi-static process is stable if $\boldsymbol{\varepsilon}(t), \boldsymbol{\sigma}(t), \rho_1(t), .., \rho_N(t)$ is a stable equilibrium at each time t.

Let us give some physical interpretation of the above "abstract" definition. For that we have plotted in Figure 4.1 a schematic representation of a quasi-static damage process in the space of stress $\boldsymbol{\sigma}$, strain $\boldsymbol{\varepsilon}$ and crack density parameter ρ. The damage evolution curve ($\dot{\rho} > 0$) is the intersection of the effective elastic surface $\boldsymbol{\varepsilon} - \boldsymbol{\mathcal{A}}(\boldsymbol{\sigma}, \rho) = 0$ with the damage surface $\mathcal{K}(\rho, \boldsymbol{\sigma}) = 0$. We can see on this curve two examples of stable and unstable material equilibrium configurations. The evolution of point S can be done either on damage evolution curve corresponding to an increasing damage ($\dot{\rho} > 0$) and an increasing strain or on the unloading curve corresponding to a constant damage ($\dot{\rho} = 0$) and a decreasing strain. On the contrary, the evolution of point U is much more complicated. For decreasing strain we have to choose between the damage evolution curve corresponding to an increasing damage ($\dot{\rho} > 0$) and the unloading curve corresponding to a constant damage ($\dot{\rho} = 0$). But, for increasing strain there exists no continuous path obeying the irreversible damage assumption ($\dot{\rho} \geq 0$). We conclude that S is a stable configuration and U is an unstable one.

From the above example we deduce that for a given continuous strain history $t \to \boldsymbol{\varepsilon}(t)$ we could have several solutions (material responses) of the quasi-static problem and in some cases there exists no continuous material response. However, since the quasi-static problem (3.1),(4.2) is ill-posed, a criterion to select the most appropriate solution with a physical interpretation is needed. Whatever the selection rule, shocks (time discontinuities) will occur. A possible choice for this criterion is the so-called *perfect delay convention*: the

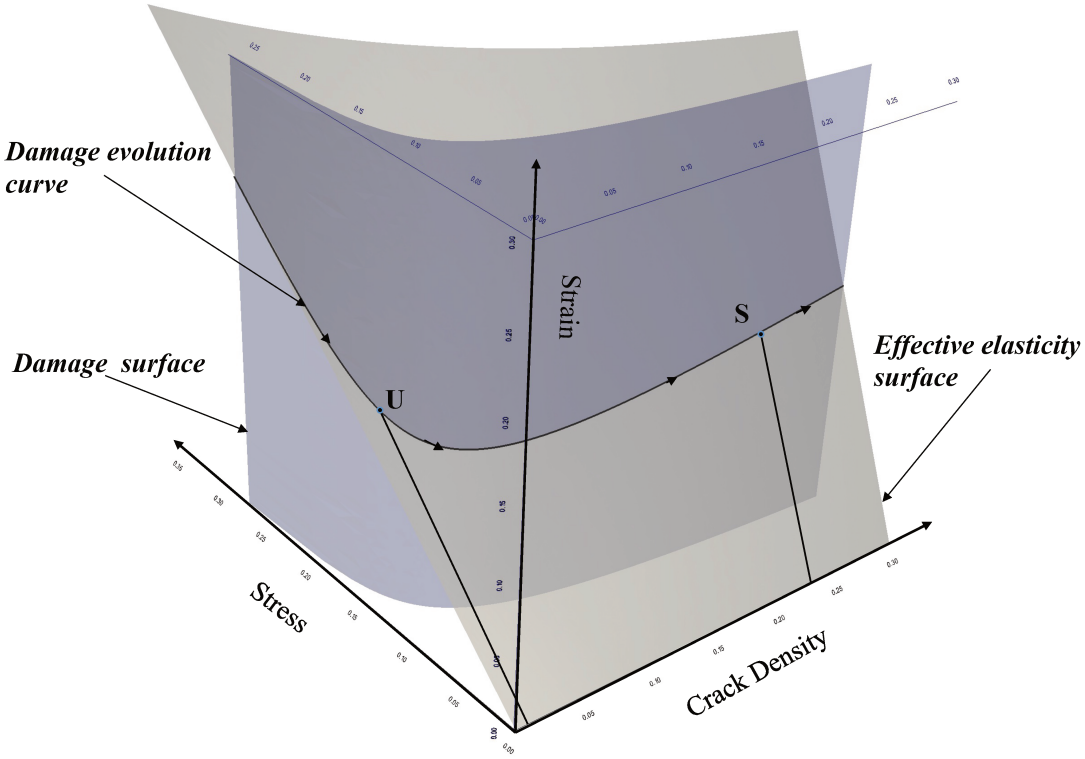

Figure 4.1: Schematic representation of a quasi-static damage process in the space of stress $\boldsymbol{\sigma}$, strain $\boldsymbol{\varepsilon}$ and crack density parameter ρ.

system only jumps when it has no other choice. That is, the quasi-static equilibrium chosen by the perfect delay convention is always stable. In this way different paths of solutions are obtained in loading and unloading processes and hysteresis phenomena could occur (see next chapter). The perfect delay convention is not always related to a simple energy criterion. It comes from catastrophe theory (see for instance [101]), and it is implicitly present in the analysis of many physical problems. It is used in the study of static or quasi-static problems and could be justified by a dynamic stability analysis (see the end of the next section).

To characterize the stability of an equilibrium configuration $\boldsymbol{\varepsilon}^0, \boldsymbol{\sigma}^0, \rho_1^0, .., \rho_N^0$ let us suppose that M micro-cracks of the N ($M \leq N$) family are "active" (could have quasi-static growth

$\dot\rho > 0$) while the other ones are not ($\dot\rho = 0$), i.e.

$$\begin{cases} \mathcal{K}^i(\rho_i^0, \boldsymbol{\sigma}^0) &= 0, \quad \text{for all } i = 1, .., M, \\ \mathcal{K}^i(\rho_i^0, \boldsymbol{\sigma}^0) &< 0, \quad \text{for all } i = M+1, .., N, \end{cases} \tag{4.3}$$

and $\mathcal{K}^i$ and $\boldsymbol{\mathcal{E}}$ are differentiable at $\boldsymbol{\sigma}^0, \rho_1^0, .., \rho_M^0$.

Let us suppose that $\boldsymbol{\varepsilon}^0, \boldsymbol{\sigma}^0, \rho_1^0, .., \rho_N^0$ is stable, hence for any given smooth strain history $t \to \boldsymbol{\varepsilon}(t)$, with $\boldsymbol{\varepsilon}(0) = \boldsymbol{\varepsilon}^0$ there exists a smooth material response $t \to \boldsymbol{\sigma}(t), \rho_1(t), .., \rho_N(t)$ with $\boldsymbol{\sigma}(0) = \boldsymbol{\sigma}^0, \rho_1(0) = \rho_1^0, .., \rho_N(0) = \rho_N^0$. From (4.3) we have $\dot\rho_i(0) = 0$ for all $i = M+1, .., N$ and since $\mathcal{K}^i(\rho_i(t), \boldsymbol{\sigma}(t)) \le 0$ we get $\dfrac{d}{dt}\mathcal{K}^i(\rho_i(t), \boldsymbol{\sigma}(t)) \le 0$ for all $i = 1, .., M$. From this last inequality we deduce

$$\frac{\partial \mathcal{K}^i}{\partial \rho}\dot\rho_i + \sum_{j=1}^{M} \frac{\partial \mathcal{K}^i}{\partial \boldsymbol{\sigma}} : \frac{\partial \boldsymbol{\mathcal{E}}}{\partial \rho_j}\dot\rho_j \le -\frac{\partial \mathcal{K}^i}{\partial \boldsymbol{\sigma}} : \frac{\partial \boldsymbol{\mathcal{E}}}{\partial \boldsymbol{\varepsilon}} : \dot{\boldsymbol{\varepsilon}}, \quad \text{for all } i = 1, .., M. \tag{4.4}$$

Since the strain rate history $\dot{\boldsymbol{\varepsilon}}$ is arbitrary, we deduce that the last inequality must have a solution $(\dot\rho_1, .., \dot\rho_M) \in \mathbb{R}_+^M$ for all negative righthand side. If we denote by $\boldsymbol{\mathcal{I}}$ the *quasi-static tangent matrix*

$$\mathcal{I}_{ij}^0 = \frac{\partial \mathcal{K}^i}{\partial \rho}(\rho_i^0, \boldsymbol{\sigma}^0)\delta_{ij} + \frac{\partial \mathcal{K}^i}{\partial \boldsymbol{\sigma}}(\rho_i^0, \boldsymbol{\sigma}^0) : \frac{\partial \boldsymbol{\mathcal{E}}}{\partial \rho_j}(\boldsymbol{\varepsilon}^0, \rho_1^0, ..., \rho_N^0), \tag{4.5}$$

then we see that the lefthand side is now $\mathcal{I}^0(\dot\rho_1, .., \dot\rho_M)^T$ and if stability occurs then the image of the cone $\mathbb{R}_+^M$ through the matrix $\boldsymbol{\mathcal{I}}^0$ contains the cone $\mathbb{R}_-^M$, i.e. $\mathbb{R}_-^M \subset \boldsymbol{\mathcal{I}}^0(\mathbb{R}_+^M)$. But since $\boldsymbol{\mathcal{I}}(\mathbb{R}^M)$ is a space of dimension $M - k$, where k is the dimension of the kernel of $\boldsymbol{\mathcal{I}}^0$, from this last inclusion we deduce that $\boldsymbol{\mathcal{I}}^0$ must be invertible (i.e. $k = 0$) and we should have

$$\boldsymbol{\mathcal{I}}^0(\mathbb{R}_+^M) = \mathbb{R}_-^M, \tag{4.6}$$

which is a *necessary stability condition*.

Let remark that the above equality is also a *sufficient stability condition*. Indeed, for the following nonlinear system of equations

$$\mathcal{F}_i(\rho_1, ..., \rho_M, \boldsymbol{\varepsilon}) = \mathcal{K}^i(\rho_i, \boldsymbol{\mathcal{E}}(\boldsymbol{\varepsilon}, \rho_1, ..., \rho_N)) = 0, \quad \text{for all } i = 1, .., M, \tag{4.7}$$

the tangent matrix is also $\mathcal{I}_{ij}^0 = \frac{\partial \mathcal{F}_i}{\partial \rho_j}(\boldsymbol{\varepsilon}^0, \rho_1^0, ..., \rho_M^0)$ and from the implicit function theorem and (4.6) we get that (4.7) has locally a smooth nondecreasing solution $t \to (\rho_1(t), .., \rho_M(t))$

for all strain process in the neighborhood of $\boldsymbol{\varepsilon}^0$.

For weak inter-families interactions, i.e. for

$$\frac{\partial \mathcal{K}^i}{\partial \boldsymbol{\sigma}}(\rho_i^0, \boldsymbol{\sigma}^0) : \frac{\partial \boldsymbol{\mathcal{E}}}{\partial \rho_j}(\boldsymbol{\varepsilon}^0, \rho_1^0, ..., \rho_N^0) \cong 0, \quad \text{for all } i \neq j,\ i,j = 1,..,M,, \tag{4.8}$$

or for a single active family of micro-cracks ($M = 1$) the stability condition (4.6) has a much simpler formulation: $\boldsymbol{\mathcal{I}}^0$ has negative elements on the diagonal, i.e

$$\frac{\partial \mathcal{K}^i}{\partial \rho}(\rho_i^0, \boldsymbol{\sigma}^0) + \frac{\partial \mathcal{K}^i}{\partial \boldsymbol{\sigma}}(\rho_i^0, \boldsymbol{\sigma}^0) : \frac{\partial \boldsymbol{\mathcal{E}}}{\partial \rho_i}(\boldsymbol{\varepsilon}^0, \rho_1^0, ..., \rho_N^0) < 0, \quad \text{for all } i = 1,..,M. \tag{4.9}$$

4.3 Dynamic stability analysis

Let us remark first that a strain-driven process can be described only by a micro-scale time evolution. Indeed, for a given strain history $t \to \boldsymbol{\varepsilon}(t)$,with $\boldsymbol{\varepsilon}(0) = \boldsymbol{\varepsilon}_0$, we get from (3.4) and (3.2) that $t \to \rho_i(t),\ i = 1,..,N$ is the solution of the following nonlinear system of N differential equations

$$\frac{d}{dt}\rho_i(t) = \mathcal{L}^i(\rho_i, \mathcal{E}(\boldsymbol{\varepsilon}(t), \rho_1(t), .., \rho_N(t))), \quad \text{for all } i = 1,..,N. \tag{4.10}$$

with the initial condition $\rho_1(0) = \rho_1^0, .., \rho_N(0) = \rho_N^0$.

We say that an equilibrium configuration $\boldsymbol{\varepsilon}^0, \boldsymbol{\sigma}^0, \rho_1^0, .., \rho_N^0$ is *dynamically stable* if there exists a neighborhood W of $\boldsymbol{\varepsilon}^0$ such that for all continuous strain-path $t \to \boldsymbol{\varepsilon}(t)$ in W the solution $t \to (\rho_1(t), .., \rho_N(t))$ of the micro-scale differential system (5.1) is stable in the sense of Lyapunov.

To characterize the dynamic stability of an equilibrium configuration $\boldsymbol{\varepsilon}^0, \boldsymbol{\sigma}^0$, $\rho_1^0, .., \rho_N^0$ let us suppose that M micro-cracks families out of N ($M \leq N$) are active while the other ones are not (i.e. (4.3) holds) and $\mathcal{L}^i$ and $\boldsymbol{\mathcal{E}}$ are differentiable at $\boldsymbol{\sigma}^0, \rho_1^0, .., \rho_M^0$. For the linear stability analysis we have to compute the *dynamic tangent matrix* $\boldsymbol{\mathcal{T}}^0 = (\mathcal{T}_{ij}^0)$,

$$\mathcal{T}_{ij}^0 = \frac{\partial \dot{\rho}^i}{\partial \rho_j} = \frac{\partial \mathcal{L}^i}{\partial \rho}(\rho_i^0, \boldsymbol{\sigma}^0)\delta_j^i + \frac{\partial \mathcal{L}^i}{\partial \boldsymbol{\sigma}}(\rho_i^0, \boldsymbol{\sigma}^0) : \frac{\partial \boldsymbol{\mathcal{E}}}{\partial \rho_j}, \quad \text{for all } i,j = 1,..,M.$$

We can formulate now the following linear stability criterion: the equilibrium configuration

$\boldsymbol{\varepsilon}^0, \boldsymbol{\sigma}^0, \rho_1^0, .., \rho_N^0$ is *linearly dynamically stable* if

$$\boldsymbol{\mathcal{T}}^0 \qquad \textit{has all its eigenvalues with a negative real part.} \tag{4.11}$$

To relate quasi-static and dynamic stability analyses, we shall suppose that the dynamic rate of damage $\mathcal{L}^i$ is constructed from the quasi-static criterion $\mathcal{K}^i$ through the equation (3.6). Denote by $\boldsymbol{\mathcal{D}} = (\mathcal{D}_{ij})$ the diagonal matrix $\mathcal{D}_{ij}^0 = \dfrac{c_m}{l'(\rho_i^0)}\varphi_i'(0)\delta_{ij}$ and using (3.6) we obtain the following relation between the dynamic and quasi-static tangent matrices

$$\boldsymbol{\mathcal{T}}^0 = \boldsymbol{\mathcal{D}}^0\boldsymbol{\mathcal{I}}^0, \qquad \mathcal{T}_{ij}^0 = \frac{c_m}{l'(\rho_i^0)}\varphi_i'(0)\mathcal{I}_{ij}^0.$$

Having in mind the above connection between the tangent and interaction matrices one can notice that, generally, the dynamic and quasi-static criteria do not coincide. However, for weak inter-families interactions assumption (5.3) or for a single active family of micro-cracks ($M = 1$), the dynamic linear stability criterion (4.11) is exactly the quasi-static stability criterion (4.9).

4.4 One family of micro-cracks

We would like to illustrate here the above stability analysis. For that we have chosen a very simple one-dimensional problem with only one family of micro-cracks ($N = 1$) of radius (half length) $l = l(\rho)$ and normal vector $\boldsymbol{n} = (1, 0, 0)$. We shall denote by $\tau \geq 0$ the (generic) stress and by $\gamma \geq 0$ the (generic) strain (see table 4.1 for different configurations).

For the effective elasticity law we have chosen the "non-interacting cracks method" (NIC) (see for instance Gambarotta and Lagomarsino [52] and Kachanov [69]) but other laws could be considered. The strain-stress equation (17.1) can be written as

$$\gamma = \mathcal{A}(\tau, l) = A_0\tau + C\rho(l)[\tau - f]_+,$$

where $f \geq 0$ is the friction force and A_0, C are compliance coefficients (see table 4.1) and η is the flaw density.

For the damage evolution law we have chosen the criterion associated to the micro-cracks self similar growth under a far field stress (4.2) when the stress intensity factor K has simple

	Mode I, 3-D	I, 2-D	II, 2-D	III, 2-D
τ	σ_{xx}	σ_{xx}	σ_{xy}	σ_{xz}
γ	$\epsilon_{xx} + \dfrac{\nu_0}{1-\nu_0}(\epsilon_{yy} + \epsilon_{zz})$	$\epsilon_{xx} + \nu_0' \epsilon_{yy}$	ϵ_{xy}	ϵ_{xz}
A_0	$\dfrac{(1+\nu_0)(1-2\nu_0)}{E_0(1-\nu_0)}$	$\dfrac{1-(\nu_0')^2}{E_0'}$	$\dfrac{1+\nu_0'}{E_0'}$	$\dfrac{1+\nu_0}{E_0}$
C	$\dfrac{16(1-\nu_0^2)}{3E_0}$	$\dfrac{2\pi}{E_0'}$	$\dfrac{\pi}{E_0'}$	$\dfrac{2\pi(1+\nu_0)}{E_0}$
f	0	0	$\mu[-\sigma_{xx}]_+$	$\mu[-\sigma_{xx}]_+$
a	$\dfrac{\sqrt{2}}{\pi}$	$\sqrt{\pi}$	$\sqrt{\pi}$	$\sqrt{\pi}$

Table 4.1: Single micro-crack family: the expressions of the generic stress τ, strain γ, compliance coefficients A_0, C, the friction force f and the non-dimensional constant a in different configurations.

expression

$$\mathcal{K}(l,\tau) = \frac{K(l,\tau)}{K_c} - 1, \qquad K(l,\tau) = a\sqrt{l}[\tau - f]_+ \tag{4.12}$$

with a different non-dimensional number for each configuration (see table 4.1).

4.4.1 Quasistatic evolution

The quasi-static strain-driven problem (3.1),(3.3) can be written as : for a given strain loading $t \to \gamma(t)$ find the stress $t \to \tau(t)$ and the micro-cracks length $t \to l(t)$ solution of

$$\begin{cases} \gamma = A_0\tau + C\rho(l)[\tau - f]_+, \quad \dot{l} \geq 0, \\ a\sqrt{l}[\tau - f]_+ \leq K_c, \qquad \dot{l}\left(a\sqrt{l}[\tau - f]_+ - K_c\right) = 0, \end{cases}$$

with the initial condition $l(0) = l^0$.

To see what equations correspond to a damage increase (i.e. $\dot{l} > 0$) we have to have $\tau > f$ and the following system of algebraic equations for the unknowns l and τ

$$A_0\tau + C\rho(l)(\tau - f) = \gamma, \quad a\sqrt{l}(\tau - f) = K_c. \tag{4.13}$$

	Mode I, 3-D	I, 2-D	II, 2-D	III, 2-D
ρ^c	$\frac{3(1-2\nu_0)}{80(1-\nu_0)^2}$	$\frac{1-(\nu_0')^2}{6\pi}$	$\frac{1+\nu_0'}{3\pi}$	$\frac{1}{6\pi}$

Table 4.2: Single micro-crack family: the expressions of the critical crack density parameter ρ^c in different configurations.

One can rewrite the above equation for the length l as follows:

$$\gamma = L^{eq}(l) = A_0 f + \frac{K_c}{a\sqrt{l}}(A_0 + C\rho(l)), \tag{4.14}$$

or equivalently for the stress τ

$$\gamma = \Sigma^{eq}(\tau) = A_0\tau + C\rho(\frac{K_c^2}{a^2(\tau - f)^2}), \tag{4.15}$$

where $\gamma = L^d(l)$ and $\gamma = \Sigma^d(\tau)$ equilibrium curves. A simple analysis of these equilibrium curves could explain the mechanical behavior during a loading (or unloading) process. For that let us compute

$$\frac{dL^{eq}}{dl} = \frac{K^c}{2al\sqrt{l}}(A_0 + C\rho(l) - 2Cl\rho'(l))$$

and let us notice that there exists a *critical micro-crack radius (half length)* l^c which discriminates the monotonicity of function L^{eq}. Indeed if l_c is the solution of the equation $2lC\rho'(l) = A_0 + C\rho(l)$ then L^d is decreasing for $l < l^c$ and increasing for $l > l^c$. This critical value can be easily computed to find the critical damage parameter ρ^c

$$\rho^c = \frac{A_0}{3C} \quad \text{in 2-D}, \qquad \rho^c = \frac{A_0}{5C} \quad \text{in 3-D}, , \tag{4.16}$$

which is given in Table 4.2 in various configurations. One can also get the critical crack-length l^c, the critical stress τ^c and the critical strain γ^c:

$$l^c = l(\rho_c), \quad \tau^c = f + \frac{K_c}{a\sqrt{l^c}}, \quad \gamma^c = A_0\tau_c + C\rho_c\frac{K_c}{a\sqrt{l^c}}. \tag{4.17}$$

In figure 4.2 we have represented the equilibrium curves $\gamma = L^{eq}(l)$ (left) and $\gamma = \Sigma^{eq}(\tau)$ (right). It corresponds to mode III for ceramics ($\nu_0 = 0.24, E_0 = 300$ GPa, $K^c_{III} = 2.7$ MPa$\sqrt{\text{m}}, \eta = 10^6/(2\pi)\text{m}^{-2}$) but it can be considered as a generic representation for all the

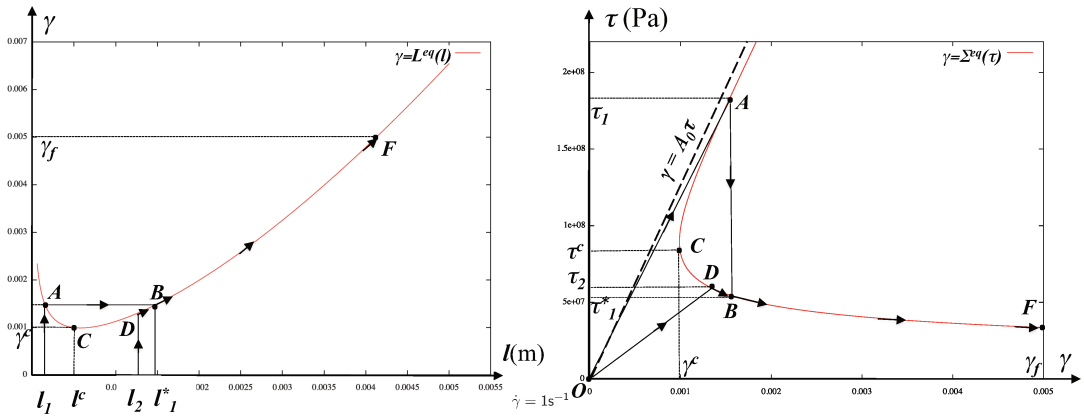

Figure 4.2: The equilibrium curves: $\gamma = L^{eq}(l)$ (left) and $\gamma = \Sigma^{eq}(\tau)$ (right) in red. The evolution of the path micro-crack length-strain ($t \to (l(t); \gamma(t))$ on the left) and of the path strain-stress ($t \to (\gamma(t); \tau(t))$ on the right) for two scenarios corresponding to different initial damage (micro-crack length) $l_0 = l_1 < l^c$ and $l_0 = l_2 \geq l^c$ during a quasi-static strain driven process.

other cases. As it follows from the graphic representation of the functions $l \to L^{eq}(l)$ and $\tau \to \Sigma^{eq}(\tau)$ (see figure 4.2) for $\gamma < \gamma^c$ there are no solution of (4.14) (or (4.15)). That means that damage cannot increase if the strain is less than γ^c, the critical level of strain, for any level of damage (micro-crack length l). For $\gamma = \gamma^c$ we deal with a single solution $l = l^c$ and $\tau = \tau^c$, while for $\gamma > \gamma^c$ there are always two distinct solutions $l < l^c < l^*$ and $\tau < \tau^c < \tau^*$.

Let us check now the stability criterion (4.9). Using the above formulae we have

$$\frac{\partial K}{\partial l} + \frac{\partial K}{\partial \tau}\frac{\partial \mathcal{E}}{\partial l} = \frac{(\tau - f)a}{2\sqrt{l}}\left(1 - \frac{2l\rho'(l)C}{A_0 + C\rho(l)}\right)$$

which means that the stability criterion (4.9) is satisfied only for $l > l^c$. The decreasing part ($l < l^c$) of the curve $\gamma = L^d(l)$ corresponds to unstable equilibria while the increasing part deals with stable equilibria.

Let us analyze here two scenarios for two different initial micro-crack lengths l_0 (initial damage) in a loading strain driven process ($\dot{\gamma} > 0$). For simplicity we suppose that there is no friction ($f = 0$). The process starts at $\gamma = 0$ (point O on Figure 4.2 right) to reach a final level of strain $\gamma = \gamma_f$ higher that the critical strain ($\gamma_f > \gamma_c$). The first scenario deals with a small initial damage corresponding to $l_0 = l_1 < l^c$. We remark that for a first period of time

(OA on Figure 4.2 right) the micro-cracks do not grow ($\dot{l} = 0$) and the strain-stress path is linear. Then the stress reaches the activation level τ_1 (A on Figure 4.2), corresponding to the intersection between the linear strain-stress path and the equilibrium curve $\gamma = \Sigma^{eq}(\tau)$. Following the stability criterion (4.9) this equilibrium position ($l = l_1, \tau = \tau_1$) is not stable and accordingly to the *perfect delay convention*, the material response has to reach the stable equilibrium position $\tau = \tau_1^*, l = l_1^*$ (B on Figure 4.2). That means that we deal with a jump (time discontinuity) of the stress and damage fields. As we shall see in the next subsection this time discontinuity for the stress and damage fields at the quasi-static time-scale is a (dynamic) unstable growth at the dynamic time-scale. After this time discontinuity, the stress and the damage have a smooth evolution on the curve $\gamma = \Sigma^d(\tau)$ to reach the final strain (F on Figure 4.2). The second scenario starts with $l_0 = l_2 \geq l^c$. As before there is a first period of time (OD on Figure 4.2 right) during which the micro-cracks do not grow ($\dot{l} = 0$) and the strain-stress path is linear. When the stress reaches the activation level τ_2 (D on Figure 4.2), the micro-cracks start growing smoothly following the curve $\gamma = L^d(l)$ to reach the final strain (the path DF on Figure 4.2).

4.4.2 Dynamic evolution

The dynamic strain-driven problem (3.1),(3.5) can be written as: for a given strain loading $t \to \gamma(t)$ find the stress $t \to \tau(t)$ and the micro-cracks length $t \to l(t)$ solution of

$$\begin{cases} \dot{l}(t) = c_m \varphi\Big(\Big[\dfrac{a\sqrt{l}[\mathcal{E}(\gamma(t), l(t)) - f]_+ - K_c}{(\alpha - 1)K_c + a\sqrt{l}[\mathcal{E}(\gamma(t), l(t)) - f]_+} \Big]_+ \Big), \\ \tau(t) = \mathcal{E}(\gamma(t), l(t)) \end{cases} \tag{4.18}$$

with the initial condition $l(0) = l^0$.

Since we deal with a single family of micro-cracks the dynamic stability criterion reduces to the quasi-static stability criterion (4.9) (see the remark at end of section 4) which is satisfied only for $l > l^c$. The decreasing part ($l < l^c$) of the curve $\gamma = L^d(l)$ corresponds to a dynamically unstable equilibrium while on the increasing part deals with a dynamic stable equilibrium.

Let us analyze here the two scenarios, considered above in the quasi-static case, for the dynamic problem (4.18). As before the computations have been done for mode III anti-plane cracks ($\alpha = 1, c_m = c_S$ and $\varphi(x) = x$) but the results could be considered as generic

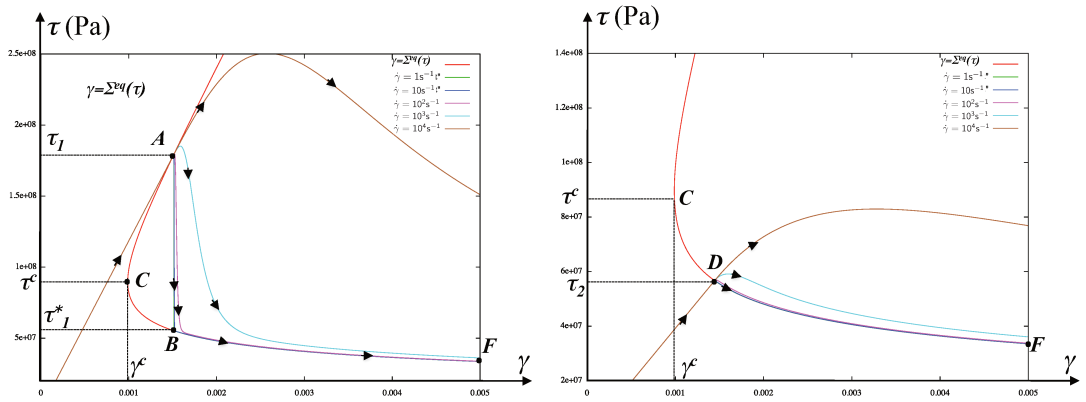

Figure 4.3: The evolution of the strain-stress path $t \to (\gamma(t); \tau(t))$ for different strain rates: $\dot{\gamma} = 1, 10, 10^2, 10^3, 10^4 \text{s}^{-1}$ during a dynamic strain driven process and the equilibrium curve $\gamma = \Sigma^{eq}(\tau)$ (in red). Left: the first scenario for initial damage (micro-crack length) $l_0 = l_1 < l^c$. Right: second scenario for initial damage (micro-crack length) $l_0 = l_2 \geq l^c$.

for all other cases. We have computed numerically the dynamic solution for two different initial micro-crack lengths l_0 (initial damage) in a loading strain-driven process $\gamma(t) = t\dot{\gamma}$ for five values of the strain rate $\dot{\gamma} = 1, 10, 10^2, 10^3, 10^4 \text{s}^{-1}$ and we have plotted the strain-stress paths in Figure 4.3. In the first scenario we have chosen $l_0 = l_1 = 0.25l^c < l^c$. For a first period of time, corresponding to AO in Figure 4.3 (left), the micro-cracks are inactive ($\dot{l} = 0$) and the strain-stress path is linear and rate-independent. Then we reach the equilibrium configuration $l = l_1, \tau = \tau_1$, corresponding to point A on the curve $\gamma = \Sigma^{eq}(\tau)$, which is an unstable position. For high rates of deformations $\dot{\gamma} = 10^3, 10^4 \text{s}^{-1}$ the strain-stress paths is very different from the quasi-static paths but for moderate rate of deformations $\dot{\gamma} = 1, 10, 10^2 \text{s}^{-1}$ the strain-stress curves are almost rate independent and coincide with the quasi-static one. This is due to the fact that micro-scale time-scale is very small (of order of l^c/c_S) and we need a very high strain rate to compensate a rapid material weakening. Notice that the perfect delay convention, which let us to choose a solution in the quasi-static case, is justified by these dynamic computations. The second scenario deals with a larger initial damage ($l_0 = l_1 = 2.5l^c \geq l^c$) and we notice that after a first period of time of inactive micro-cracks ($\dot{l} = 0$) the strain-stress path, corresponding to OD in Figure 4.3 (right), reaches the equilibrium curve $\gamma = \Sigma^{eq}(\tau)$ in D. As in the first scenario, for high rates of deformations $\dot{\gamma} = 10^4 \text{s}^{-1}$ the strain-stress path is very different from the quasi-static paths, but for moderate rate of deformations $\dot{\gamma} = 1, 10, 10^2, 10^3 \text{s}^{-1}$ the strain-stress curves are almost rate independent and coincide with the quasi-static ones.

Notice that the strain rate sensitivity and the passage from dynamic to quasi-static process at the microscopic level, presented in Figure 4.3 left and explained here through a stability analysis, is not specific to NIC effective elasticity and to the similar growth model. Indeed, for the SCS effective elasticity and the wing crack-model Paliwal and Ramesh [95] and Hu et al. [63] obtained the same strain rate dependence with the same time "discontinuities" (see Figures 7 and 12 of [95] and Figure 7 of [63]).

4.5 Conclusions

We obtained stability criteria for dynamic and quasi-static processes at the microscopic scale. These criteria are rather general and they are related to a large class of damage models. We show that for a given continuous strain history the quasi-static or dynamic problems are instable or ill-posed (multiplicity of material responses) and whatever the selection rule is adopted, shocks (time discontinuities) will occur. We show that the quasi-static equilibria chosen by the "perfect delay convention" is always stable. The dynamic stability criterion coincides with the quasi-static one for weak inter-families interactions or for a single active family of micro-cracks.

These stability criteria are used to analyze the NIC effective elasticity associated to the self similar growth associated to some special configurations (one family of micro-cracks in mode I, II and III and in plane strain or plain stress). In each case we determine a critical crack density parameter and critical micro-crack radius (length) which distinguish between stable and unstable behaviors. This critical crack density depends only on the chosen configuration and on the Poisson ratio.

CHAPTER 5

THE HOMOGENOUS STRAIN-DRIVEN PROBLEM

We would like to analyze in this section only the constitutive assumptions (material behavior) regardless of the wave propagation. For that we will focus on the homogeneous problem (i.e. all the mechanical fields being independent of the spatial variables), also called the zero-dimensional problem. We have chosen the strain-driven processes (i.e. the strain evolution $t \to \boldsymbol{\varepsilon}(t)$ is prescribed) because they are easier to implement and there are no constitutive restrictions, as for a stress-driven problem. Since the associated (ordinary) differential equations are nonlinear and no analytical solutions is available, we will first develop a numerical scheme able to capture the material behavior even for unstable processes. This time integration technique of the damage constitutive law for a strain-driven process will be used later to develop the numerical scheme for the initial and boundary value problem.

First, let us recall first that a strain-driven process can be described only by a micro-scale time evolution. Indeed, for a given strain history $t \to \boldsymbol{\varepsilon}(t)$,with $\boldsymbol{\varepsilon}(0) = \boldsymbol{\varepsilon}_0$, we get from (3.4) and (3.2) that $t \to \rho_i(t),\ i = 1, .., N$ is the solution of the following nonlinear system of N differential equations

$$\frac{d}{dt}\rho_i(t) = \mathcal{L}^i(\rho_i, \mathcal{E}(\boldsymbol{\varepsilon}(t), \rho_1(t), .., \rho_N(t))), \qquad \text{for all } i = 1, .., N. \tag{5.1}$$

with the initial condition $\rho_1(0) = \rho_1^0, .., \rho_N(0) = \rho_N^0$.

5.1 Numerical approach

To integrate the differential system (5.1) over the time interval $[0, T^0]$ we consider m local (micro-scale) steps and $T^0 = m\delta t$, with δt the local (micro-scale) time step. Since the system of equations (5.1) could have unstable solutions it is necessary to use an implicit scheme. If we put $\rho_i^j = \rho_i(j\delta t)$ then the implicit time discretization (backward Euler scheme) of (5.1) reads:

$$\frac{\rho_i^{j+1} - \rho_i^j}{\delta t} = \mathcal{L}^i(\rho_i^{j+1}, \mathcal{E}(\boldsymbol{\varepsilon}((j+1)\delta t), \rho_1^{j+1}, .., \rho_N^{j+1})), \quad \text{for all } i = 1, .., N. \tag{5.2}$$

Let us notice that the above system of equation is nonlinear and we have to use some numerical algorithm to solve it at each time step. However, for weak inter-family micro-cracks interactions, i.e. for

$$\frac{\partial \mathcal{K}^i}{\partial \boldsymbol{\sigma}} : \frac{\partial \boldsymbol{\mathcal{E}}}{\partial \rho_k} \cong 0, \quad \text{for all } i \neq k,\ i, k = 1, .., N, , \tag{5.3}$$

or for a single family of micro-cracks ($N = 1$), the above nonlinear system could be replaced by a sequence of N nonlinear scalar equations as follows

$$\frac{\rho_i^{j+1} - \rho_i^j}{\delta t} = \mathcal{L}^i(\rho_i^{j+1}, \mathcal{E}(\boldsymbol{\varepsilon}((j+1)\delta t), \rho_1^j, ...\rho_{i-1}^j, \rho_i^{j+1}, \rho_{i+1}^j, ..., \rho_N^j)), \tag{5.4}$$

for all $i = 1, .., N$. In many cases the above nonlinear equation can be solved analytically, hence (5.4) is not computationally expensive.

The above numerical scheme will be used in the next section to compute the homogeneous solution for a single family of micro-cracks.

5.2 Single orientation micro-cracks

We suppose that all the micro-cracks have the same configuration and normal vector $\boldsymbol{n} = (1, 0, 0)$. Having in mind that we are looking for a zero-dimensional problem we shall denote by $\tau \geq 0$ the (generic) stress and by $\gamma \geq 0$ the (generic) strain (see table 4.1 for different configurations). For 0-D problems with constant strain rate the acceleration terms are vanishing, hence there are no inertial effects and we cannot distinguish between the dynamical and quasi-static macroscopic processes. At the microscopic level we analyze here only the

dynamic process with high or moderate rate of deformation.

Each element of the i-th family of micro-cracks has a different initial radius (half length) $l_i^0, i = 1, ..N$. The chosen effective elasticity law is the "non-interacting cracks method" (NIC) (Gambarotta and Lagomarsino [52] and Kachanov [69] and Appendix, chapter 17) and for the sake of simplicity we have considered only frictionless processes. The strain-stress equation (3.1) can be written as

$$\gamma = \mathcal{A}(\tau, l_1, .., l_N) = (A_0 + C \sum_{i=1}^{N} \rho(l_i))\tau \tag{5.5}$$

while (3.2) reads

$$\tau = \mathcal{E}(\gamma, l_1, .., l_N) = \frac{\gamma}{A_0 + C \sum_{i=1}^{N} \rho(l_i)}, \tag{5.6}$$

where A_0, C are compliance coefficients (see table 4.1).

The damage evolution law (5.1) is constructed, as in (3.5), from a quasi-static criterion $\mathcal{K} \leq 0$, associated to the micro-cracks self similar growth under a far field stress (4.2) (the stress intensity factor K given by (4.12) with a from table 4.1).

Figure 5.1: A schematic representation of the initial distribution of the micro-cracks. Left: single micro-cracks family model (F1). Right: 3 micro-cracks families model (F3). Note that the two models have the same damage, and the second model has an uniformly distributed damage on all three micro-crack types.

For a given strain rate $\dot{\gamma}$ and a given final γ^f we define the following loading/unloading process :

$$\gamma(t) = \begin{cases} t\dot{\gamma} & \text{if} \quad t \in [0, t^f], \\ \gamma^f - t\dot{\gamma} & \text{if} \quad t \in [t^f, 2t^f], \end{cases} \tag{5.7}$$

where $t^f = \gamma^f/\dot{\gamma}$ is the duration of both the loading and unloading processes. With this given strain evolution we have computed the stress τ and the evolution of the micro-cracks

length l_i from the ordinary differential system

$$\dot{l}_i = \varphi(\left[1 - \frac{K_c}{a\sqrt{l_i}\mathcal{E}(\gamma, l_1, .., l_N)}\right]_+), \quad \text{for all } i = 1, ...N, \tag{5.8}$$

using an Euler's backward method, described in the previous section.

In what follows we have used the following material settings corresponding to the anti-plane configuration for ceramics ($\nu_0 = 0.24, E_0 = 300$ GPa, and $K^c_{III} = 2.7$ MPa, $c_m = c_S, \varphi(x) = x$, which will generate the coefficients A_0, C and a through Table 4.1) but the results are not qualitatively different in other configurations for other brittle materials.

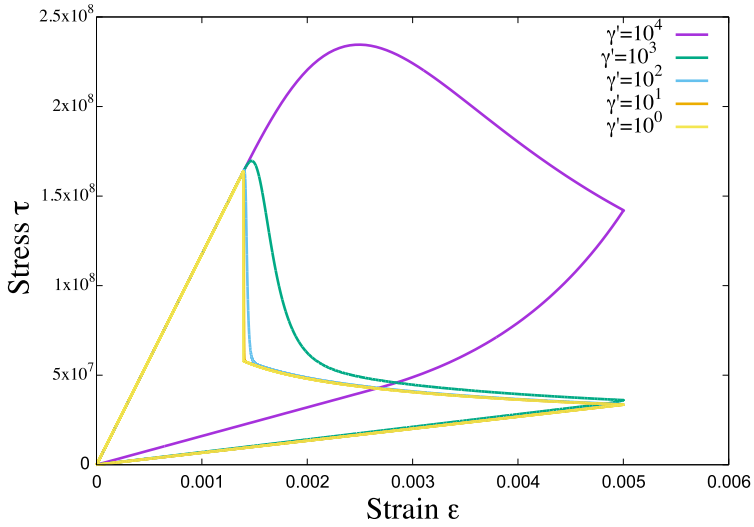

Figure 5.2: Stress (in Pa) versus strain for a strain driven loading/unloading process of a single family model (F1) under different strain rates $\dot{\gamma} = 10^4, 10^3, 10^2, 10^1 \text{s}^{-1}$ and $\dot{\gamma} = 1\text{s}^{-1}$.

5.2.1 One family of micro-cracks

First, we have considered model F1, that is, a single family ($N = 1$, see Figure 5.1 left) of micro-cracks with the flaw density $\eta = 10^6/(2\pi)\text{m}^{-2}$ and the initial the half-length l^0 was chosen such that the material is almost undamaged at the initial state $\rho^0 = 0.016$ and the process is unstable ($l^0 < l_c$). For a given final strain $\gamma^f = 0.005$ we have considered five strain rates $\dot{\gamma} = 10^4\text{s}^{-1}$, $\dot{\gamma} = 10^3\text{s}^{-1}$, $\dot{\gamma} = 10^2\text{s}^{-1}$, $\dot{\gamma} = 10\text{s}^{-1}$ and $\dot{\gamma} = 1\text{s}^{-1}$. The numerical results

were plotted in Figure 5.2. For a first period of time, the micro-cracks are inactive ($\dot{l} = 0$) and the strain-stress path is linear and rate-independent. We see that in all cases, strain-stress paths have a (unstable) softening part due to the damage evolution. For high rates of deformations $\dot{\gamma} = 10^3, 10^4 \text{s}^{-1}$ the softening process is very different from the moderate rate of deformations $\dot{\gamma} = 1, 10^2 \text{s}^{-1}$. This is due to the fact that for moderate strain rate the micro-scale time-scale is very small with respect to the loading time scale (macro-scale). In this case the micro-cracks (damage) growth is very rapid, giving a "discontinuous", rate independent strain-stress path. For high strain rates the softening process due to micro-cracks growth is compensated by the loading process giving a smooth, rate dependent, strain-stress path. For more details and discussion on this unstable material behavior see the previous chapter.

This strain rate sensitivity, presented in Figure 5.2 is not specific to NIC effective elasticity and to the self similar growth model. Indeed, for the SCS effective elasticity and the wing crack-model Paliwal and Ramesh [95] and Hu et al. [63] obtained the same type of strain rate dependence (see Figures 7 and 12 of [95] and Figure 7 of [63]).

As it follows from Katcoff and Graham-Brady [73] the distribution of flaw sizes is very important at moderate strain rate and the presence of large flaws control the dynamic strength of the material. On the contrary, at very high strain rates, crack growth is activated even in small flaws and therefore the flaw density is controlling the dynamic strength.

In conclusion, for a single family of micro-cracks the rate of deformation plays a major role. For intermediate and low rates of deformation, sharp stress drops related to the material instabilities could be expected, and the strain-stress curve is not very sensitive on the strain rate. On the contrary, for high rates of deformation, the strain-stress curve depends strongly on the rate of deformation but only a smooth stress drop is expected.

5.2.2 Three families of micro-cracks

In a second numerical experiment called model F3, we have considered three families of micro-cracks ($N = 3$, see Figure 5.1 rigth), with the initial lengths $l_1^0 = l^0, l_2^0 = l^0/2, l_3^0 = 2l^0$. The flaw density $\eta_1 = \eta/3, \eta_2 = 4\eta/3, \eta_3 = \eta/12$ was chosen such that $\rho_i^0 = \eta_i (l_i^0)^2 = \rho^0/3$, hence the specimen has the same initial damage uniformly distributed on all three micro-crack types.

he strain versus the stress (in Pa) for a strain driven loading/unloading process of a single family model (F1) under different strain rates $\dot{\gamma} = 10^4, 10^3, 10^2, 10^1 \text{s}^{-1}$ and $\dot{\gamma} = 1 \text{s}^{-1}$.

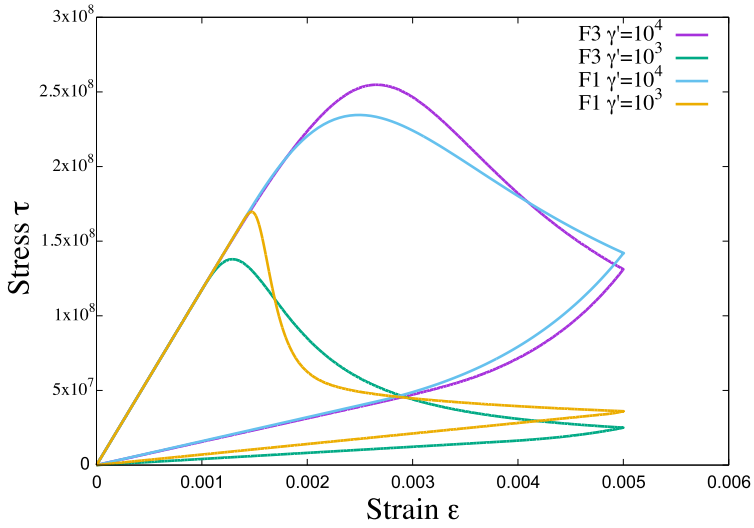

Figure 5.3: Stress (in Pa) versus strain of a strain driven loading/unloading process with models F1 and F3 for two different strain rates $\dot{\gamma} = 10^3 \mathrm{s}^{-1}$ and $\dot{\gamma} = 10^4 \mathrm{s}^{-1}$.

We have done computations for two rates of deformation ($\dot{\gamma} = 10^3 \mathrm{s}^{-1}$ and $\dot{\gamma} = 10^4 \mathrm{s}^{-1}$ and we compared models F1 and F3 presented in the previous subsection. For the lowest strain rate we remark that only the largest micro-crack system (number 3) of model F3 is activated, much earlier than the micro-crack of model F1. However, even with only one activated micro-crack type the total damage is larger for model F3 than for model F1. This can be seen in Figure 5.3 where we have compared the two models (in red and blue) in a strain-stress representation. For the highest rate of deformation the situation is different. In this case 2 micro-crack systems (1 and 3) of model F3 are activated but the overall damage is less than in model F1 (see Figure 5.3 green and magenta curves) . This can be explained by the fact that the time period between the activation of the systems 3 and 1 is much shorter, hence the difference between them are dominated by the flaw density η.

5.3 Conclusions

We proposed a semi-implicit numerical scheme to integrate the (ordinary) differential equations associated to homogeneous strain-driven processes of a damage constitutive law. We used this numerical scheme to investigate some simple damage problems. We found that for

a single family of micro-cracks the rate of deformation plays a major role. For intermediate and low rates of deformation, sharp stress drops related to the material instabilities could be expected, and the strain-stress curve is not very sensitive on the strain rate. On the contrary, for high rates of deformation, the strain-stress curve depends strongly on the rate of deformation but only a smooth stress drop is expected. The role played by the rate of deformation is much more complex if more families of micro-cracks are considered. As a matter of fact, the damage evolution is driven not only by the initial micro-crack densities but also by the initial micro-cracks lengths (or flaw densities). There exists a subtile interplay between the rate of deformation and the distribution of the micro-cracks lengths, even with the same spatial orientation.

CHAPTER 6

NUMERICAL APPROACH

The aim of this chapter is to introduce a new numerical scheme associated to the boundary value problem of the wave propagation in a damaged material described by a rather general (local) damage constitutive law. To solve this nonlinear hyperbolic problem we will adapt here the second order scheme proposed by Etienne et al. [46]. The explicit leapfrog scheme used for the time discretization deals with the velocity and the strain fields and not with the stress fields, as it is usual in a velocity-stress formulation. This technique permits us to use the effective elasticity constitutive law and not its time derivative. Using this specific time discretization during a (macro-scale) time step the constitutive damage law becomes a strain driven homogeneous problem, which was studied in the previous section. To capture the instabilities we use here a semi-implicit Euler method and a micro-scale time step to integrate it. For the flux choice a centered scheme will be considered.

6.1 The continuous boundary value problem

We consider the deformation of an elastic body occupying, in the initial unconstrained configuration, a domain $\mathcal{D}$ in $\mathbb{R}^3$ not necessarily bounded. Its boundary $\partial\mathcal{D}$ is supposed to be smooth and divided into two disjoint parts: denoted Σ_v and Σ_s. We denote the displacement field by $\boldsymbol{u} = (u_x, u_y, u_z)$, the velocity filed by $\boldsymbol{v} = \dot{\boldsymbol{u}}$ and by $\boldsymbol{\varepsilon} = (\nabla\boldsymbol{u} + \nabla^T\boldsymbol{u})/2$ the small strain tensor. If we denote by ρ^{mass} the mass density, the momentum balance law can be

written as:

$$\rho^{mass}\dot{\boldsymbol{v}}(t) = \text{div}\ \boldsymbol{\sigma}(t) + \rho^{mass}\boldsymbol{b}(t) \quad \text{in} \ \ \mathcal{D}, \tag{6.1}$$

where $\rho^{mass}\boldsymbol{b}$ are the volume forces, while the rate of deformation is given by

$$\dot{\boldsymbol{\varepsilon}}(t) = \boldsymbol{\varepsilon}(\boldsymbol{v}(t)) = \frac{1}{2}(\nabla \boldsymbol{v}(t) + \nabla^T \boldsymbol{v}(t)) \quad \text{in} \quad \mathcal{D}. \tag{6.2}$$

We complete the above general equations with the damage model presented in the previous section,

$$\boldsymbol{\sigma}(t) = \boldsymbol{\mathcal{E}}(\boldsymbol{\varepsilon}(t), \rho_1(t), ..., \rho_N(t)), \tag{6.3}$$

$$\dot{\rho}_i(t) = \mathcal{L}^i(\rho_i(t), \boldsymbol{\sigma}(t)), \quad \text{for all } i = 1, .., N. \tag{6.4}$$

We complete the field equations with some boundary conditions

$$\boldsymbol{v}(t) = \boldsymbol{V}(t) \ \ \text{on} \quad \Sigma_v, \quad \boldsymbol{\sigma}(t)\boldsymbol{n} = \boldsymbol{S}(t) \ \ \text{on} \quad \Sigma_s, \tag{6.5}$$

where $\boldsymbol{n}$ is the outward unit normal to $\partial\mathcal{D}$, and the initial conditions

$$\boldsymbol{v}(0) = \boldsymbol{v}^0, \quad \boldsymbol{\varepsilon}(0) = \boldsymbol{\varepsilon}^0, \quad \rho_i(0) = \rho_i^0, \qquad i = 1, ..N. \tag{6.6}$$

The initial and boundary value with anisotropic damage can be formulated now as follows: find the velocity $\boldsymbol{v} : [0,T] \times \mathcal{D} \to \mathbb{R}^3$, the stress $\boldsymbol{\sigma} : [0,T] \times \mathcal{D} \to \mathbb{R}^{3\times 3}_S$, the strain $\boldsymbol{\varepsilon} : [0,T] \times \mathcal{D} \to \mathbb{R}^{3\times 3}_S$ and the crack-density parameters $\rho_i : [0,T] \times \mathcal{D} \to \mathbb{R}_+$, for $i = 1, ..N$ solution of (6.1)-(6.3) with the boundary conditions (6.5) and the initial conditions (6.6).

6.2 Time discretization

For the time discretization, we adopt a second-order explicit leap-frog scheme that allows to compute alternatively the velocity and the stress components from one half time step to the next. To this end, let $\Delta t > 0$ be the time step, M the maximum number of steps, and $T = M\Delta t$, with Δt the (macro-scale) time step. We denote by $\boldsymbol{u}^k, \boldsymbol{v}^k$ the discretization of the displacement and velocity at time $t = k\Delta t$ and by $\boldsymbol{\sigma}^{k+\frac{1}{2}}, \boldsymbol{\varepsilon}^{k+\frac{1}{2}}, \rho_i^{k+\frac{1}{2}}$ the stress, strain and crack density parameters at time $t = (k+\frac{1}{2})\Delta t$. The equations (6.1) and (6.2) are discretized

in time as

$$\frac{\rho^{mass}}{\Delta t}(\boldsymbol{v}^k - \boldsymbol{v}^{k-1}) = \text{div}\ \boldsymbol{\sigma}^{k-\frac{1}{2}} + \rho^{mass}\boldsymbol{b}^{k-\frac{1}{2}} \quad \text{in} \quad \mathcal{D}, \tag{6.7}$$

$$\frac{1}{\Delta t}\left(\boldsymbol{\varepsilon}^{k+\frac{1}{2}} - \boldsymbol{\varepsilon}^{k-\frac{1}{2}}\right) = \boldsymbol{\varepsilon}(\boldsymbol{v}^k) = \frac{1}{2}(\nabla \boldsymbol{v}^k + \nabla^T \boldsymbol{v}^k) \quad \text{in} \quad \mathcal{D}. \tag{6.8}$$

To get the stress $\boldsymbol{\sigma}^{k+\frac{1}{2}}$ we have to integrate the constitutive equation (6.3) over the time interval $[(k-\frac{1}{2})\Delta t, (k+\frac{1}{2})\Delta t]$. Since the strain $\boldsymbol{\varepsilon}^{k+\frac{1}{2}}$ is already computed we are dealing with a material strain-driven process, described in the previous section. The algorithm used here, similar to the returning map algorithm in plasticity, was already described for homogeneous processes.

The (macro-scale) time interval $[(k-\frac{1}{2})\Delta t, (k+\frac{1}{2})\Delta t]$ is divided into m (micro-scale) time steps δt with $\Delta t = m\delta t$. If we put $\rho_i^{k-\frac{1}{2},0} = \rho_i^{k-\frac{1}{2}}, \boldsymbol{\sigma}^{k-\frac{1}{2},0} = \boldsymbol{\sigma}^{k-\frac{1}{2}}$ and we interpolate the strains as

$$\boldsymbol{\varepsilon}^{k-\frac{1}{2},j} = \boldsymbol{\varepsilon}^{k-\frac{1}{2}} + \frac{j\delta t}{\Delta t}(\boldsymbol{\varepsilon}^{k+\frac{1}{2}} - \boldsymbol{\varepsilon}^{k-\frac{1}{2}})$$

then the sequence of nonlinear equations (5.4) reads

$$\frac{\rho_i^{k-\frac{1}{2},j} - \rho_i^{k-\frac{1}{2},j-1}}{\delta t} = \mathcal{L}^i(\rho_i^{j+1}, \mathcal{E}(\boldsymbol{\varepsilon}^{k-\frac{1}{2},j}, \rho_1^{j-1}, ...\rho_{i-1}^{j-1}, \rho_i^j, \rho_{i+1}^{j-1}, ..., \rho_N^{j-1})), \tag{6.9}$$

for all $i = 1, .., N$. The stress field is computed after we have computed all the micro-cracks densities $\rho_i^{k-\frac{1}{2},j}$ from

$$\boldsymbol{\sigma}^{k-\frac{1}{2},j} = \boldsymbol{\mathcal{E}}(\boldsymbol{\varepsilon}^{k-\frac{1}{2},j}, \rho_1^{k-\frac{1}{2},j}, .., \rho_N^{k-\frac{1}{2},j}). \tag{6.10}$$

At the end of the macro-scale time interval $[(k-\frac{1}{2})\Delta t, (k+\frac{1}{2})\Delta t]$ we put $\rho_i^{k+\frac{1}{2}} = \rho_i^{k-\frac{1}{2},m}$ and $\boldsymbol{\sigma}^{k+\frac{1}{2}} = \boldsymbol{\sigma}^{k-\frac{1}{2},m}$.

6.3 Space discretization

In order to achieve the spatial discretization of the partial differential equations (6.7),(6.8) let $\mathcal{D}$ be discretized with a family of tetrahedra $\mathcal{T}_h$,h denoting the mesh size . The discretization space W_h for the velocities $\boldsymbol{v}^k$, strains $\boldsymbol{\varepsilon}^{k+\frac{1}{2}}$, stresses $\boldsymbol{\sigma}^{k+\frac{1}{2},j}$ and micro-cracks density parameters $\rho^{k+\frac{1}{2},j}$ is associated to the discontinuous Galerkin method. The functions $\varphi \in W_h$ are polynomial functions of degree d on each tetrahedron $T \in \mathcal{T}_h$, but may be discontinuous between two tetrahedra.

Let us fix the time iteration k. If we multiply (6.7) by $\boldsymbol{\varphi} \in W_h^3$ and (6.8) by $\boldsymbol{\Psi} \in W_h^{3\times 3}$, and we make use of Green formula, then the variational problem on each tetrahedron $T \in \mathcal{T}_h$ of the domain $\mathcal{D}$ reads:

$$\int_T \left[\frac{\rho^{mass}}{\Delta t}(\boldsymbol{v}^k - \boldsymbol{v}^{k-1}) \cdot \boldsymbol{\varphi} + \boldsymbol{\sigma}^{k-\frac{1}{2}} : \boldsymbol{\varepsilon}(\boldsymbol{\varphi}) \right] \, dv = \int_T \rho^{mass} \boldsymbol{b}^{k-\frac{1}{2}} \cdot \boldsymbol{\varphi} \, dv + \int_{\partial T} \mathcal{F}_\sigma^{k-\frac{1}{2}} \cdot \boldsymbol{\varphi} \, da, \quad (6.11)$$

$$\int_T \left[\frac{1}{\Delta t} \left(\boldsymbol{\varepsilon}^{k+\frac{1}{2}} - \boldsymbol{\varepsilon}^{k-\frac{1}{2}} \right) : \boldsymbol{\Psi} + \boldsymbol{v}^k \cdot \mathrm{div}(\boldsymbol{\Psi}) \right] \, dv = \int_{\partial T} \boldsymbol{\Psi} \boldsymbol{n} \cdot \mathcal{F}_v^k \, da \quad (6.12)$$

where $\boldsymbol{n}$ is the unit outward normal along the boundary ∂T of T and $\mathcal{F}_\sigma^{k-\frac{1}{2}}, \mathcal{F}_v^k$ are the stress and velocity fluxes. The above problems can be solved with a discontinuous Galerkin technique by using a specific choice of the flux appearing in the right hand side of (6.11) and (6.12). Here we have chosen the centered flux scheme which has very good non-dissipative properties (see BenJemaa et al. [19], Delcourte et al. [31], Etienne et al [46]):

$$\mathcal{F}_v^k = \boldsymbol{v}^k + \frac{1}{2}[\boldsymbol{v}]^{k+1}, \qquad \text{on} \;\; \partial T \cap \mathcal{D}, \quad (6.13)$$

$$\mathcal{F}_\sigma^{k-\frac{1}{2}} = (\boldsymbol{\sigma}^{k-\frac{1}{2}} + \frac{1}{2}[\boldsymbol{\sigma}]^{k-\frac{1}{2}})\boldsymbol{n}, \qquad \text{on} \;\; \partial T \cap \mathcal{D}, \quad (6.14)$$

where $[\boldsymbol{\sigma}]$ and $[\boldsymbol{v}]$ denote the jump of $\boldsymbol{\sigma}$ and $\boldsymbol{v}$ across the boundary of T. Following this choice and using the boundary conditions (6.5) we get the following variational equations

$$\int_{\mathcal{D}} \left[\frac{\rho}{\Delta t}(\boldsymbol{v}^k - \boldsymbol{v}^{k-1}) \cdot \boldsymbol{\varphi} + \boldsymbol{\sigma}^{k-\frac{1}{2}} : \boldsymbol{\varepsilon}(\boldsymbol{\varphi}) \right] \, dv = \sum_{T \in \mathcal{T}_h} \int_{\partial T \setminus \partial \mathcal{D}} \mathcal{F}_\sigma^{k-\frac{1}{2}} \cdot \boldsymbol{\varphi} \, da + \quad (6.15)$$

$$\int_{\mathcal{D}} \rho^{mass} \boldsymbol{b}^{k-\frac{1}{2}} \cdot \boldsymbol{\varphi} \, dv + \int_{\Sigma_s} \boldsymbol{\varphi} \cdot \boldsymbol{S}((k-\frac{1}{2})\Delta t) \, da + \int_{\Sigma_v} \boldsymbol{\varphi} \cdot \boldsymbol{\sigma}^{k-\frac{1}{2}} \boldsymbol{n} \, da,$$

$$\int_\Omega \left[\frac{1}{\Delta t} \left(\boldsymbol{\varepsilon}^{k+\frac{1}{2}} - \boldsymbol{\varepsilon}^{k-\frac{1}{2}} \right) : \boldsymbol{\Psi} + \boldsymbol{v}^k \cdot \mathrm{div}(\boldsymbol{\Psi}) \right] \, dv = \sum_{T \in \mathcal{T}_h} \int_{\partial T \setminus \partial \mathcal{D}} \mathcal{F}_v^k \cdot \boldsymbol{\Psi} \boldsymbol{n} \, da + \quad (6.16)$$

$$\int_{D_v} \boldsymbol{V}(k\Delta t) \cdot \boldsymbol{\Psi} \boldsymbol{n} \, da + \int_{D_s} \boldsymbol{v}^k \cdot \boldsymbol{\Psi} \boldsymbol{n} \, da,$$

for all $\boldsymbol{\varphi} \in W_h^3$ and all $\boldsymbol{\Psi} \in W_h^{3\times 3}$.

Concerning the Courant-Friedrichs-Lewy (CFL) condition, which links the mesh width and the time step to guarantee numerical stability, there is no mathematical proof for unstruc-

tured meshes associated to the second-order explicit leap-frog scheme used here. However, a heuristic stability criterion, that usually works well, was found by Kaser et al. [72]

$$\Delta t < \frac{1}{2d+1} \min_{T \in \mathcal{T}_h} \frac{2r(T)}{c_P(T)}, \tag{6.17}$$

where $r(T)$ is the radius of the sphere inscribed in the element T and $c_P(T)$ is the P-wave velocity in the element T. For structured or uniform meshes we will denote by CFL the non-dimensional parameter

$$CFL = \frac{\Delta t}{h} c_0, \tag{6.18}$$

where c_0 is the reference wave velocity of the process.

Let us summarize here the proposed numerical algorithm at each time step k. First, we compute $\boldsymbol{v}^k$ from (6.15), then we use it to compute $\boldsymbol{\varepsilon}^{k+\frac{1}{2}}$ from (6.16). Finally, we make use of the strain $\boldsymbol{\varepsilon}^{k+\frac{1}{2}}$ to compute $\boldsymbol{\sigma}^{k+\frac{1}{2}}$ and $\rho_i^{k+\frac{1}{2}}$ from the iterative scheme (6.9)-(6.10).

6.4 Testing the numerical approach

To test the numerical scheme proposed in this chapter we would like to compare the computed solution with an exact (analytical) one. As far as we know there are no (nontrivial) analytical solutions for the wave propagation in a material modeled with a damage constitutive law. That is why we will construct first a one dimensional problem for which we can have an exact solution with a specific choice of the volume forces. Since the role played by the strain rate is essential in mechanical modeling, as well in the numerical integration, we discuss here the numerical accuracy for different strain rates. Using specific dimensionless variables we will compare different exact solutions associated to different strain rates.

6.4.1 Exact solution

The aim of this subsection is to construct an exact (analytical) solution of the wave propagation problem with damage to test the numerical scheme presented in this chapter. For that we will suppose that we deal with a single family of micro-cracks ($N = 1$). The starting point will be the strain-driven homogeneous problem studied before. Let $s \to \gamma^0(s)$ be the given (generic) strain pulse of length 2δ (i.e. $\gamma^0(s) = 0$ for $s \leq 0$ or $s \geq 2\delta$) and let

$s \to \tau^0(s)$ be the (generic) stress (see Table 4.1 for the expressions of γ^0 and τ^0 in different configurations). We suppose that no frictional or unilateral phenomenon occurs and we will assume a linear stress-strain law $\tau = \mathcal{E}(\gamma, \rho) = \mathcal{E}(\rho)\gamma$. We denote by $s \to \rho^0(s)$ the solution of the following ordinary differential equation modeling the damage evolution

$$\frac{d}{ds}\rho^0(s) = \mathcal{L}(\mathcal{E}(\rho(s))\gamma^0(s), \rho(s)), \qquad \rho^0(0) = \rho_0, \tag{6.19}$$

where ρ_0 is the initial damage. The solution of this differential equation can be found analytically or numerically. In the latter case one can use the (implicit) backward Euler method described in the previous chapter. Since it is computationally non-expensive it can be done with a very small time step such that the error of the numerical integration is very small with respect to the error expected for the wave propagation problem. That is why, even obtained numerically $s \to \rho^0(s)$ could be considered as an "exact" (analytical) solution. Then the exact stress evolution $s \to \tau^0(s)$ could be obtained from $\tau^0(s) = \mathcal{E}(\rho^0(s))\gamma^0(s)$.

Let x be the generic one-dimensional space variable and let $(0, L)$ be the spatial domain, while the strain rate relationship reads

$$\dot{\gamma}(t, x) = \beta \partial_x v(t, x),$$

where β is the non dimensional parameter corresponding to the choice off the configuration ($\beta = 1$ for the mode I and $\beta = 1/2$ in mode II or mode III). The time interval will be denoted by $[0, T]$, where $T = L/c_0$ and $c_0 = \sqrt{\mathcal{E}(0)\beta/\rho^{mass}}$ is the (generic) wave speed in the undamaged material. Let us denote by

$$v^{ex}(t, x) = -c_0\gamma^0(t - x/c_0), \quad \tau^{ex}(t, x) = \tau^0(t - x/c_0),$$

$$\gamma^{ex}(t, x) = \gamma^0(t - x/c_0), \quad \rho^{ex}(t, x) = \rho^0(t - x/c_0),$$

the exact solution that we are looking for. Even if it is constructed from the homogeneous problem and using the characteristics method the above solution does not satisfy the momentum balance law in the absence of the volumetric forces. Indeed,

$$\rho^{mass}\dot{v}^{ex} = \frac{\partial}{\partial x}(\mathcal{E}(0)\beta\gamma^{ex}) \neq \frac{\partial}{\partial x}\tau^{ex}$$

but it could satisfy the momentum balance law with an appropriate choice of the volume force

$f = \frac{\partial}{\partial x}(\beta\mathcal{E}(0)\gamma^{ex} - \tau^{ex})$. This volume force could be easily computed from the homogeneous solution as

$$f(t,x) = -\frac{1}{c_0} b(t - x/c_0), \tag{6.20}$$

where

$$b(s) = [\beta\mathcal{E}(0) - \mathcal{E}(\rho^0(s))]\frac{d}{ds}\gamma^0(s) - \frac{d\mathcal{E}(\rho^0(s))}{d\rho}\mathcal{L}(\mathcal{E}(\rho(s))\gamma^0(s), \rho(s))\gamma^0(s).$$

Finally we get that $v^{ex}, \tau^{ex}, \gamma^{ex}$ and ρ^{ex} is the solution of the following one dimensional system of equations

$$\begin{cases} \rho^{mass}\dot{v}(t,x) & = \partial_x\tau(t,x) + f(t,x), \\ \dot{\gamma}(t,x) & = \beta\partial_x v(t,x), \\ \tau(t,x) & = \mathcal{E}(\rho(t,x))\gamma(t,x), \\ \dot{\rho}(t,x) & = \mathcal{L}(\rho(t,x), \tau(t,x)), \end{cases} \tag{6.21}$$

with the boundary and initial conditions

$$v(t,0) = -c_0\gamma^0(t), \quad v(t,L) = 0, \tag{6.22}$$

$$v(0,x) = 0, \quad \gamma(0,x) = 0, \quad \rho(0,x) = \rho_0. \tag{6.23}$$

For the effective elasticity law obtained using the "non-interacting cracks method" (NIC) and without any unilateral or frictional effects (traction in mode I or frictionless in mode II or III) the expression of the the the compliance $\mathcal{E}$ is

$$\gamma = \mathcal{A}(\rho)\tau = (A_0 + C\rho(l))\tau, \quad \tau = \mathcal{E}(\rho)\gamma = \frac{1}{A_0 + C\rho(l)}\gamma,$$

where A_0, C are compliance coefficients (see table 4.1).

If the damage evolution law is associated to the micro-cracks self similar growth under a far field stress (4.2) and without any unilateral or frictional effects the stress intensity factor K has a simple expression

$$\mathcal{K}(l,\tau) = \frac{K(l,\tau)}{K_c} - 1, \qquad K(l,\tau) = a\sqrt{l}\tau$$

where a is a non-dimensional number (see table 4.1). The dynamic evolution law for the

damage parameter ρ can be replaced by an evolution law for the crack-length l and the one dimensional evolution equation (6.21) reads

$$\begin{cases} \rho^{mass}\dot{v}(t,x) &= \partial_x\tau(t,x) + f(t,x), \\ \dot{\gamma}(t,x) &= \beta\partial_x v(t,x), \\ \tau(t,x) &= \dfrac{1}{A_0 + C\rho(l(t,x))}\gamma(t,x), \\ \dot{l}(t,x)(t,x) &= c_m\varphi(\left[\dfrac{a\sqrt{l(t,x)}\tau(t,x) - K_c}{(\alpha-1)K_c + a\sqrt{l(t,x)}\tau(t,x)}\right]_+), \end{cases} \tag{6.24}$$

while the initial conditions (6.23) have to be replaced by

$$v(0,x) = 0, \quad \gamma(0,x) = 0, \quad l(0,x) = l_0. \tag{6.25}$$

6.4.2 Strain rate sensitivity

We want to see here the strain rate influence on the exact solution constructed before. For that let $\dot{\Gamma}$ be the strain rate and we denote by γ^f the given final strain. To compare the solutions we have to use non-dimensional variables and functions, but for the sake of simplicity we will use the same notations. For instance, instead of ρ^{mass} we use $\rho^{mass}\rho_c^{mass}$ where ρ_c^{mass} is the characteristic mass density and ρ^{mass} is the non-dimensional density. We proceed in the same way with $t \to tT_c$, $x \to xL_c^{macro}$, $v \to vV_c$, $\tau \to \tau S_c$, $l \to lL_c^{micro}$ and $f \to ff_c$. If we take the following (natural) choices for the characteristic variables

$$T_c = \frac{\gamma^f}{\dot{\Gamma}}, \quad S_c = \frac{1}{A_0}, \quad V_c = \sqrt{\frac{S_c}{\beta\rho_c^{mass}}}, \quad L_c^{macro} = V_cT_c, \quad L_c^{micro} = l(\rho_c), \quad f_c = \frac{\rho_c^{mass}V_c}{T_c},$$

then the system (6.24) reads

$$\begin{cases} \rho^{mass}\dot{v}(t,x) &= \partial_x\tau(t,x) + f(t,x), \\ \dot{\gamma}(t,x) &= \beta\partial_x v(t,x), \\ \tau(t,x) &= \dfrac{1}{1 + C\rho(l(t,x))/A_0}\gamma(t,x), \\ \dot{l}(t,x) &= \dfrac{c_m\gamma^f}{L_c^{micro}\dot{\Gamma}}\varphi(\left[\dfrac{a\sqrt{l(t,x)}\tau(t,x) - K_cA_0/L_c^{micro}}{(\alpha-1)K_cA_0/L_c^{micro} + a\sqrt{l(t,x)}\tau(t,x)}\right]_+). \end{cases} \tag{6.26}$$

Using this non-dimensional system we can compare now different exact solution on the same (non-dimensional) space $x \in (0,1)$ and on the same (non-dimensional) time $t \in (0,1)$ but associated to different processes, related to different strain rates $\dot{\Gamma}$. We notice that the structure of the system is unchanged with exception of the last equation related to the crack-growth which is directly dependent on the strain rate $\dot{\Gamma}$. The stiffness of this last differential equation is related to the non dimensional number M_Q, called here the "microscopic evolution index",

$$M_Q = \frac{c_m \gamma^f}{L_c^{micro} \dot{\Gamma}} \tag{6.27}$$

which discriminate, at the microscopic scale, a quasi-static from a dynamic behavior. For small values of M_Q we deal with a dynamic process while for large values of M_Q the macroscopic time scale is too large to capture the micro-scale evolution, hence the process is quasi-static (see the discussion given in the first chapter of this part) .

Using the above one-dimensional solution one can construct two dimensional or three dimensional analytical solutions. For instance, for the anti-plane configuration considered in what follows, we put $\mathcal{D} = (0,L) \times (0,H) \times R$ to get that $v_z(t,x,y) = v^{ex}(t,x), \sigma_{xz}(t,x,y) = \tau^{ex}(t,x), \sigma_{yz}(t,x,y) = 0, \epsilon_{xz}(t,x,y) = \gamma^{ex}(t,x)$ and $\epsilon_{yz}(t,x,y) = 0$ is a the exact solution for the boundary value problem with vanishing tangential stress on $y = 0$ and $y = H$.

We have computed the exact solution for different strain rates in the anti-plane configuration, corresponding to mode III for ceramics ($\nu_0 = 0.24, E_0 = 300$ GPa, $\rho^{mass} = 3673$ kg m^{-3}, $c_0 = c_S = \sqrt{G_0/\rho^{mass}}$, $K^c_{III} = 2.7$ MPa$\sqrt{\text{m}}, \eta = 10^6/2\pi\text{m}^{-2}$). The strain pulse was chosen to be $\gamma^0(t) = \gamma^f \varphi_\delta(t-\delta)$, with $\varphi_\delta(s) = (\cos(s\pi/\delta)+1)/2$ if $|s| \leq \delta$ and $\varphi_\delta(s) = 0$ if $|s| > \delta$ and $\gamma^f = 0.005$. The initial micro-crack length was chosen to be $l_0 = \sqrt{\rho_c/(3\eta)}$ corresponding to a crack density $\rho_0 = \rho_c/3$, where ρ_c is the critical crack density ($\rho_c = 1/6\pi$ in the anti-plane case). Following the analysis given in section 4.4.2 the process has a material instability.

In figure 6.1 we have plotted the spatial distribution of the exact stress $x \to \tau^{ex}(t,x)$ for different strain rates. We remark an important sensitivity with respect to the strain rate: the pulse loses its amplitude when the strain rate is decreasing. However, starting to $\dot{\Gamma} = 10^2\text{s}^{-1}$ the role of the strain rate is less important and we can speak on a rate independent model (no differences between $\dot{\Gamma} = 10^1\text{s}^{-1}$ and $\dot{\Gamma} = 1\text{s}^{-1}$). Since the microscopic evolution index M_Q varies from $M_Q = 4969.98$ for $\dot{\Gamma} = 10\text{s}^{-1}$ to $M_Q = 4.96998$ for $\dot{\Gamma} = 10^4\text{s}^{-1}$ one can deduce from the above discussion that for small values of the strain rate the process is

quasi-static at the microscopic scale, but it is still dynamic at the macroscopic scale. In our case the critical microscopic evolution index M_Q^c, which discriminate the dynamic from the quasi-static micro-scale behavior, is around of

$$M_Q^c = 50,$$

i.e. for $M_Q < M_Q^c$ we deal with a micro-scale dynamic process while for $M_Q \geq M_Q^c$ we have to use a micro-scale quasi-static model.

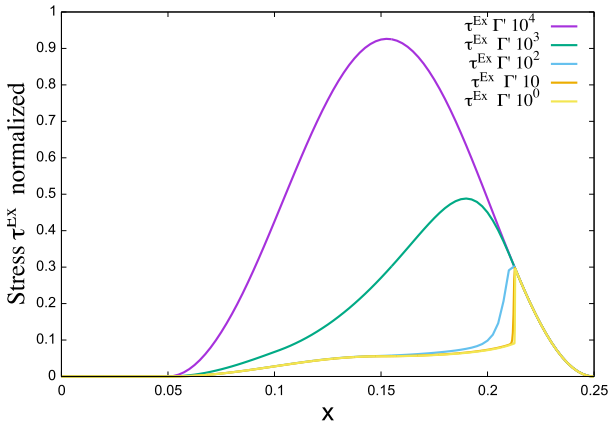

Figure 6.1: The transition from dynamic to quasi-static microscopic process. The spatial distribution of the exact stress pulse $x \to \tau^{ex}(t,x)$ for different strain rates: $\dot{\Gamma} = 1, 10, 10^2, 10^3, 10^4 \mathrm{s}^{-1}$.

6.4.3 Mesh/Time step analysis

In section we focus on the analysis of the mesh/time step sensitivity of the numerical solution in connection with role played by the strain rate. Since the exact solution was constructed with a volume forces f which is associated through (6.20) to a wave propagating with the speed c we cannot distinguish between the role played by the mesh size and the time step. That is why we have considered here that the micro-scale time step is equal to the macro-scale time step, $\delta t = \Delta t$, and we fixed the CFL constant to be $CFL = 0.1$, i.e. $\Delta t = h/10$, where h is the size of an uniform mesh.

Using the non-dimensional settings of the previous section all the solutions, associated to different strain rates, are computed on the same space interval $(0, 1)$ during the same time

interval $(0, 1)$.

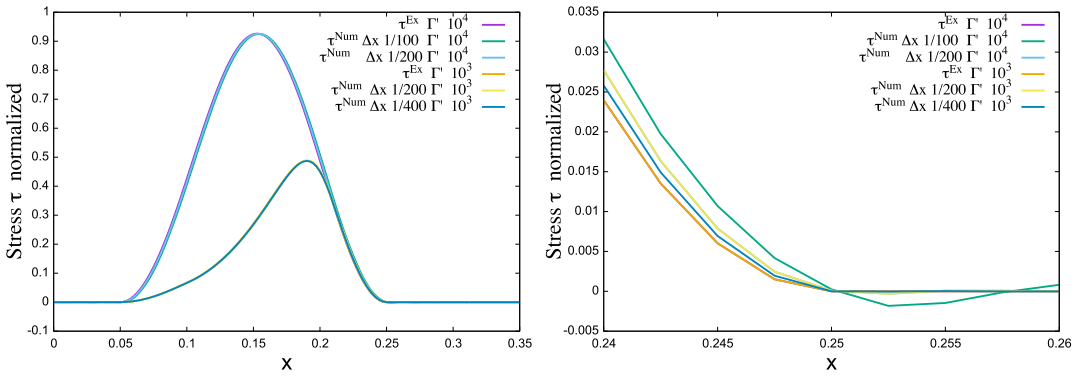

Figure 6.2: Micro-scale dynamic process ($\dot{\Gamma} = 10^3, 10^4 \text{s}^{-1}$): the spatial distribution of the computed stress $x \to \tau(t, x)$ and of the exact stress $x \to \tau^{ex}(t, x)$. For $\dot{\Gamma} = 10^4 \text{s}^{-1}$ the computed stress with $h = 10^{-2}(\Delta t = 10^{-3})$ and with $h = 0.5 \cdot 10^{-2}(\Delta t = 0.5 \cdot 10^{-3})$. For $\dot{\Gamma} = 10^3 \text{s}^{-1}$ the computed stress with $h = 10^{-2}(\Delta t = 10^{-3})$, $h = 0.5 \cdot 10^{-2}(\Delta t = 0.5 \cdot 10^{-3})$ and with $h = 0.25 \cdot 10^{-2}(\Delta t = 0.25 \cdot 10^{-3})$. A zoom of the front wave on the left.

Let us first analyze the case of high strain rates, for which the process is dynamic at both scales (micro and macro). In Figure 6.2 we have plotted the comparison of the exact solution with the numerical results for $\dot{\Gamma} = 10^3, 10^4 \text{s}^{-1}$. We notice that for $\dot{\Gamma} = 10^4 \text{s}^{-1}$ the solution is very close to the exact one even for $h = 10^{-2}(\Delta t = 10^{-3})$. For $\dot{\Gamma} = 10^3 \text{s}^{-1}$ some small errors are present for $h = 10^{-2}, \Delta t = 10^{-3}$ which disappear for a smaller time step, beginning with $h = 0.5 \cdot 10^{-2}(\Delta t = 0.5 \cdot 10^{-3})$. If we formulate this conclusion in terms of microscopic evolution index M_Q we get that the associated non-dimensional number $\Delta t M_Q$ have to be less than 0.05 to get a very good numerical accuracy.

Let us see now the role played by the mesh size/time step for moderate strain rates. In figure 6.3 we have plotted the numerical results and the exact solution for $\dot{\Gamma} = 10^2 \text{s}^{-1}$. We see that the numerical solution does not approach the exact pulse for $h = 0.5 \cdot 10^{-2}(\Delta t = 0.5 \cdot 10^{-3})$ and for $h = 0.25 \cdot 10^{-2}(\Delta t = 0.25 \cdot 10^{-3})$ but starting with $h = 0.125 \cdot 10^{-2}(\Delta t = 0.125 \cdot 10^{-3})$ the difference between them is very small. We get that the non-dimensional number $\Delta t M_Q$ have to be less than 0.075 for a good convergence.

The numerical results and the exact solution for $\dot{\Gamma} = 10 \text{s}^{-1}$ are plotted in Figure 6.4. As we can see from Figure 6.1 the exact solution contains shocks and we are dealing with a quasi-static microscopic process associated to a dynamic macroscopic process. We notice that for $h = 0.125 \cdot 10^{-3}(\Delta t = 0.125 \cdot 10^{-4})$, which corresponds to $\Delta t M_Q = 0.075$, the

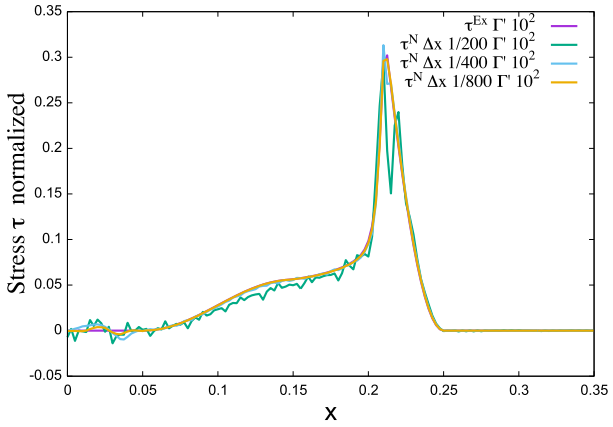

Figure 6.3: Micro-scale dynamic/quasi-static process ($\dot{\Gamma} = 10^2 \mathrm{s}^{-1}$): the spatial distribution of the exact stress $x \to \tau^{ex}(t,x)$ and of the computed stress $x \to \tau(t,x)$ with $h = 0.5 \cdot 10^{-2} (\Delta t = 0.5 \cdot 10^{-3})$, $h = 0.25 \cdot 10^{-2} (\Delta t = 0.25 \cdot 10^{-3})$ and $h = 0.125 \cdot 10^{-2} (\Delta t = 0.125 \cdot 10^{-3})$.

computed pulse has a good amplitude but the are a lot of spurious oscillations. We conclude that a mesh/time step refinement is not enough to get a accuracy and special shock capturing techniques have to be used.

Following the above analysis we conclude that the mesh size/time step have to be adapted to the strain rate. For dynamic microscopic processes the non-dimensional time step Δt has to be less that $0.05/M_Q$ which can be rewritten for the dimensional variables as

$$\delta t \leq 0.05 \frac{L_c^{micro}}{c_m}, \tag{6.28}$$

for a CFL=0.1.

6.5 Conclusions

We have introduced a new numerical scheme associated to the boundary value problem of the wave propagation in a material modeled by a general damage constitutive law. To solve the associated nonlinear hyperbolic problem we used an explicit leapfrog type scheme for the time discretization. This scheme deals with velocity and strain fields and not with stress fields, as it is usual in a velocity-stress formulation. Using this specific time discretization, during a (macro-scale) time step the constitutive damage law becomes a strain driven homogeneous problem (previous chapter). To capture the instabilities we used a semi-implicit Euler

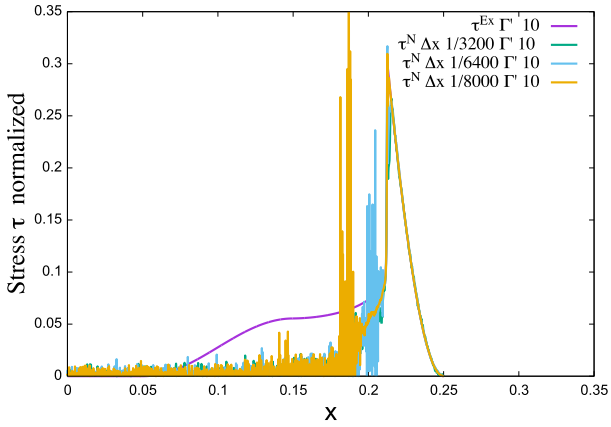

Figure 6.4: Micro-scale quasi-static process ($\dot{\Gamma} = 10\text{s}^{-1}$): the spatial distribution of the exact stress $x \to \tau^{ex}(t,x)$ and of the computed stress $x \to \tau(t,x)$ with $h = 0.3125 \cdot 10^{-3} (\Delta t = 0.3125 \cdot 10^{-4})$ $h = 0.15625 \cdot 10^{-3} (\Delta t = 0.15625 \cdot 10^{-4})$ and $h = 0.125 \cdot 10^{-3} (\Delta t = 0.125 \cdot 10^{-4})$.

method and a micro-scale time step to integrate the (micro-scale) strain driven problem. A DG method with a centered flux choice was considered for the spatial discretization.

To test the numerical scheme proposed in this chapter we construct a new (nontrivial) analytical solutions for a 1-D problem. Using a specific dimensionless variables we compared different exact solutions associated to different strain rates. Using the exact solution we analyzed the accuracy of the numerical scheme and its time step/mesh size sensitivity. We found that the dynamic processes (at the microscopic scale) are very well approximated by the numerical scheme. The centered scheme flux choice works well as far as the macro-scale solution is smooth. For quasi-static processes (at the microscopic scale), the solution exhibit shocks and a specific shock capturing flux choice has to be used.

CHAPTER 7

1-D WAVE PROPAGATION

The objective of this section is to study how the damage affects the one dimensional wave propagation of a stress pulse. For that we consider the dynamic evolution of an one-dimensional elastic body $\Omega = (0, L)$ (the generic space variable will be denoted by x) with a generic velocity $v = v(t, x)$, a generic strain $\gamma = \gamma(t, x)$ and a generic stress $\tau = \tau(t, x)$ (see Table 4.1 for the expressions of v, γ and τ in different configurations).

7.1 Problem statement

Let us write the system of equations for v, γ, τ and $l_i = l(\rho_i)$ modeling the one dimensional wave propagation problem with damage. The momentum balance law and the definition of the strain rate read

$$\rho^{mass}\dot{v}(t, x) = \partial_x \tau(t, x), \tag{7.1}$$

$$\dot{\gamma}(t, x) = \beta \partial_x v(t, x), \tag{7.2}$$

where $\beta = 1$ in mode I and $\beta = 1/2$ in modes II and III. For the effective elasticity law we have chosen the "non-interacting cracks method" (NIC) (see for instance Gambarotta and Lagomarsino [52] and Kachanov [69]) without any frictional or unilateral effects. The strain-stress equation (17.1) can be written as

$$\tau(t, x) = \frac{1}{A_0 + C \sum_{i=1}^{N} \rho(l_i(t, x))} \gamma(t, x), \tag{7.3}$$

where A_0, C are compliance coefficients (see table 4.1). For the damage evolution law we have chosen the criterion associated to the micro-cracks self similar growth under a far field stress (4.2) (the stress intensity factor K is given by (4.12) with a being a different non-dimensional number for each configuration as in table 4.1) and the associated evolution equation (3.5)

$$\dot{l}_i(t,x) = c_m \varphi_i\left(\left[\frac{a\sqrt{l_i(t,x)}\tau(t,x) - K_c}{(\alpha-1)K_c + a\sqrt{l_i(t,x)}\tau(t,x)} \right]_+ \right), \tag{7.4}$$

On the boundary $x = 0$ the structure is loaded by a stress pulse $S(t) = S^{max}\varphi_\delta(t-\delta)$, with $\varphi_\delta(s) = (\cos(s\pi/\delta)+1)/2$ if $|s| \le \delta$ and $\varphi_\delta(s) = 0$ if $|s| > \delta$ while at the other side $x = L$ the structure is fixed:

$$\tau(t,0) = S(t), \quad v(t,L) = 0. \tag{7.5}$$

At the initial state, the body is at rest, without any stress, and contains a distributed family of micro-cracks characterizing the homogeneous initial damage:

$$v(0,x) = 0, \quad \boldsymbol{\gamma}(0,x) = 0, \quad l_i(0,x) = l_i^0, \quad i = 1, ..., N. \tag{7.6}$$

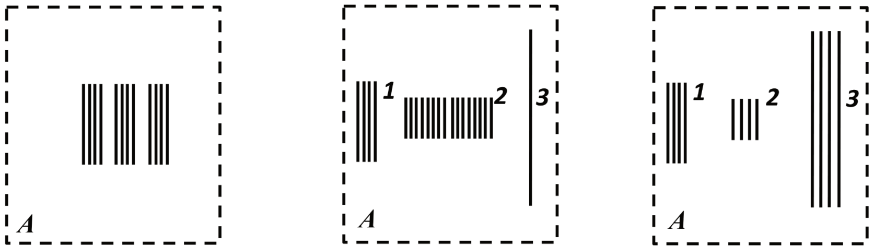

Figure 7.1: A schematic representation of the models used in the 1-D problem. Left: single crack damage model F1. Middle: 3 cracks model F3 (first case), Right: 3 cracks model F3' (second case).

If the loading pulse does not induce any supplementary damage (i.e. $l_i(t,x) = l_i^0$) then we can easily compute the propagation of the "undamaged" wave across the structure

$$\bar{v}(t,x) = \frac{\sqrt{\beta(A_0 + C\sum_{i=1}^N \rho(l_i^0))}}{\sqrt{\rho^{mass}}} S(t - x/c_0), \quad \bar{\tau}(t,x) = S(t-x/c_0),$$

where $c_0 = \sqrt{\beta}/\sqrt{\rho^{mass}(A_0 + C\sum_{i=1}^N \rho(l_i^0))}$ is the "undamaged" wave velocity.

Next we want to show how damage affects the profile and the propagation of a loading stress pulse. To do that we have considered the same values as in the previous subsection, corresponding to a anti-plane configuration in mode III, with $\rho^{mass} = 3673$ kg m^{-3}, while for the stress pulse S we have chosen $S^{max} = 200$MPa, $\delta = L/(10c_0)$. As before the initial half-length l_i^0 is taken small enough so that the material is almost undamaged at the initial state with a wave propagation speed $c_0 \approx \sqrt{\beta}/\sqrt{\rho^{mass} A_0}$. In all cases we consider below, the damaged stress pulse, after a transitory period of time near $x = 0$, propagates as a solitary wave (plotted as a snapshot of the stress-pulse taken at $t = 9\delta$).

First, we have considered a single family ($N = 1$) of micro-cracks (see Figure 7.1 left) and we have plotted in Figures 7.2 and 7.3, the stress pulse $\tau(t, x)$ versus the space x, computed at $t = 9\delta$. We remark that the damage induced by the loading wave significantly modifies the stress pulse shape (the amplitude is smaller and the pulse length is larger). The amplitude loss of the stress pulse is related to the softening of the strain-stress curve (see Figure 5.3) associated to damage and we expect a lower stress amplitude for the same strain. Since the elastic coefficients are affected, the wave velocity in the damaged material $c = \sqrt{\beta}/\sqrt{\rho^{mass}(A_0 + C\sum_{i=1}^{N}\rho(l_i))}$ (always localized behind the pulse front) is smaller than the velocity of the stress pulse front propagating in a fully undamaged zone. That means that the stress pulse needs more time and space to evacuate, and its length is larger than the undamaged pulse length.

7.2 Influence of the flaw density

To show the influence of the flaw density we have chosen the initial micro-cracks length to be $l^0 = 0.025$mm and we have performed computations for three different flaw densities $\eta = 10^6/2\pi, \eta = 10^6/\pi$ and $\eta = 0.25 \cdot 10^6/\pi$ m^{-2} and compared them with the undamaged case (see Figure 7.2). The stress pulse is more flat (larger length and smaller amplitude) when the flaw density increases. We also note that the damage pulse has the same shape as the undamaged pulse at the beginning, and the three cases are different only afterwards. This can be explained by the fact that the three cases have the same initial crack-length, hence the same activation stress. Only after that the flaw density η will play a role in the evolution of the stress pulse.

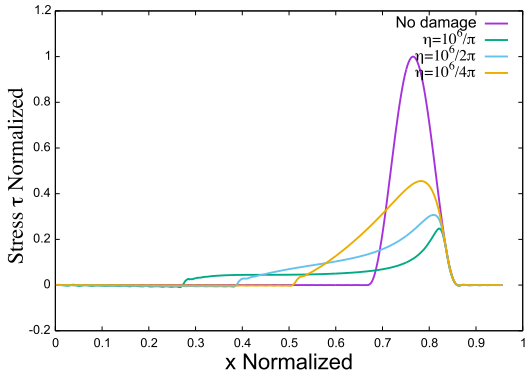

Figure 7.2: Influence of the flaw density in 1-D wave propagation. Normalized stress $\tau(t,x)/S^{max}$ versus normalized space x/L, computed at $t = 9\delta$ for model F1 (left in Figure 7.1): the undamaged material (red line) and different values of flaw densities $\eta = 10^6/2\pi$ (green), $\eta = 10^6/\pi$ (magenta) and $\eta = 0.25 \cdot 10^6/\pi$ m^{-2} (blue).

7.3 Influence of the initial crack length

We analyze now the influence of the initial crack length on the stress pulse. For that we have chosen the flaw density $\eta = 10^6/\pi \text{m}^{-2}$ and we have made computations (see Figure 7.3) for three different values of initial crack length $l^0 = 0.025$mm (green), $l^0 = 0.050$mm (magenta) and $l^0 = 0.0125$mm (blue) and for the undamaged material ($l^0 = 0$, red line). From the shape of the stress pulse at the forward tip, we see that for small initial crack lengths the damage is activated later than for larger ones, which leads to different pulse amplitude. The length of the pulse is less affected by the initial crack length.

7.4 Three families of micro-cracks

In a second numerical experiment we have considered models F3 and F3', that is, a family of three cracks ($N = 3$) with the initial lengths $l_1^0 = l^0 = 0.025$mm, $l_2^0 = l^0/2, l_3^0 = 2l^0$, and two different distributions of the flaw density. For the first one (model F3 plotted in Figure 7.1 middle) we take: $\eta_1 = \eta/3 = \frac{10^6}{6\pi}\text{m}^{-2}$, $\eta_2 = 4\eta/3, \eta_3 = \eta/12$ and $\rho_i^0 = \rho(l_i^0) = \rho^0/3$, hence the specimen has the same initial damage uniformly distributed at the three crack types. For the second case (model F3' Figure 7.1 right) we have chosen $\eta_1 = \eta_2 = \eta_3 = \eta/3 = \frac{10^6}{6\pi}\text{m}^{-2}$, i.e. the three different cracks are uniformly distributed. In Figure 7.4 we have compared

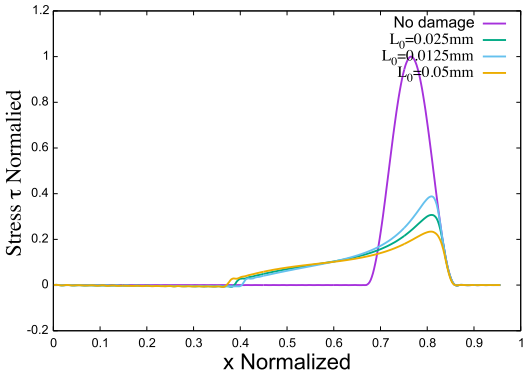

Figure 7.3: Influence of the initial crack length in 1-D wave propagation. Normalized stress $\tau(t,x)/S^{max}$ versus normalized space x/L, computed at $t = 9\delta$ for model F1 (left in Figure 7.1): undamaged material (red line) and different values of initial crack lengths $l^0 = 0.025$mm (green), $l^0 = 0.050$mm (magenta) and $l^0 = 0.0125$mm (blue).

the three damage models F1,F3,F3' represented in Figure 7.1. The stress pulse of model F1 (green) and F3' (magenta) are very close, but model F3 (blue) is very different. This confirms the fact, already observed for model F1, that the flaw density has a much stronger influence than the initial crack length.

7.5 Conclusions

We analyzed how the damage affect the one dimensional wave propagation of a stress pulse. We found that the stress pulse is more flat (larger length an smaller amplitude) when the flaw density increases. Concerning the influence of the initial crack length on the stress pulse we found that for small initial crack lengths the damage is activated later than for larger ones, which leads to different pulse amplitude. The length of the pulse is less affected by the initial crack length.

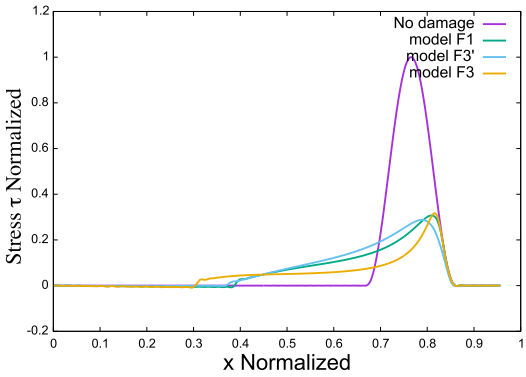

Figure 7.4: 1-D problem for 3 families of micro-cracks: normalized stress $\tau(t,x)/S^{max}$ versus normalized space x/L computed at $t = 9\delta$. Red: undamaged model, green: model F1 (left in Figure 7.1), blue: model F3 (middle in Figure 7.1), magenta: model F3' (right in Figure 7.1).

CHAPTER 8

ANTI-PLANE WAVE PROPAGATION

Consider the anti-plane shearing in a domain $\mathcal{D} = \Omega \times \mathbb{R}$, with $\Omega \subset \mathbb{R}^2$ not necessarily bounded. We suppose that the displacement field $\boldsymbol{u} = (u_x, u_y, u_z)$ is 0 in directions Ox and Oy and that u_z does not depend on z. The displacement is therefore denoted simply by $w = w(t, x, y)$ and the velocity by $v = \dot{w}$. The non-vanishing deformations are $\gamma_x = \epsilon_{xz} = \frac{1}{2}\partial_x w$ and $\gamma_y = \epsilon_{yz} = \frac{1}{2}\partial_y w$ (i.e. $\boldsymbol{\gamma} = \frac{1}{2}\nabla w$), while the non-vanishing shear stress components are $\tau_x = \sigma_{xz}$, $\tau_y = \sigma_{yz}$, which can also be represented through the vector $\boldsymbol{\tau} = (\tau_x, \tau_y)$.

The effective elasticity model, the damage model and the material settings used in this chapter are the same as in Chapter 7 .

8.1 Anisotropic damage under isotropic loading

The numerical experiment considered in this subsection investigates the influence of the damage anisotropy on the propagation of an initial isotropic loading. We considered the elastic body $\Omega = \{(x, y)\ ;\ x^2 + y^2 < R^2\}$, the disc of rayon R, impacted in the center with an initial velocity $v_0(x, y) = V_0\varphi_\delta(\sqrt{x^2 + y^2})$ ($\delta = R/5$).

We have considered three models of the initial distributions of three the mini-cracks families ($N = 3$) of normal vectors $\boldsymbol{n}_i = (\cos(\theta_i), \sin(\theta_i))$ for $i = 1, 2, 3$. The first one, called "model a", is the same as model F3 in the one-dimensional problem (see also Figure 7.1 middle), i.e. $\theta_i = 0$, $l_1^0 = l^0 = 0.025$mm, $l_2^0 = l^0/2, l_3^0 = 2l^0$ and $\eta_1 = \eta/3 = \frac{10^6}{6\pi}\mathrm{m}^{-2}$, $\eta_2 = 4\eta/3, \eta_3 = \eta/12$.

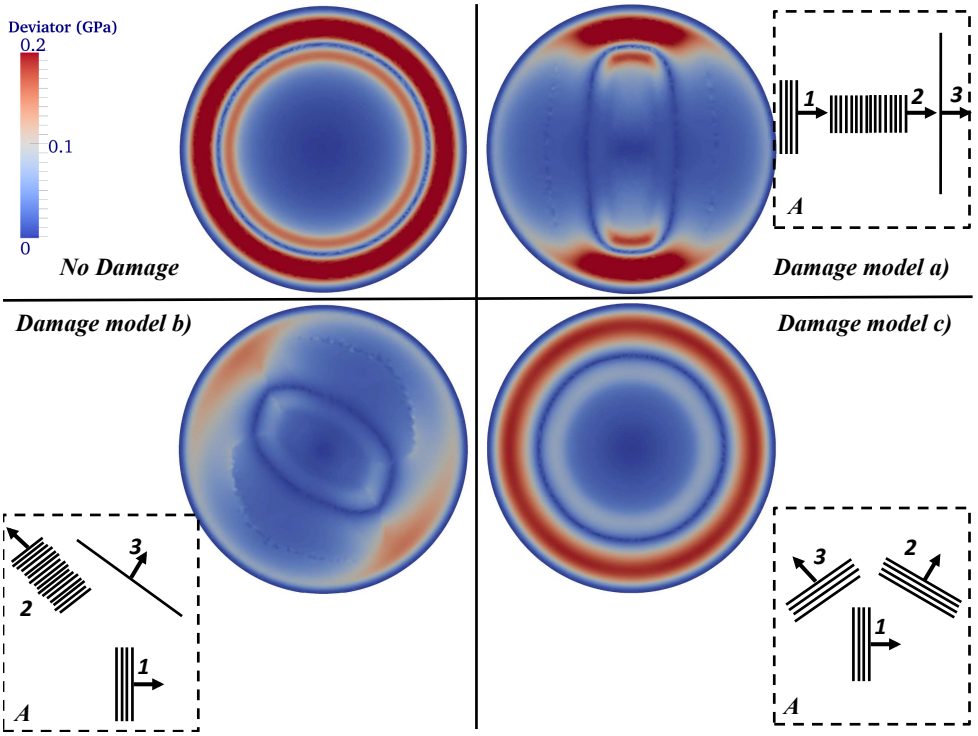

Figure 8.1: The distribution of stress deviator at the final time $t = T$. Up left : no-damage model. Up right: damage model a). Button left: damage model b). Button right: damage model c).

The second one, called "model b", has the same initial lengths l_i^0 and flaw densities η_i, but the orientations are different for each family : $\theta_1 = 0, \theta_2 = \pi/3, \theta_3 = 2\pi/3$. The last one, called "model c", has the same orientations as in the previous case but with uniform initial lengths $l_i^0 = l^0$ and flaw densities $\eta_i = \eta/3$. We have made numerical computations over the time interval $[0, T]$ with $T = (R - \delta)/c_0$.

In Figure 8.1 we have plotted the spatial distribution of the stress deviator $\sqrt{\tau_x^2 + \tau_y^2}$ at the final time $t = T$ for different damage models. The the undamaged model (up left) exhibits perfect isotropy and its the stress deviator is concentrated in a circular ring. For damage model (up right in Figure 8.1) the final distribution is very different. In the direction of the micro-cracks the initial circular wave damages the material, which affects the speed wave, hence the wave is propagating much slower than in the orthogonal direction, where the material is hardly damaged. As we can see from Figure 8.2 (top) all the three systems are activated but, as expected, systems 1 and 3 are more developed than the system 2. Once

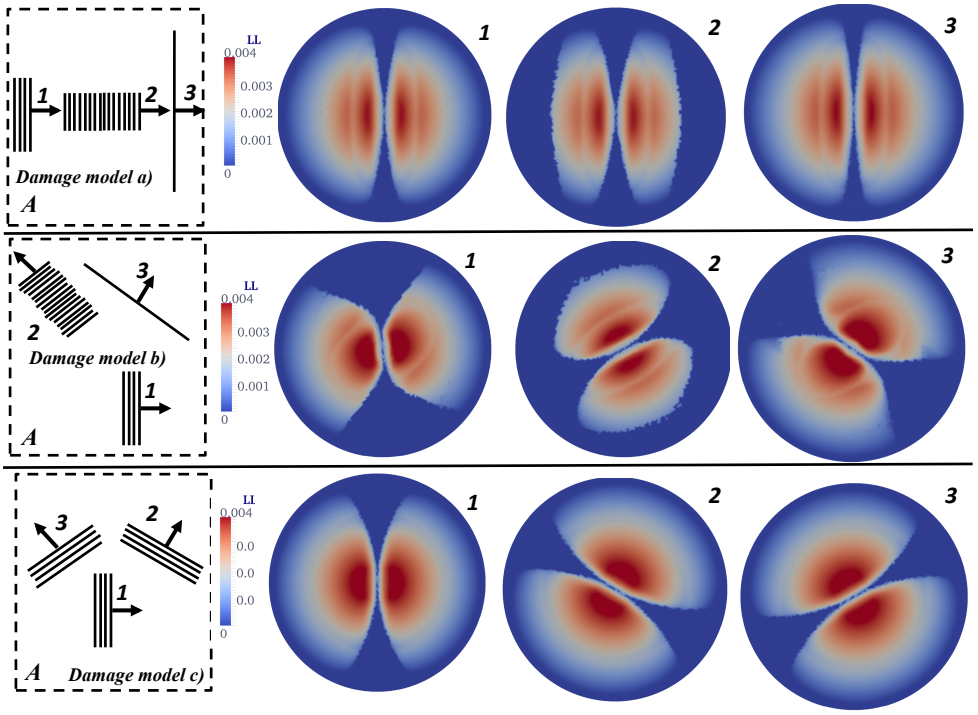

Figure 8.2: The distribution of the micro-cracks length $l_i(t)$ at the final time $t = T$. Up: damage model a). Middle: damage model b). Button: damage model c).

again we do not note any significant difference between the three final micro-cracks lengths.

In Figure 8.1 (bottom left) we have depicted model b). We remark that even if the three cracks systems have different orientations, the final snapshot still shows an important anisotropy. This is due to the differences of initial micro-cracks lengths and flaw densities for the three directions. We note that damage is weaker in the direction of the largest micro-cracks which also have the lowest flaw density. This small flaw density is not compensated by the crack lengths. Indeed, in Figure 8.2 (middle) we see that all 3 directions are activated and, even if the initial crack lengths are different ,the final lengths are very similar.

Finally, the damage model c) is plotted in Figure 8.1 (bottom right). We note that the final distribution of the stress deviator shows a very good damage isotropy. Hence, at least for isotropic loadings, the choice of only three directions with the same initial properties, ensures an isotropic damage behavior. This is confirmed by the symmetric distribution of the final crack lengths plotted in Figure 8.2 (bottom).

8.2 Anisotropic loading of an initial isotropic damaged material

We want to illustrate here the influence of an anisotropic loading on an initially isotropic (damaged) material. In order to do so, we consider a domain $\Omega = (0, 2a) \times (0, a) \cup A \setminus D$ where A is the half disk of radius $R = a/2$ centered at $(2a, a/2)$ and D is the disk of radius $R = a/6$ entered at $(2a, a/2)$ (see Figure 8.3). At initial time the elastic body is at rest without any pre-stress conditions. We impose in $x = 0$ a stress pulse $\boldsymbol{\sigma n} = B\varphi(t - \delta)\boldsymbol{e}_z$ of duration 2δ (with $\delta = a/8c_S$) while the other boundaries are stress free. We want to see how this loading wave will damage the material and will change its wave propagation properties. As before we have considered the material settings: Young modulus $E = 300$GPa, Poisson ratio $\nu = 0.24$ and $\rho^{mass} = 3673\text{kg/m}^3$. As we can see from the previous subsection the "isotropic" damage behavior could be obtained with an uniform spatial distribution in three directions orientated at $2\pi/3$. That is why we have considered an uniform initial micro-crack lengths $l_i^0 = 0.025$mm, with the same flaw density $\eta_i = \frac{10^6}{6\pi}\text{m}^{-2}$ and having the orientations of the normals at $\theta = 0, \theta_2 = 2\pi/3$ and $\theta_3 = 4\pi/3$. We have done numerical computations over the interval $[0, T]$ with $T = 2a/c_S$.

The main scenario of this numerical experiment has three time periods. In the first time interval the loading wave will travel as a plane wave in the material in the Ox direction and will generate a damage increase principally in the direction $\theta = 0$ and less in the other two directions. When reaching the circular hole the wave will be reflected as a cylindrical wave (isotropic loading) in the domain which was non-isotropically damaged by the incident wave. We expect to see in the third time interval that in $\theta = 0$ direction the reflected wave will be slower than in the other directions.

To see how the stress pulse is affected by the presence of micro-cracks we have plotted in Figure 8.3 four snapshots ($t = 0.6T, 0.7T, 0.8T$ and the final time $t = T$) of the spatial distribution of the stress deviator $\sqrt{\tau_x^2 + \tau_y^2}$ for the model with damage (top) and without damage (bottom). In Figure 8.4 we plotted the distribution of the micro-cracks length $l_i(t)$ at the same time t for the three families of micro-cracks (up $\theta = 0$, middle $\theta = 2\pi/3$ and bottom $\theta = 4\pi/3$).

At the first snapshot (Figure 8.3 left up and Figure 8.4 left), associated to the first time interval of our scenario, we remark that the wave associated to the loading pulse at the left side traveled as a plane wave in both models. As we have already noticed in the one

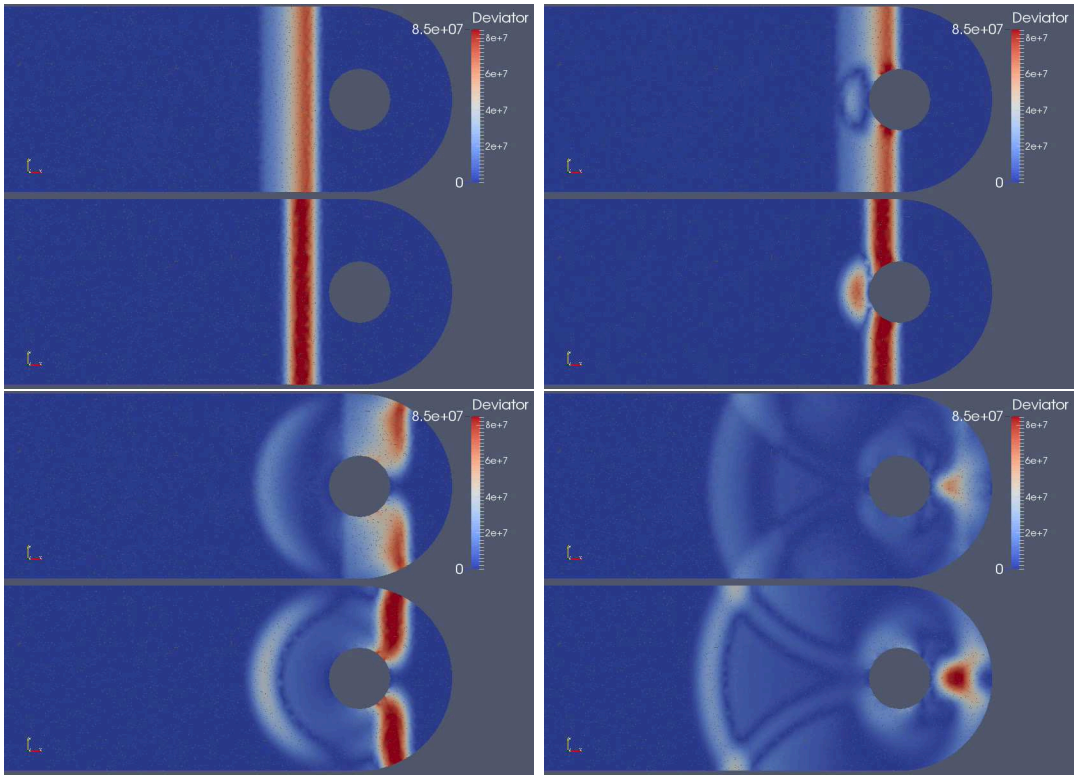

Figure 8.3: Snapshots of the spatial distribution of the stress deviator at $t = 0.6T, 0.7T, 0.8T$ and the final time $t = T$. The model with damage on the top of the model without damage.

dimensional simulations, the damaged wave has a smaller amplitude and a longer wave length but the two pulses have the same front wave. The first family, $\theta = 0$, is the single family of micro-cracks which was affected by the loading wave. That means that after the passage of the plane wave the material has a weakness in the Ox direction and loses its isotropy.

The second time interval of our scenario (the reflection on the circular cavity) is illustrated in the second snapshot (see Figure 8.3 top and right and Figure 8.4 middle left). We see that, since the damaged pulse is larger, it can include the reflected wave, while for the non-damage model the direct and reflected pulses are separated. The damage for the first family continue to increase and we notice the first evolution of the damage in the second and third directions. Essentially, they are due to the reflection on the circular cavity and we remark the localization of the damaged zones are not the same for the second and third family of micro-cracks.

In the third snapshot (see Figure 8.3 bottom left and Figure 8.4 middle right) we see the propagation of the direct wave behind the circular cavity and the propagation of the reflected

wave in the left part of the domain. We see that the front of the direct wave arrives in the same time in both cases (damaged and undamaged) but for the reflected wave the arrival times are different. Indeed in the Ox direction, corresponding to the maximal damaged direction, the damaged front wave has a delay with respect the undamaged one, while in Oy direction front waves are simultaneous. This can be confirmed for the analysis of the damage distribution : The first family has a lot of damaged accumulated at the left of the circular cavity while the the second and the third family are not affected by the damage.

Finally, in the fourth snapshot we see that the delay of the damaged reflected wave front is larger and other two reflections are involved. In conclusion we have seen that even if at the beginning we deal with an isotropic damaged material, after the propagation of a (loading) anisotropic wave the material has an anisotropic behavior.

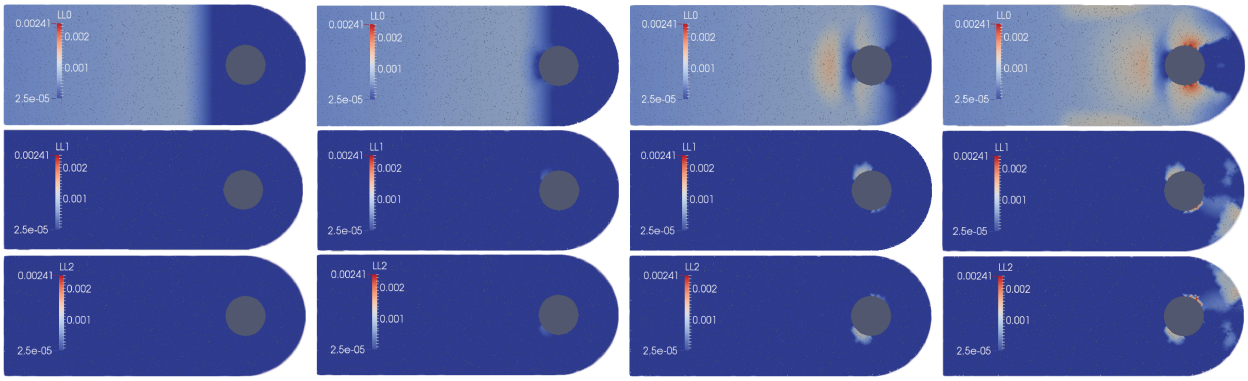

Figure 8.4: The distribution of the micro-cracks length $l_i(t)$ at $t = 0.6T, 0.7T, 0.8T$ and the final time $t = T$. Up: family $i = 1, \theta = 0$. Middle: family $i = 2, \theta = 2\pi/3$. Bottom: family $i = 3, \theta = 4\pi/3$.

8.3 Conclusions

We have done some numerical experiments in the anti-plane configuration to investigate the influence of the damage anisotropy on the propagation of an initial isotropic loading. For that we have analyzed three different damage scenarios, for a different choice of the initial micro-cracks' families. We found that in the direction of the micro-cracks the material is hardly damaged and the initial circular wave is propagating much slower than in the orthogonal direction. Even if the cracks systems have different orientations, the final snapshot still

shows an important anisotropy. This is due to the differences of initial micro-cracks lengths and flaw densities. If the initial micro-cracks lengths and flaw densities are the same in three directions the final distribution of the stress deviator shows a very good damage isotropy. Hence, at least for isotropic loadings, the choice of only three directions with the same initial properties, ensures an isotropic damage behavior.

Concerning the anisotropic loading of an initial isotropic damaged material we found that even if at the beginning we deal with an isotropic damaged material, after the propagation of a (loading) anisotropic wave the material has an anisotropic behavior.

CHAPTER 9

BLAST IMPACT AND DAMAGE EVOLUTION

The aim of this chapter is to illustrate how the numerical method associated to the damage model works in modeling the blast wave propagation.

We consider, as for the cracked materials, an elastic domain $\Omega = (0, a) \times (0, 5a)$ in a stress plane configuration (see Figure 9.1), which is impacted at the left side $x = 0, y \in (2a, 3a)$ by a compressive pulse $t \to S(t)$ with an amplitude $-B$ and a time duration $2\delta = 0.5a/c_P$. The faces $y = 0$ and $y = 5a$ are fixed and the face $x = a$ is stress free. The loading compressive wave is traveling into the damage material till it reaches the stress free boundary, when it will be reflected as traction loading wave. In addition to this direct and reflected P-wave we have also a S-wave generated at the boundary between the loaded surface and the unloaded one $(x = 0, y = 2a, 3a)$.

We have done numerical computations over the interval $[0, T]$ with $T = 2a/c_P$ using the damage model defined by a NIC effective elasticity (17.1) associated to micro-cracks having normals orientated with an angle θ.

As before, we have considered the material settings: Young modulus $E = 300GPa$, Poisson ratio $\nu = 0.24$ and $\rho^{mass} = 3673\text{kg/m}^3$with an uniform initial micro-crack lengths $l_i^0 = 0.025\text{mm}$, with the same flaw density $\eta_i = \frac{10^6}{3} m^{-2}$, corresponding to the initial crack density parameter $\rho_0 = 10^{-5}$, and having the orientations at $\theta_i, i = 1, .., N$. Concerning the damage model we have used the self similar micro-crack under a stress far field model, associated to a mixed mode (I and II) fracture criterion (18.2) with $K^I = K^{II} = 2.7\ \text{MPa}\sqrt{\text{m}}$. For the damage evolution law we have used the universal crack speed function of Deng and

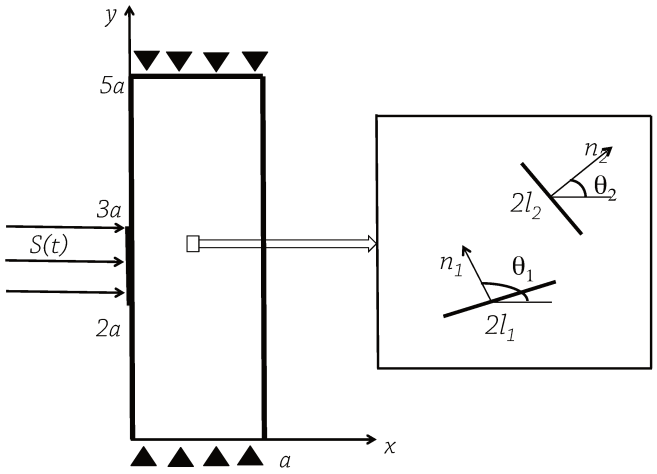

Figure 9.1: Schematic representation of the blast impact on a solid modeled with a local damage constitutive law.

Nemat-Nasser [32] given by (18.5). The reference strain rate was chosen to be $\dot{\Gamma} = 10^4 \mathrm{s}^{-1}$ and we have considered $a = 2c_P\gamma^f/\dot{\Gamma}$ where $\gamma^f = 0.003$ is the final strain. The amplitude B was taken $B = G_0\gamma^f$ and we have done numerical computations over the interval $[0, T]$ with $T = 2a/c_P$.

9.1 Single family of micro-cracks

Let us consider here the case of one family of micro-cracks ($N = 1$) having the orientation of the normal to be θ. We start with the frictionless model and we continue by introducing the friction into the damage computations. Firstly we will consider two configurations without friction: horizontally and vertically oriented micro-cracks.

In Figure 9.2 we have plotted the comparison between the propagation of the blast wave computed for the damage model (middle) and the stress deviator computed for the model without damage (right) for vertical cracks ($\theta = 0$). In the first frame, at $t = 0.5T$, we have plotted the instance before the pulse reaches the boundary. There are almost no difference between the damaged and the undamaged case. We notice that only the S-waves, generated at the end of the loading region, have produced some damage. That means that the vertical cracks have worked in mode II. In the second frame, at $t = 0.75T$ we have plotted the instance

just after the pulse has been reflected on the stress free boundary. The damage produced by the S-waves (in mode II) have increased but the damage related to the reflected tractional wave (mode I) is not yet present. Indeed, between $t = 0.6T$ and $t = 0.75T$ the micro-cracks do not have the time to growth. In the third frame, at $t = 0.875T$ we see that the damage produced by the S-waves (in mode II) have continued to increase and we note the presence of the damage related to the reflected tractional wave (mode I). This phenomenon is visible in the final frame and we remark a difference between the damaged and undamaged model distributions of the reflected pulse. At the end of the time interval the maximal value of damage was ρ^{max}=0.2. In conclusion for this period of time, we see that the mode II, present from the first instants of the loading wave, have been more active (created more damage) than the reflected pulse.

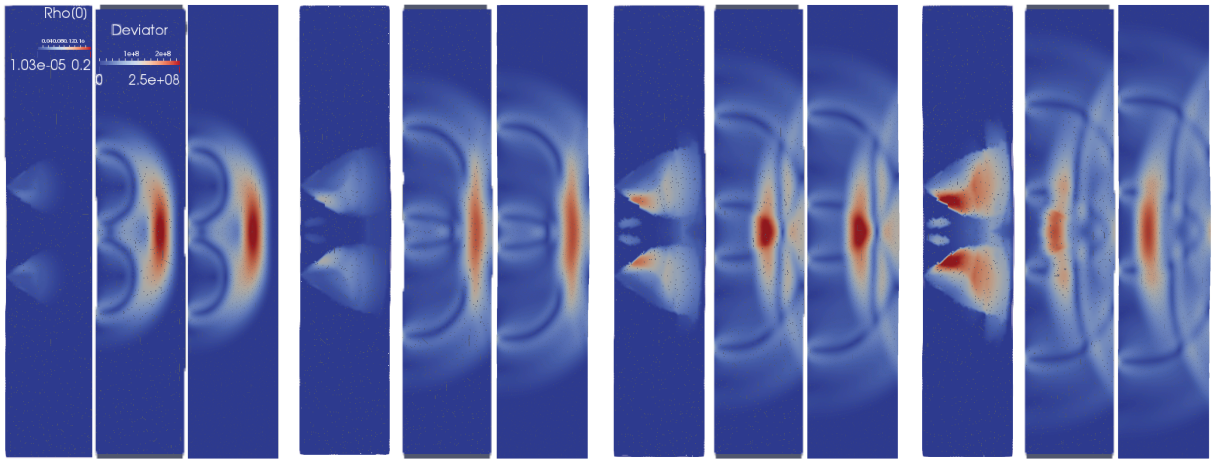

Figure 9.2: Vertical micro-cracks ($\theta = 0$) without friction. Four snapshots at $t = 0.5T, 0.75T, 0.875T$ and $t = T$ of the propagation of the blast wave. At each time t in color scale the distribution of: the crack density $\rho(t)$ (left), the stress deviator (in Pa) computed for the model with damage (middle) and for the model without damage (right).

In Figure 9.3 we have plotted the comparison between the propagation of the blast wave computed for the damage model (middle) and the stress deviator computed for the model without damage (right) for horizontal micro-cracks ($\theta = \pi/2$). In all the frames we note that the damage produced by the S-wave is more important than in the case of the vertical cracks. Moreover, the distribution of the damage seems to be different and the zones maximal damage are not the same. The are no damage produced by the reflected tractional wave. In the last frame, at the end of the time interval ($t = T$) the maximal value of damage

was ρ^{max}=0.237, higher than for the vertical cracks configuration but he conclusions are the same. Indeed, here only mode II is present and the reflected tractional pulse have not produced any damage.

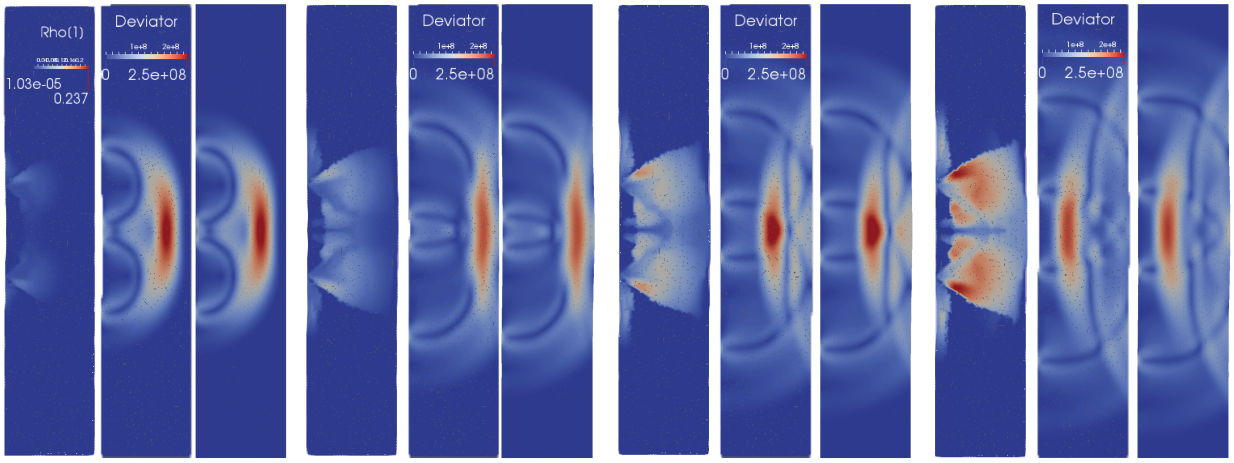

Figure 9.3: Horizontal micro-cracks ($\theta = \pi/2$) without friction. Four snapshots at $t = 0.5T, 0.75T, 0.875T$ and $t = T$ of the propagation of the blast wave. At each time t in color scale the distribution of: the crack density $\rho(t)$ (left), the stress deviator (in Pa) computed for the model with damage (middle) and for the model without damage (right).

In the next computation we want to illustrate how the frictional damage model works. To have a more important effect due to friction we have considered that the cracks are oriented at $\theta = -\pi/4$. In this case the compressive wave will generate a frictional resistance, while the traction reflected wave will not do it. In Figure 9.4 we have plotted the propagation of the blast wave for the model with friction ($\mu = 0.5$). We remark that in the upper part of the sample, where the S-waves generate a negative shear stress σ_{xy} the cracks with the orientation $\theta = -\pi/4$ are loaded in traction producing a lot of damage. In contrast in the lower part, where we deal with positive shear stress σ_{xy} the cracks are loaded in compression and the the damage associated to the S-wave is not anymore present. As we can see in the last snapshot the reflected wave is not anymore symmetric with respect to the horizontal axis. This non-symmetry is a consequence of the non-symmetric damage generated by the loading direct wave.

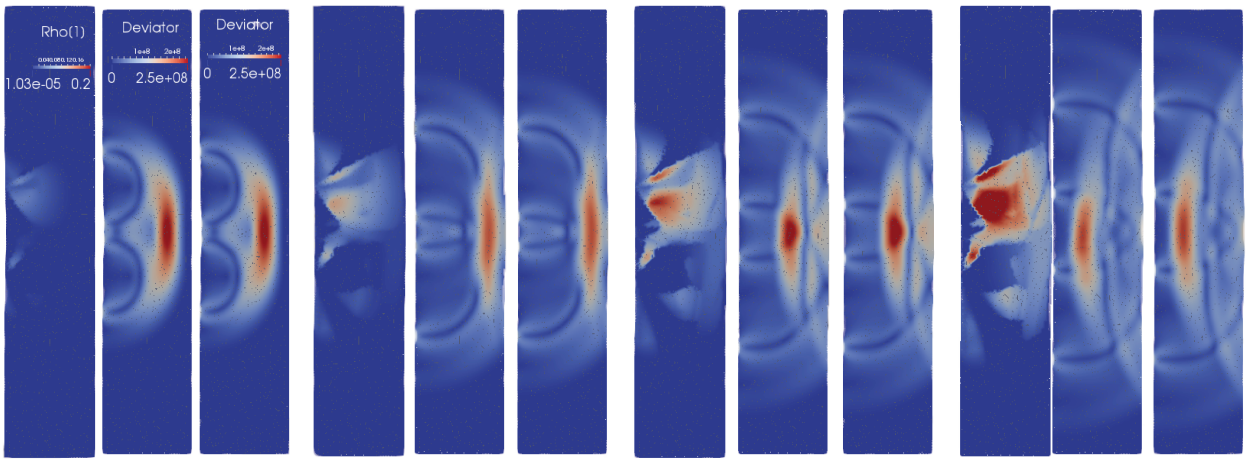

Figure 9.4: Micro-cracks at $\theta = -\pi/4$ with friction. Four snapshots at $t = 0.5T$, $0.75T$, $0.875T$ and $t = T$ of the propagation of the blast wave. At each time t in color scale the distribution of: the crack density $\rho(t)$ (left), the stress deviator (in Pa) computed for the model with damage (middle) and for the model without damage (right).

9.2 Four families of micro-cracks

In this section we consider the case of four families of micro-cracks orientated at $\theta_1 = 0, \theta_2 = \pi/2, \theta_3 = \pi/4$ and $\theta_4 = -\pi/4$, which corresponds to an initial isotropic damage distribution. To see the role played by the friction in the damaged material we will compare the computations obtained with and without friction.

In Figure 9.5 we have plotted the stress deviator evolution for frictionless, frictional and undamaged model. In the first frame, we do not distinguish differences in the three cases. In the following two frames, at $t = 0.75T$ and $t = 0.875T$, we observe a loss in the amplitude of the stress deviator for both frictional and frictionless case, being more notorious in the frictionless case. In the last frame, at $t = T$, we observe a remarkable loss of amplitude of the stress deviator for the frictionless case. Since the material is damaged the waves travel with a lower velocity and we remark a delay between the arrival time of the wave with and without damage. We conclude that the friction in the damage model has a non-negligible influence on the amplitude and on the speed of the loading wave.

To see the role played by the friction on the damage fields we have plotted in Figure 9.6 the final crack density ρ_i for each micro-crack family. First, we note that each damage pattern has the same shape as in the case of one family of micro-cracks (see the final patterns of damage in Figures 9.2, 9.3 and 9.4). That means that we deal with an additive effect of

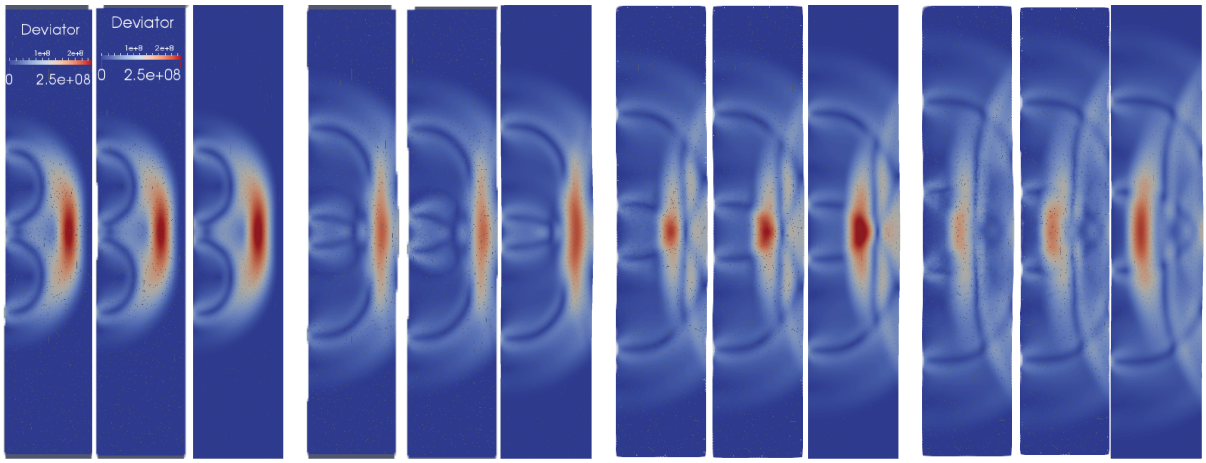

Figure 9.5: Four families of micro-cracks without (left) and with friction (middle) and no damage (left). The propagation of the blast wave with the stress deviator (measured in Pa) in the color scale. Four snapshots at $t = 0.5T, 0.75T, 0.875T$ and $t = T$.

the damage without an important interplay between the micro-cracks families. We see also that the damage in the frictionless case is much more developed than for the frictional case. Indeed, the friction force reduces the tangential stress acting on the micro-cracks and as a consequence the crack-growth is reduced (or absent) in mode II. This fact is more visible for the cracks orientated at $\theta = \pm\pi/4$ and at $\theta = \pi/2$.

9.3 Conclusions

We have analyzed the role played by the initial distribution of the micro-cracks in the blast wave propagation. We found that the behavior is different if the micro-cracks are vertically or horizontally oriented. For micro-cracks orientated at $\pi/4$ the reflected wave is not anymore symmetric with respect to the horizontal axis. This non-symmetry is a consequence of the non-symmetric damage generated by the loading direct wave. The friction in the damage model has a non-negligible influence on the amplitude and on the speed of the loading wave. If several orientations of the micro-cracks are considered we deal with an additive effect of the damage without an important interplay between the micro-cracks families. We found also that the damage in the frictionless case is much more developed than for the frictional case.

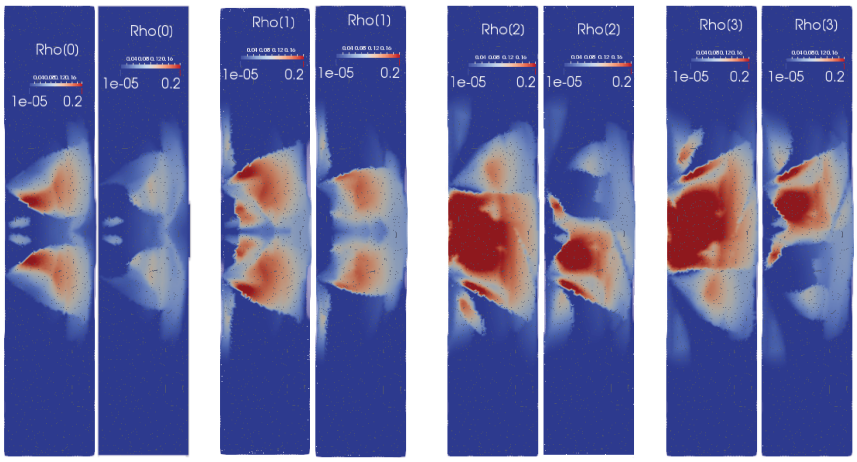

Figure 9.6: Four families of micro-cracks without (left) and with friction (right). Final ($t = T$) crack density ρ_i (damage) for each micro-crack family: left $\theta_1 = 0$, middle left $\theta_2 = \pi/2$, middle right $\theta_3 = \pi/4$ and right $\theta_4 = -\pi/4$.

CHAPTER 10

FINAL CONCLUSIONS AND PERSPECTIVES

In this part we analyzed the coupling between the damage evolution and the wave propagation. Since the loading wave, propagating into the material, produces damage and changes the propagation properties of the material, the mechanical damage processes cannot be separated from the wave propagation process. The micro-crack growth is activated in some privileged directions according to the applied macroscopic loading leading to a anisotropic behavior.

The (local) damage model for brittle materials used in this part is rather general and covers a wide spectrum of the micro-mechanics-based damage models.

We obtained stability criteria for dynamic and quasi-static processes at the microscopic scale. We found that for a given continuous strain history the quasi-static or dynamic problems are unstable or ill-posed (multiplicity of material responses) and whatever the selection rule is adopted, shocks (time discontinuities) will occur. The dynamic stability criterion coincides with the quasi-static one for weak inter-families interactions or for a single active family of micro-cracks. We found a critical crack density parameter and a critical micro-crack radius (length) which distinguish between stable and unstable behaviors of some specific models (NIC effective elasticity and self similar growth) associated to some special configurations (one family of micro-cracks in mode I, II and III and in plane strain or plain stress).

For homogeneous strain-driven processes we found that for a single family of micro-cracks the rate of deformation plays a major role. For intermediate and low rates of deformation,

sharp stress drops related to the material instabilities could be expected, and the strain-stress curve is not sensitive on the strain rate. On the contrary, for high rates of deformation, the strain-stress curve depends strongly on the rate of deformation but only a smooth stress drop is expected. The role played by the rate of deformation is much more complex if more families of micro-cracks are considered.

We have introduced a new numerical scheme associated to the boundary value problem of the wave propagation. To solve the associated nonlinear hyperbolic problem we used an explicit leapfrog type scheme for the time discretization. This scheme deals with velocity and strain fields and not with stress fields, as it is usual in a velocity-stress formulation. To capture the instabilities we used a semi-implicit Euler method and a micro-scale time step to integrate the (micro-scale) strain driven problem. A DG method with a centered flux choice was considered for the spatial discretization. To test the numerical scheme proposed in this chapter we construct a new (nontrivial) analytical solutions for an 1-D problem. Using the exact solution we analyzed the accuracy of the numerical scheme and its time step/mesh size sensitivity. We found that the dynamic processes (at the microscopic scale) are very well approximated by the numerical scheme. The centered scheme flux choice works well as far as the macro-scale solution is smooth. For quasi-static processes (at the microscopic scale), the solution exhibit shocks and a specific shock capturing flux choice have to be used.

We analyzed how the damage affect the one dimensional wave propagation of a stress pulse. We founded that the stress pulse is more flat (larger length an smaller amplitude) when the flaw density increases while the length of the pulse is less affected by the initial crack length.

In the anti-plane configuration in the direction of the micro-cracks the material is hardly damaged and the initial circular wave is propagating much slower than in the orthogonal direction. Even if the cracks systems have different orientations, the final snapshot still shows an important anisotropy. This is due to the differences of initial micro-cracks lengths and flaw densities. For isotropic loadings, the choice of only three directions with the same initial properties, ensures an isotropic damage behavior. We illustrated the fact that even if at the beginning we deal with an isotropic damaged material, after the propagation of a (loading) anisotropic wave the material has an anisotropic behavior.

We have analyzed the role played by the initial distribution of the micro-cracks in the blast wave propagation. We found that the behavior depends on the micro-cracks orientation. The friction in the damage model has a non-negligible influence on the amplitude and on

the speed of the loading wave. If several orientations of the micro-cracks are considered an additive effect of the damage is present without an important interplay between the micro-cracks families.

For the future prospects related to the wave propagation in a solid with a micro-mechanics based damage model we want to mention that a deeper analysis of the inter-families interaction (especially for the interaction of micro-cracks with different orientations) in connection with the dynamic material stability or wave propagation is needed. In this thesis we have given some examples one dimensional or two dimensional problems to point out that this interaction exists but we have not explored this subject in detail. Another future prospect is to include some shock capturing techniques (numerical fluxes, slope limiters, ...) or other smoothing methods (Suliciu's or viscous or gradient regularizations) in the numerical scheme. This is in important point in modeling wave propagation at low and moderate strain rates in damaged materials which exhibit material instabilities. Indeed, in this thesis only the material and temporal instabilities were well captured, while the spatiotemporal discontinuities associated to the induced wave propagation have to be addressed in a future work. Finally, in the numerical and mechanical approach the flaw densities, the micro-cracks' radius and orientations have to be introduced as random variables (as in Graham-Brady [53] and Huq et al. [65] for instance), and not as deterministic characteristics of the material. It will be of high interest to address a stability analysis in connection with a deterministic approach. Can the present instability capturing numerical approach be adapted to random materials variables, and how to take advantage of a DG discretization for a probabilistic analysis, are two questions to be addressed also.

Part II

Wave propagation in a cracked solid

CHAPTER 11

INTRODUCTION

11.1 Introduction

The derivation of accurate relationships between the micro-structure (pores, micro-cracks) and overall elastic properties of brittle materials (rocks, ceramics,..) is an ongoing problem in material science, geophysics, and solid mechanics. Micro-fractures strongly influence the (seismic) wave propagation giving rise to scattering and fracture-induced anisotropy. In a fractured medium, when the size of fractures is substantially less than the wavelength, wave propagation can be described using effective-medium theories (see for instance [84, 64, 108, 115] or [109] and references therein).

There is a general agreement for a dilute concentration of micro-cracks among these models, but for higher concentrations considerable differences arise. Moreover, spatial correlations between different fractures cannot be included in equivalent-medium models. Therefore, it is necessary to validate effective-medium theories with experimental data [23, 64] or numerical simulation [106, 105] .

The large majority of numerical schemes that treat the wave propagation in materials with micro-fractures are using the finite-difference method. Some of them take the cracks as secondary point sources [121] and others use penny-shaped weak inclusions [106, 105] to model the micro-cracks. In order to adequately model the thickness of cracks, the finite-difference discretization has to be done on a small grid spacing which generates high computational cost (both the grid spacing and time interval have to be small to satisfy stability considerations).

Also, when the medium contains high-contrast discontinuities (strong heterogeneities), some instability problems arise on a staggered grids [122] may appear. Some of them could be avoided by using the rotated staggered grid technique [104].

In contrast, for the "explicit interface" approaches the fracture is assumed to have a vanishing width across which tractions are continuous, but displacements and velocities are allowed to have jumps. One of the "explicit interface" approaches is the so called "linear-slip displacement-discontinuity model" [107, 108, 123, 129] offering a unified description of fractures on scales both large and small, relative to the wavelength. However, this model is linear and cannot describe the nonlinear phenomena present on the micro-cracks interface as unilateral contact and/or friction.

To model frictional contact constraints, the classical finite-element technique makes use of three (nodal values) discretization methods: the Lagrange multiplier method, the penalty method and the augmented Lagrangian method (see for instance [6, 110, 99, 128, 85, 42] or [125]). Other discretization schemes, as mortar methods, were developed for non-matching grid [15, 16, 76, 113]. Another class of mixed formulations are the "dual mortar" methods (see for instance [100, 111]). An alternative to mixed methods is the primal formulation (in which the displacement field is the only unknown) by using Nitsche's method (see [83, 126] and its extensions to either quasi-static friction [3, 119] or explicit dynamics [2]).

Nitsche's method has also been used under the guise of the "interior penalty" method within the context of discontinuous Galerkin (DG) methods (see Arnold [4] for the earliest applications). There are a lot of important developments of discontinuous Galerkin approaches for linear and nonlinear solid mechanics (see for instance [57] in linear elasticity, [79, 114, 117] in finite-strain elasticity, [93] in elasto-plasticity and [91] in second-order computational homogenization). A unifying analysis of the DG method applied to elliptic problems is contained in [6]. A second group of important interface problems in solid mechanics involves contact problems with friction. Very recently, Truster and Masud [120] have developed a stabilized discontinuous Galerkin (DG) interface method for transient contact with Coulomb friction extending their previous work on interphase damage modeling [118].

The aim of this part of the thesis is to use the discontinuous Galerkin (DG) method to investigate the dynamics of (damaged) materials with a nonlinear micro-structure (micro-cracks in frictional contact). In the classical finite element technique, inner boundary conditions require a geometrical treatment, hence the computational effort became very important for a large number of micro-cracks. In contrast, in the DG method the inner boundary con-

ditions are modeled by the flux choice without any additional computational cost even for many micro-cracks.

We chose to adapt here the second order numerical scheme, proposed in [46] (the explicit leapfrog scheme in time and a centered flux choice for the inner element faces) for the elastic wave propagation in homogeneous isotropic media. The nonlinear conditions on the micro-cracks are treated as special flux choices. The resulting nonlinear equations at each time step are solved by using the augmented Lagrangian technique. The numerical results obtained with this numerical scheme will be compared to a nontrivial analytical solution to see its mesh size and time step sensitivity.

The numerical scheme will be used for a *numerical upscaling homogenization* to find the effective properties of the damaged material and to study the wave propagation (speed, amplitude, wavelength, etc.) in an isotropic material with micro-cracks and to analyze how a loading pulse is affected by the presence of micro-cracks.

Finally we will illustrate how our DG method can be used to investigate more complex wave propagation phenomena as a blast-wave propagation in a ceramic block with an anisotropic crack distribution.

11.2 Problem statement

Let $\mathcal{D} \subset \mathbb{R}^3$ be an elastic domain which contains an internal boundary (a set of cracks) $\Sigma \subset \overline{\mathcal{D}}$ (see Figure 11.1 for a schematic representation). We are looking for the displacement $\boldsymbol{u} : [0,T] \times \mathcal{D} \to \mathbb{R}^3$ and the stress tensor $\boldsymbol{\sigma} : [0,T] \times \mathcal{D} \to \mathbb{R}^{3\times 3}_s$ (here $\mathbb{R}^{3\times 3}_s$ is the space of symmetric 3×3 matricies) solution of the following equations

$$\rho^{mass}\ddot{\boldsymbol{u}}(t) = \text{div } \boldsymbol{\sigma}(t) + \rho^{mass}\boldsymbol{b}(t) \qquad \text{in } \mathcal{D}, \tag{11.1}$$

$$\boldsymbol{\sigma} = \mathcal{E}\boldsymbol{\varepsilon} \qquad \text{in } \mathcal{D}, \tag{11.2}$$

$$\boldsymbol{\varepsilon}(\boldsymbol{u}) = \frac{1}{2}(\nabla \boldsymbol{u} + \nabla^t \boldsymbol{u}) \qquad \text{in } \mathcal{D}, \tag{11.3}$$

where $\boldsymbol{\varepsilon}$ is the small strain tensor, $\rho^{mass}\boldsymbol{b}$ are the volume forces and $\mathcal{E}$ is the fourth order tensor of the elastic coefficients. If we denote by $\boldsymbol{v} = \dot{\boldsymbol{u}}$ the velocity field and by $\mathcal{A} = \mathcal{E}^{-1}$ the compliance tensor then (11.2) reads

$$\mathcal{A}\dot{\boldsymbol{\sigma}}(t) = \boldsymbol{\varepsilon}(\boldsymbol{v}(t)). \tag{11.4}$$

Let $\boldsymbol{n}$ be the normal at Σ oriented from $-$ to $+$ side as defined on the figure 11.1 . We define the jump $[\varphi]$ of φ by the difference $\varphi^+ - \varphi^-$. The boundary $\partial\mathcal{D}$ of $\mathcal{D}$ will be divided into two parts: the internal boundary Σ, and the "loading" boundary, which is the union of two disjoints parts Σ_v and Σ_σ, i.e. $\partial\mathcal{D} = \Sigma \cup \Sigma_v \cup \Sigma_\sigma$ On the external boundary $\Sigma_v \cup \Sigma_\sigma$ we

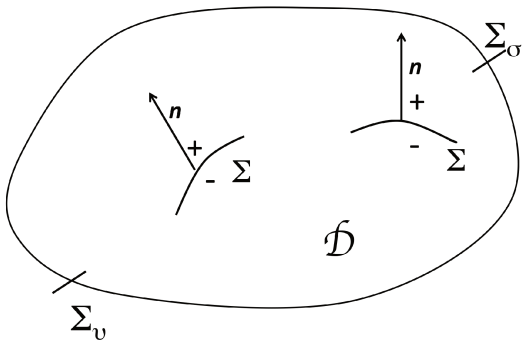

Figure 11.1: Representation of the domain $\mathcal{D}$ and of its boundary $\partial\mathcal{D} = \Sigma \cup \Sigma_v \cup \Sigma_\sigma$.

impose the displacement and the stress vector:

$$\boldsymbol{u}(t) = \boldsymbol{U}(t) \text{ on } \Sigma_v, \quad \boldsymbol{\sigma n}(t) = \boldsymbol{F}_s(t) \text{ on } \Sigma_\sigma, \tag{11.5}$$

while on the internal boundary Σ we prescribe unilateral contact with Coulomb friction. The non penetration Signorini conditions are

$$[\boldsymbol{\sigma}]\boldsymbol{n} = 0 \qquad \text{on } \Sigma; \tag{11.6}$$

$$[\boldsymbol{u}] \cdot \boldsymbol{n} \geqslant 0; \quad \sigma_n \leqslant 0; \quad \sigma_n([\boldsymbol{u}] \cdot \boldsymbol{n}) = 0 \qquad \text{on } \Sigma, \tag{11.7}$$

while

$$|\boldsymbol{\sigma}_T| + \mu_f \sigma_n \leqslant 0, \quad (|\boldsymbol{\sigma}_T| + \mu_f \sigma_n)[\dot{\boldsymbol{u}}_T] = 0 \text{ and } \quad \frac{[\dot{\boldsymbol{u}}_T]}{|[\dot{\boldsymbol{u}}_T]|} = -\frac{\boldsymbol{\sigma}_T}{|\boldsymbol{\sigma}_T|}, \tag{11.8}$$

are the Coulomb friction conditions, with μ_f the Coulomb coefficient. We have used here the normal and tangential decomposition $\sigma_n = \sigma\boldsymbol{n} \cdot \boldsymbol{n}$, $\boldsymbol{\sigma}_T = \boldsymbol{\sigma n} - \sigma_n \boldsymbol{n}$, $\boldsymbol{u}_T = \boldsymbol{u} - (\boldsymbol{u} \cdot \boldsymbol{n})\boldsymbol{n}$.

The unilateral contact equation (11.7) could be replaced by the normal compliance law introduced by Martins and Oden [82, 94]

$$\sigma_n = -C_n [[\boldsymbol{u}] \cdot \boldsymbol{n}]_-^{m_n} \text{ on } \Sigma, \tag{11.9}$$

where $C_n > 0$ and $m_n > 0$ could be either physical or numerical parameters and $[x]_- =$

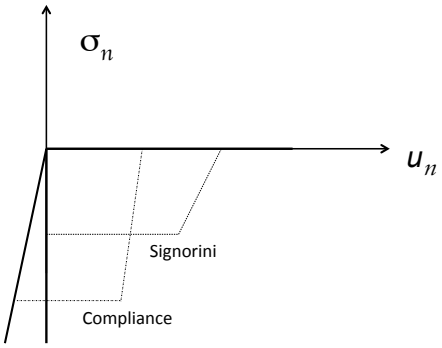

Figure 11.2: Representation of Signorini unilateral conditions and of the compliance law.

$\frac{1}{2}(-x+|x|)$ is the negative part of x. Indeed, as we see from Figure 11.2, the compliance law is the asymptotic approximation of unilateral non penetration condition (11.7) for $C_n \to +\infty$.

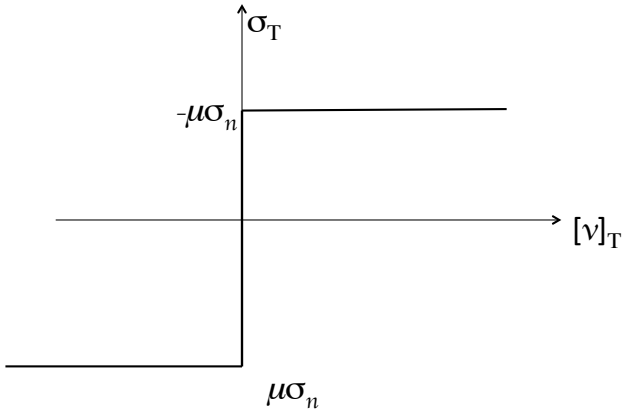

Figure 11.3: Representation of Coulomb friction law.

Let us write the Coulomb friction law (11.8) as a variational inequality. This will be useful in developing the numerical approach. For that, let us consider the set of admissible tangential stress

$$\mathcal{T}^t = \{\boldsymbol{\tau} : \mathcal{D} \to \mathbb{R}^{3\times 3}_s; |\boldsymbol{\tau}_T| + \mu_f \sigma_n(t) \leqslant 0 \text{ on } \Sigma\}. \tag{11.10}$$

Then (11.8) is equivalent with

$$\boldsymbol{\sigma}(t) \in \mathcal{T}^t; \quad [\dot{\boldsymbol{v}}(t)]_T \cdot (\boldsymbol{\tau}_T - \boldsymbol{\sigma}_T(t)) \leqslant 0 \quad \text{for all } \tau \in \mathcal{T}^t \tag{11.11}$$

We complete the field equations and the boundary conditions with the initial conditions

$$\boldsymbol{u}(0) = \boldsymbol{u}_0 \text{ (or } \boldsymbol{\sigma}(0) = \boldsymbol{\sigma}^0 = \mathcal{A}\boldsymbol{\varepsilon}(\boldsymbol{u}_0)), \quad \boldsymbol{v}(0) = \boldsymbol{v}^0, \quad \text{in } \mathcal{D}. \tag{11.12}$$

The initial and boundary problem can be formulated now as follows: find the displacement $\boldsymbol{u} : [0,T] \times \mathcal{D} \to \mathbb{R}^3$ (or equivalently the velocity $\boldsymbol{v} = \dot{\boldsymbol{u}} : [0,T] \times \mathcal{D} \to \mathbb{R}^3$) and the stress $\boldsymbol{\sigma} : [0,T] \times \mathcal{D} \to \mathbb{R}^{3\times 3}_S$, solution of (11.1)-(11.3) with the external boundary conditions (11.5), the nonlinear internal boundary conditions (11.6)-(11.8) (or (11.9) instead of (11.7)) and the initial conditions (11.12).

CHAPTER 12

NUMERICAL APPROACH

The general framework of the numerical scheme which will be introduced in this chapter is based on the second order numerical scheme proposed by Etienne et al. [46]: the explicit leapfrog scheme in time and a centered flux choice for the inner element faces. The nonlinear conditions on the micro-cracks will be treated as special flux choices, while the resulting nonlinear equations at each time step are solved by using an augmented Lagrangian technique.

12.1 Time Discretization

In order to discretize the time, we adopt here a second order explicit leap-frog scheme that allows to compute alternatively the velocity $\boldsymbol{v} = \dot{\boldsymbol{u}}$ and the stress $\boldsymbol{\sigma}$ from one half time step to the next. To this end, let $\Delta t > 0$ be the time step and let M be the maximum number of steps $M\Delta t = T$. We denote by $\boldsymbol{u}^k, \boldsymbol{v}^k$ the displacement and the velocity field at $t = k\Delta t$ and $\boldsymbol{\sigma}^{k+\frac{1}{2}}$, $\boldsymbol{\varepsilon}^{k+\frac{1}{2}}$ the stress and the strain at $t = (k + \frac{1}{2})\Delta t$.

The momentum balance law (11.1) is discretized as an explicit equation for the velocity field

$$\frac{\rho^{mass}}{\Delta t}(\boldsymbol{v}^{k+1} - \boldsymbol{v}^k) = \text{div } \boldsymbol{\sigma}^{k+\frac{1}{2}} + \rho^{mass}\boldsymbol{b}^{k+\frac{1}{2}}, \tag{12.1}$$

from now on called "velocity problem". The displacement is obtained from $\dot{\boldsymbol{u}} = \boldsymbol{v}$ as

$$\boldsymbol{u}^{k+1} = \boldsymbol{u}^k + \frac{\Delta t}{2}(\boldsymbol{v}^k + \boldsymbol{v}^{k+1}). \tag{12.2}$$

The time discretization of the constitutive equation (11.4), as from now called "stress problem", reads

$$\mathcal{A}\frac{\boldsymbol{\sigma}^{k+\frac{3}{2}} - \boldsymbol{\sigma}^{k-\frac{1}{2}}}{\Delta t} = \boldsymbol{\varepsilon}(\boldsymbol{v}^{k+1}) \tag{12.3}$$

It is not difficult to write the time discretization of the displacement and stress conditions (11.5)

$$\boldsymbol{v}^{k+1} = \boldsymbol{V}((k+1)\Delta t), \quad \text{on } \mathcal{D}_v, \tag{12.4}$$

$$\boldsymbol{\sigma}^{k+\frac{1}{2}}\boldsymbol{n} = \boldsymbol{F}^k((k+\frac{1}{2})\Delta t), \quad \text{on } \mathcal{D}_\sigma, \tag{12.5}$$

but for the contact and frictional conditions, which relate the stress and velocity/ displacement fields, some special treatments must be made to accommodate fields which are not computed at the same time.

We will develop two numerical strategies to deal with the Signorini condition (11.7). For the first one, called “the compliance method”, we have chosen to write

$$\sigma_n^{k+\frac{1}{2}} = -C_n \left[[\boldsymbol{u}^k]\cdot\boldsymbol{n}\right]_-^{m_n} \quad \text{on } \Sigma. \tag{12.6}$$

For the second strategy, called “Lagrangian approach ” we will write the contact complementary condition as

$$[\boldsymbol{u}^{k+1}]\cdot\boldsymbol{n} \geqslant 0; \quad \sigma_n^{k+\frac{1}{2}} \leqslant 0; \quad \sigma_n^{k+\frac{1}{2}}([\boldsymbol{u}^{k+1}]\cdot\boldsymbol{n}) = 0, \quad \text{on } \Sigma, \tag{12.7}$$

and using (12.2) we write the above complementary conditions (12.7) in a variational form as

$$\boldsymbol{v} \in \mathcal{V}^{k+1}, \quad \sigma_n^{k+\frac{1}{2}}([\boldsymbol{\varphi}]\cdot\boldsymbol{n} - [\boldsymbol{v}^{k+1}]\cdot\boldsymbol{n}) \geqslant 0, \quad \text{on } \Sigma, \quad \text{for all } \boldsymbol{\varphi} \in \mathcal{V}^{k+1}, \tag{12.8}$$

where the cone $\mathcal{V}^{k+1}$ is

$$\mathcal{V}^{k+1} = \{\boldsymbol{\varphi} : \mathcal{D} \to \mathbb{R}^3; \quad [\boldsymbol{u}^k]\cdot\boldsymbol{n} + \frac{\Delta t}{2}([\boldsymbol{v}^k]\cdot\boldsymbol{n} + [\boldsymbol{\varphi}]\cdot\boldsymbol{n}) \geqslant 0 \text{ on } \Sigma\}.$$

In the treatment of the tangential part of the stress vector we consider

$$\mathcal{T}^{k+\frac{3}{2}} = \{\boldsymbol{\tau} : \mathcal{D} \to \mathbb{R}^{3\times 3}_s; |\boldsymbol{\tau}_T| + \mu_f \sigma_n^{k+1} \leqslant 0 \text{ on } \Sigma\}, \tag{12.9}$$

where σ_n^{k+1} will be defined later for each strategy. Then, the frictional complementary condition (11.11) can be written as

$$\boldsymbol{\sigma}^{k+\frac{3}{2}} \in \mathcal{T}^{k+\frac{3}{2}}; \quad [\boldsymbol{v}^{k+1}]_T \cdot (\boldsymbol{\tau}_T - \boldsymbol{\sigma}_T^{k+\frac{3}{2}}) \leqslant 0 \quad \text{ on } \ \Sigma, \tag{12.10}$$

for all $\boldsymbol{\tau} \in \mathcal{T}^{k+\frac{3}{2}}$.

12.2 Space Discretization and Algorithm

In order to give a spatial discretization of the partial differential equations (11.1),(11.2) let $\mathcal{D}$ be discretized by using a family of tetrahedra $\mathcal{T}_h$ with the mesh size h. The discretization space W_h for the velocities $\boldsymbol{v}^k$, the strain $\boldsymbol{\varepsilon}^{k+\frac{1}{2}}$ and the stress $\boldsymbol{\sigma}^{k+\frac{1}{2}}$ fields is the set of polynomial functions of degree d on each tetrahedron $T \in \mathcal{T}_h$, which can have discontinuities between two tetrahedra.

Apart from internal or external boundaries, the stress and velocity fluxes, associated to the discontinuous Galerkin method, were chosen to follow the centered flux scheme, which has very good non-dissipative properties (see BenJemaa et al. [19], Delcourte et al. [31], Etienne et al [46]).

Concerning the Courant-Friedrichs-Lewy (CFL) condition, which links the mesh width and the time step to guarantee numerical stability, there is no mathematical proof for unstructured meshes associated to the second-order explicit leap-frog scheme used here. However, a heuristic stability criterion, that usually works well, was found by Kaser et al. [72]

$$\Delta t < \frac{1}{2d+1} \min_{T\in\mathcal{T}_h} \frac{2r(T)}{c_P(T)}, \tag{12.11}$$

where $r(T)$ is the radius of the sphere inscribed in the element T and $c_P(T)$ is the P-wave velocity in the element T. For structured or uniform meshes we will denote by CFL the non-dimensional parameter

$$CFL = \frac{\Delta t}{h} c_0, \tag{12.12}$$

where c_0 is the reference wave velocity of the process.

12.2.1 Velocity Problem

Let us fix the time iteration $k > 0$. If we multiply (12.1) by $\boldsymbol{\varphi} \in W_h^3$ and we use the Green formula, then the variational problem on each tetrahedron T of $\mathcal{T}_h$ reads:

$$\int_T \left[\frac{\rho^{mass}}{\Delta t}(\boldsymbol{v}^{k+1} - \boldsymbol{v}^k) \cdot \boldsymbol{\varphi} + \boldsymbol{\sigma}^{k+\frac{1}{2}} : \boldsymbol{\varepsilon}(\boldsymbol{\varphi}) \right] \, dv = \int_{\partial T} \mathcal{F}_\sigma^{k+\frac{1}{2}} \cdot \boldsymbol{\varphi} \, da + \int_T \rho^{mass} \boldsymbol{b}^{k+\frac{1}{2}} \cdot \boldsymbol{\varphi} \, dv, \tag{12.13}$$

where $\boldsymbol{n}$ is the unit normal to ∂T outward T and $\mathcal{F}_\sigma^{k+\frac{1}{2}}$is the stress flux which will be derived below. If ∂T is not included in the boundary of $\mathcal{D}$ (i.e. $\partial T \cap \partial \mathcal{D} = \emptyset$) then we use the central flux scheme:

$$\mathcal{F}_\sigma^{k+\frac{1}{2}} = \boldsymbol{\sigma}^{k+\frac{1}{2}} \boldsymbol{n} + \frac{1}{2} [\boldsymbol{\sigma}]^{k+\frac{1}{2}} \cdot \boldsymbol{n}, \qquad \text{on } \partial T \cap \mathcal{D}.$$

On Σ_σ, the flux is derived from the stress boundary conditions :

$$\mathcal{F}_\sigma^{k+\frac{1}{2}} = F((k + \frac{1}{2})\Delta t), \qquad \text{on } \partial T \cap \Sigma_\sigma$$

while on the velocity boundary Σ_v we put

$$\mathcal{F}_\sigma^{k+\frac{1}{2}} = \boldsymbol{\sigma}^{k+\frac{1}{2}} \boldsymbol{n}, \qquad \text{on } \partial T \cap \Sigma_v$$

The stress flux $\mathcal{F}_\sigma^{k+\frac{1}{2}}$ could be decomposed in the normal flux $\mathcal{F}_{\sigma_n}^{k+\frac{1}{2}}$ and the tangential flux $\mathcal{F}_{\sigma_T}^{k+\frac{1}{2}}$:

$$\mathcal{F}_\sigma^{k+\frac{1}{2}} = \mathcal{F}_{\sigma_n}^{k+\frac{1}{2}} \boldsymbol{n} + \mathcal{F}_{\sigma_T}^{k+\frac{1}{2}}, \qquad \mathcal{F}_{\sigma_T}^{k+\frac{1}{2}} \cdot \boldsymbol{n} = 0.$$

To define the flux $\mathcal{F}_\sigma^{k+\frac{1}{2}}$ on the inner boundary Σ we should distinguish two cases corresponding to two numerical approaches.

Lagrangian Approach

In the case of the "Lagrangian approach", if we use (12.13) with $\boldsymbol{\varphi} - \boldsymbol{v}^{k+1}$ instead of $\boldsymbol{\varphi}$ and we do the summation over all triangles we get

$$\begin{aligned}\int_{\mathcal{D}} \left[\frac{\rho^{mass}}{\Delta t}(\boldsymbol{v}^{k+1} - \boldsymbol{v}^{k}) \cdot (\boldsymbol{\varphi} - \boldsymbol{v}^{k+1}) + \boldsymbol{\sigma}^{k+\frac{1}{2}} : \boldsymbol{\varepsilon}(\boldsymbol{\varphi} - \boldsymbol{v}^{k+1})\right] \, dv - \\ \int_{\mathcal{D}} \rho^{mass} \boldsymbol{b}^{k+\frac{1}{2}} \cdot (\boldsymbol{\varphi} - \boldsymbol{v}^{k+1}) \, dv = \sum_{T \in \mathcal{T}_h} \int_{\partial T} \mathcal{F}_{\sigma}^{k+\frac{1}{2}} \cdot (\boldsymbol{\varphi} - \boldsymbol{v}^{k+1}) \, da\end{aligned} \tag{12.14}$$

Having in mind that

$$\sum_{T \in \mathcal{T}_h} \int_{\partial T \cap \Sigma} \mathcal{F}_{\sigma_n}^{k+\frac{1}{2}} \cdot (\boldsymbol{\varphi} \cdot \boldsymbol{n} - \boldsymbol{v}^{k+1} \cdot \boldsymbol{n}) \, da = \int_{\Sigma} \mathcal{F}_{\sigma_n}^{k+\frac{1}{2}} \cdot ([\boldsymbol{\varphi}] \cdot \boldsymbol{n} - [\boldsymbol{v}]^{k+1} \cdot \boldsymbol{n}) \, da$$

we get that the last term in (12.14) can be written as

$$\begin{aligned}\sum_{T \in \mathcal{T}_h} \Big(\int_{\partial T \setminus \Sigma} \mathcal{F}_{\sigma}^{k+\frac{1}{2}} \cdot (\boldsymbol{\varphi} - \boldsymbol{v}^{k+1}) \, da + \int_{\partial T \cap \Sigma} \mathcal{F}_{\sigma_T}^{k+\frac{1}{2}} \cdot (\boldsymbol{\varphi} - \boldsymbol{v}^{k+1}) \, da \\ + \int_{\partial T \cap \Sigma} \mathcal{F}_{\sigma_n}^{k+\frac{1}{2}} \cdot ([\boldsymbol{\varphi}] \cdot \boldsymbol{n} - [\boldsymbol{v}]^{k+1} \cdot \boldsymbol{n}) \, da \Big).\end{aligned}$$

If we choose now

$$\mathcal{F}_{\sigma}^{k+\frac{1}{2}} = \mathcal{F}_{\sigma_T}^{k+\frac{1}{2}} = \boldsymbol{\sigma}_T^{k+\frac{1}{2}} + \frac{1}{2}[\boldsymbol{\sigma}]_T^{k+\frac{1}{2}}, \quad \mathcal{F}_{\sigma_n}^{k+\frac{1}{2}} = 0, \quad \text{on } \partial T \cap \Sigma,$$

then, from (12.8) we find the following variational inequality for $\boldsymbol{v}^{k+1} \in \mathcal{V}^{k+1}$

$$\begin{aligned}\int_{\mathcal{D}} \left[\frac{\rho^{mass}}{\Delta t}(\boldsymbol{v}^{k+1} - \boldsymbol{v}^{k}) \cdot (\boldsymbol{\varphi} - \boldsymbol{v}^{k+1}) + \boldsymbol{\sigma}^{k+\frac{1}{2}} : \boldsymbol{\varepsilon}(\boldsymbol{\varphi} - \boldsymbol{v}^{k+1})\right] \, dv \geqslant \\ \int_{\mathcal{D}} \rho^{mass} \boldsymbol{b}^{k+\frac{1}{2}} \cdot (\boldsymbol{\varphi} - \boldsymbol{v}^{k+1}) \, dv + \sum_{T \in \mathcal{T}_h} \int_{\partial T} \mathcal{F}_{\sigma}^{k+\frac{1}{2}} \cdot (\boldsymbol{\varphi} - \boldsymbol{v}^{k+1}) \, da,\end{aligned} \tag{12.15}$$

for all $\boldsymbol{\varphi} \in \mathcal{V}^{k+1}$.

To solve the variational inequality (12.15) we use here a Lagrangian approach. For that let

$$\Gamma_h = \{\gamma : \Sigma \to \mathbb{R}; \quad \gamma|_{\partial T} \in \mathbb{P}_d\},$$

be the Lagrange multipliers space and let $\mathcal{L}_v$ be the Lagrangian defined by

$$\mathcal{L}_v(\boldsymbol{\varphi},\gamma) = \frac{1}{2}\int_{\mathcal{D}} \frac{\rho^{mass}}{\Delta t}|\boldsymbol{\varphi}|^2 - \int_{\mathcal{D}} \frac{\rho^{mass}}{\Delta t}\boldsymbol{v}^k\cdot\boldsymbol{\varphi} + \int_{\mathcal{D}} \boldsymbol{\sigma}^{k+1} : \boldsymbol{\varepsilon}(\boldsymbol{\varphi}) -$$
$$\int_{\mathcal{D}} \rho^{mass}\boldsymbol{b}^{k+\frac{1}{2}}\cdot\boldsymbol{\varphi} + \sum_{T\in\mathcal{T}_h}\int_{\partial T} \mathcal{F}_\sigma^{k+\frac{1}{2}}\cdot\boldsymbol{\varphi} - \int_\Sigma \frac{2}{\Delta t}\left\{[\boldsymbol{u}]^k\cdot\boldsymbol{n} + \frac{\Delta t}{2}([\boldsymbol{v}]^k\cdot\boldsymbol{n} + [\boldsymbol{\varphi}]\cdot\boldsymbol{n})\right\}\gamma.$$

At each time step k we start the Uzawa algorithm with $\gamma_0^{k+1} = \gamma^k$ and we compute $\boldsymbol{v}_i^{k+1}$ solution of $\mathcal{L}_v(\boldsymbol{v}_i^{k+1},\gamma_{i-1}^{k+1}) \leqslant \mathcal{L}_v(\boldsymbol{\varphi},\gamma_{i-1}^{k+1})$ for all $\boldsymbol{\varphi}$. Since $\mathcal{L}_v$ is quadratic we get the following equation for $\boldsymbol{v}_i^{k+1} \in W_h^3$

$$\begin{aligned}&\int_{\mathcal{D}} \frac{\rho^{mass}}{\Delta t}(\boldsymbol{v}_i^{k+1} - \boldsymbol{v}^k)\cdot\boldsymbol{\varphi} - \int_\Sigma \gamma_i^{k+1}[\boldsymbol{\varphi}]\cdot\boldsymbol{n} + \int_{\mathcal{D}} \boldsymbol{\sigma}^{k+\frac{1}{2}} : \boldsymbol{\varepsilon}(\boldsymbol{\varphi}) = \\ &\sum_{T\in\mathcal{T}_h}\int_{\partial T\setminus\Sigma} \mathcal{F}_\sigma^{k+\frac{1}{2}}\cdot\boldsymbol{\varphi} - \int_{\mathcal{D}} \rho^{mass}\boldsymbol{b}^{k+\frac{1}{2}}\cdot\boldsymbol{\varphi},\end{aligned} \tag{12.16}$$

for all $\boldsymbol{\varphi} \in W_h^3$. Let us remark that in the above linear system for the velocity field we deal with the same matrix at each time iteration k and at each Uzawa iteration i. That means that the computational cost of each iteration is low, hence the algorithm for solving the nonlinear non-penetration condition does not introduce an important additional cost. To have less Uzawa iterations one can imagine an augmented Lagrangian approach by replacing $\mathcal{L}_v$ with

$$\mathcal{L}_v^a(\boldsymbol{\varphi},\gamma) = \mathcal{L}_v(\boldsymbol{\varphi},\gamma) + \int_\Sigma \frac{2r_v}{\Delta t}\left[[\boldsymbol{u}]^k\cdot\boldsymbol{n} + \frac{\Delta t}{2}([\boldsymbol{v}]^k\cdot\boldsymbol{n} + [\boldsymbol{\varphi}]\cdot\boldsymbol{n})\right]_-^2,$$

where $[x]_- = (|x| - x)/2$ is the negative value and r_v is some numerical parameter discussed below. If an augmented Lagrangian technique is used then the linear system to be solved is different at each Uzawa iteration i. In this case one have to evaluate if the benefits of the augmented Lagrangian technique are not overpassed by the additional cost for solving the linear system.

After the computation of the velocity field $\boldsymbol{v}_i^{k+1}$ one can compute the displacement

$$\boldsymbol{u}_i^{k+1} = \boldsymbol{u}^k + \frac{\Delta t}{2}(\boldsymbol{v}^k + \boldsymbol{v}_i^{k+1}), \tag{12.17}$$

and we update the Lagrangian multiplayer γ^{k+1} through the Uzawa algorithm

$$\gamma_{i+1}^{k+1} = \gamma_i^k + r_v[[\boldsymbol{u}_i^{k+1}]\cdot\boldsymbol{n}]_-, \tag{12.18}$$

where r_v is a numerical parameter which has to be chosen. In general, if r_v is too small, the convergence is too slow and if r is too large, then the algorithm does not converge. The convergence is achieved when the difference $\|\boldsymbol{v}_i^{k+\frac{3}{2}} - \boldsymbol{v}_{i-1}^{k+1}\|$ is small enough with respect to a chosen tolerance.

Finally, we choose the normal stress in the definition of $\mathcal{T}^{k+\frac{3}{2}}$ to be

$$\boldsymbol{\sigma}_n^{k+1} = -\gamma^{k+1}.$$

In conclusion, the velocity problem (12.1) is reduced to the variational inequality (12.15) which is solved with the Lagrangian approach by using the Uzawa algorithm (12.16), (12.18).

Compliance Algorithm

The compliance approach makes use of (12.6) to choose the flux

$$\mathcal{F}_\sigma^{k+\frac{1}{2}} = \boldsymbol{\sigma}_T^{k+\frac{1}{2}} + \frac{1}{2}[\boldsymbol{\sigma}]_T^{k+\frac{1}{2}} - C_n \left[\boldsymbol{u}^k\right] \cdot \boldsymbol{n}\big]_-^{m_n} \boldsymbol{n} \quad \text{on } \partial T \cap \Sigma. \tag{12.19}$$

With this choice of stress flux, by summation of (12.13) over all $T \in \mathcal{T}_h$, we get the following linear equation for the velocity $\boldsymbol{v}^{k+1}$:

$$\begin{aligned} &\int_{\mathcal{D}} \left[\frac{\rho^{mass}}{\Delta t}(\boldsymbol{v}^{k+1} - \boldsymbol{v}^k) \cdot \boldsymbol{\varphi} + \boldsymbol{\sigma}^{k+\frac{1}{2}} : \boldsymbol{\varepsilon}(\boldsymbol{\varphi}) \right] \, dv = \sum_{T \in \mathcal{T}_h} \int_{\partial T} \mathcal{F}_\sigma^{k+\frac{1}{2}} \cdot \boldsymbol{\varphi} \, da \\ &+ \int_{\mathcal{D}} \rho^{mass} \boldsymbol{b}^{k+\frac{1}{2}} \cdot \boldsymbol{\varphi}, \quad \text{for all } \boldsymbol{\varphi} \in W_h^3. \end{aligned} \tag{12.20}$$

After computing $\boldsymbol{v}^{k+1}$, we find $\boldsymbol{u}^{k+1}$ from (12.2) and the normal stress is given by

$$\sigma_n^{k+1} = -\, C_n[[\boldsymbol{u}^{k+1}] \cdot \boldsymbol{n}]_-^{m_n}, \quad \text{on } \Sigma. \tag{12.21}$$

We remark that, unlike to the Lagrangian approach, for the compliance approach the velocity problem (12.1) is reduced to (12.20) without any additional computational cost.

12.2.2 Stress Problem

To give the space discretization of the stress problem (12.3) let $\mathcal{S}_h^{k+\frac{3}{2}}$ be the set of admissible tangential stress:

$$\mathcal{S}_h^{k+\frac{3}{2}} = \{\boldsymbol{\tau} \in W_{h,s}^{3\times 3}; |\boldsymbol{\tau}_T| + \mu_f \sigma_n^{k+\frac{3}{2}} \leqslant 0 \ \text{ on } \ \Sigma\}.$$

If we multiply (12.3) by $\boldsymbol{\psi} - \boldsymbol{\tau}^{k+\frac{3}{2}}$ ($\boldsymbol{\psi} \in \mathcal{S}_h^{k+\frac{3}{2}}$), and integrate the result over each tetrahedron $T \in \mathcal{T}_h$, we get:

$$\begin{aligned} &\int_T \mathcal{A}\left(\frac{\boldsymbol{\sigma}^{k+\frac{3}{2}} - \boldsymbol{\sigma}^{k+\frac{1}{2}}}{\Delta t}\right) : (\boldsymbol{\psi} - \boldsymbol{\sigma}^{k+\frac{3}{2}}) + \int_T \boldsymbol{v}^{k+1} \cdot \operatorname{div}(\boldsymbol{\psi} - \boldsymbol{\sigma}^{k+\frac{3}{2}}) = \\ &\int_{\partial T} (\boldsymbol{\psi} - \boldsymbol{\sigma}^{k+\frac{3}{2}})\boldsymbol{n} \cdot \mathcal{F}_v^{k+1}, \end{aligned} \tag{12.22}$$

where $\mathcal{F}_v^{k+1}$ is the velocity flux. If ∂T is not on the boundary of $\mathcal{D}$, we use, as for the stress flux, the centered flux scheme

$$\mathcal{F}_v^{k+1} = \boldsymbol{v}^{k+1} + \frac{1}{2}[\boldsymbol{v}]^{k+1}, \quad \text{ on } \ \partial T \cap \mathcal{D}.$$

On the boundary Σ_v we have

$$\mathcal{F}_v^{k+1} = V((k+1)\Delta t), \quad \text{ on } \ \partial T \cap \Sigma_v,$$

while on the stress boundary we choose the flux to be

$$\mathcal{F}_v^{k+1} = \boldsymbol{v}^{k+1}, \quad \text{ on } \ \partial T \cap \Sigma_\sigma.$$

For $\partial T \subset \Sigma$ we have to decompose the velocity flux $\mathcal{F}_v^{k+1}$ into the tangential $\mathcal{F}_{v_T}^{k+1}$ and the normal part $\mathcal{F}_{v_n}^{k+1}$

$$\mathcal{F}_v^{k+1} = \mathcal{F}_{v_T}^{k+1} + \mathcal{F}_{v_n}^{k+1}\boldsymbol{n}, \quad \mathcal{F}_{v_T}^{k+1} \cdot \boldsymbol{n} = 0.$$

Having in mind that $\boldsymbol{v}_T^{k+1} = (\boldsymbol{v}_T^{k+1} + \frac{1}{2}[\boldsymbol{v}]_T^{k+1}) - \frac{1}{2}[\boldsymbol{v}]_T^{k+1}$ from (12.10) we deduce

$$\boldsymbol{v}_T^{k+1} \cdot (\psi_T - \boldsymbol{\sigma}_T^{k+\frac{3}{2}}) \geqslant (\boldsymbol{v}_T^{k+1} + \frac{1}{2}[\boldsymbol{v}]_T^{k+1}) \cdot (\psi_T - \boldsymbol{\sigma}_T^{k+\frac{3}{2}}) \quad \text{ on } \ \Sigma. \tag{12.23}$$

If we choose $\mathcal{F}_{v_n}^{k+1} = \boldsymbol{v}^{k+1} \cdot \boldsymbol{n}$ for the normal part, while for the tangential part we consider the centered flux $\mathcal{F}_{v_T}^{k+1} = \boldsymbol{v}_T^{k+1} + \frac{1}{2}[\boldsymbol{v}]_T^{k+1}$, i.e.

$$\mathcal{F}_v^{k+1} = \boldsymbol{v}_T^{k+1} + \frac{1}{2}[\boldsymbol{v}]_T^{k+1} + (\boldsymbol{v}^{k+1} \cdot \boldsymbol{n})\boldsymbol{n}, \quad \text{ on } \ \partial T \cap \Sigma \tag{12.24}$$

then, using the last inequality (12.23), one can sum (12.22) for all $T \in \mathcal{T}_h$ to get the following variational inequality for the stress field $\boldsymbol{\sigma}^{k+\frac{3}{2}} \in \mathcal{S}_h^{k+\frac{3}{2}}$:

$$\begin{aligned} &\int_{\mathcal{D}} \frac{1}{\Delta t}\mathcal{A}(\boldsymbol{\sigma}^{k+\frac{3}{2}} - \boldsymbol{\sigma}^{k+\frac{1}{2}}) : (\boldsymbol{\psi} - \boldsymbol{\sigma}^{k+\frac{3}{2}}) + \int_{\mathcal{D}} \boldsymbol{v}^{k+1} \cdot \mathrm{div}(\boldsymbol{\psi} - \boldsymbol{\sigma}^{k+\frac{3}{2}}) \\ &\geqslant \sum_{T\in\mathcal{D}_h} \int_{\partial T} \mathcal{F}_v^{k+1} \cdot (\boldsymbol{\psi} - \boldsymbol{\sigma}^{k+\frac{3}{2}})\boldsymbol{n}, \quad \text{for all } \boldsymbol{\psi} \in \mathcal{S}_h^{k+\frac{3}{2}}. \end{aligned} \tag{12.25}$$

In order to solve the variational inequality (12.25) we use here a Lagrangian formulation and the Uzawa algorithm. For that, let Λ_h be the Lagrange multipliers space

$$\Lambda_h = \{\lambda : \Sigma \to \mathbb{R}^3;\ \lambda \cdot \boldsymbol{n} = 0;\ \lambda|_{\partial T} \in \mathbb{P}_d\}$$

and let us define the Lagrangian $\mathcal{L}_s : W_{h,s}^{3\times 3} \times \Lambda_h \to \mathbb{R}$ as

$$\begin{aligned} \mathcal{L}_s(\boldsymbol{\psi}, \lambda) = \frac{1}{2}\int_{\mathcal{D}} \frac{1}{\Delta t}\mathcal{A}\boldsymbol{\psi} : \boldsymbol{\psi} - \int_{\mathcal{D}} \frac{1}{\Delta t}\mathcal{E}\boldsymbol{\sigma}^{k+\frac{1}{2}} : \boldsymbol{\psi} - \int_{\mathcal{D}} \boldsymbol{v}^{k+1} \cdot \mathrm{div}\boldsymbol{\psi} \\ - \sum_{T\in\mathcal{T}_h} \int_{\partial T} \mathcal{F}_v^{k+1} \cdot \boldsymbol{\psi}\boldsymbol{n} + \frac{1}{2}\int_{\Sigma} \lambda(|\boldsymbol{\psi}_T|^2 - (\mu_f \sigma_n^{k+1})^2). \end{aligned}$$

At each time step k we start the Uzawa algorithm by choosing the Lagrange multiplier to be $\lambda_0^{k+1} = \lambda^k$. At each iteration i we compute $\boldsymbol{\sigma}_i^{k+\frac{3}{2}}$ to be the minimum of $\mathcal{L}_s$ with respect to the first variable, i.e. $\mathcal{L}_s(\boldsymbol{\sigma}_i^{k+\frac{3}{2}}, \lambda_{i-1}^{k+1}) \leqslant \mathcal{L}_s(\boldsymbol{\psi}, \lambda_i^{k+1})$ for all $\boldsymbol{\psi} \in W_h^{3\times 3}$. Since $\mathcal{L}_s$ is quadratic, we get the following linear equation for the stress field $\boldsymbol{\sigma}_i^{k+\frac{3}{2}}$

$$\begin{aligned} &\int_{\mathcal{D}} \frac{1}{\Delta t}\mathcal{A}(\boldsymbol{\sigma}_i^{k+\frac{3}{2}} - \boldsymbol{\sigma}_i^{k+\frac{1}{2}}) : \boldsymbol{\psi} + \int_{\Sigma} \lambda_{i-1}^{k+1}\boldsymbol{\sigma}_{i,T}^{k+\frac{3}{2}} \cdot \boldsymbol{\psi}_T - \int_{\mathcal{D}} \boldsymbol{v}^{k+1} \cdot \mathrm{div}\boldsymbol{\psi} \\ &= \sum_{T\in\mathcal{T}_h} \int_{\partial T} \mathcal{F}_v^{k+1} \cdot \boldsymbol{\psi}\boldsymbol{n}, \quad \text{for all } \boldsymbol{\psi} \in W_{h,s}^{3\times 3}. \end{aligned} \tag{12.26}$$

To decrease the number of iterations one can choose to use an augmented Lagrangian technique by using the augmented Lagrangian $\mathcal{L}_s^a$

$$\mathcal{L}_s^a(\boldsymbol{\psi}, \lambda) = \mathcal{L}_s(\boldsymbol{\psi}, \lambda) + \int_{\Sigma} r_s \left[|\boldsymbol{\psi}_T| - \mu_f|\sigma_n^{k+1}|\right]_+^2,$$

instead of $\mathcal{L}_s$. As before, we remark that, since the Lagrange multiplier λ_{i-1}^{k+1} is different at each iteration the linear equation (12.26) has a different matrix at each iteration implying an

important computational extra-cost. For this reason, one could replace it with the following linear system

$$\begin{aligned}&\int_{\mathcal{D}} \frac{1}{\Delta t}\mathcal{A}(\boldsymbol{\sigma}_i^{k+\frac{3}{2}} - \boldsymbol{\sigma}_i^{k+\frac{1}{2}}) : \boldsymbol{\psi} + \int_{\Sigma} \lambda_{i-1}^{k+1}\boldsymbol{\sigma}_{i-1,T}^{k+\frac{3}{2}} \cdot \boldsymbol{\psi}_T - \int_{\mathcal{D}} \boldsymbol{v}^{k+1} \cdot \mathrm{div}\boldsymbol{\psi} \\ &= \sum_{T\in\mathcal{T}_h} \int_{\partial T} \mathcal{F}_v^{k+1} \cdot \boldsymbol{\psi}\boldsymbol{n}, \quad \text{for all } \boldsymbol{\psi} \in W_{h,s}^{3\times 3}.\end{aligned} \tag{12.27}$$

which has the same matrix at all time and Uzawa iterations. Even if the convergence is slower, this version of the Lagrangian approach is computationally attractive.

The Lagrange multipliers are updated from:

$$\lambda_{i+1}^{k+1} = \lambda_i^{k+1} + r_s[|\boldsymbol{\sigma}_{iT}^{k+\frac{3}{2}}|^2 - (\mu_f \sigma_n^{k+1})^2]_+$$

where $r_s > 0$ is a numerical parameter(step) which has to be chosen (if r_s is too small the convergence is too slow and if r_s is too large then the algorithm does not converge). The convergence is achieved when the difference $\|\boldsymbol{\sigma}_{i+1}^{k+\frac{3}{2}} - \boldsymbol{\sigma}_i^{k+\frac{3}{2}}\|$ is small enough with respect to a chosen tolerance.

12.2.3 Frictionless Contact with Compliance

The case without friction is simpler and does not involve any iterative algorithm. The compliance method is used to define the stress flux:

$$\mathcal{F}_\sigma^{k+\frac{1}{2}} = -C_n[[\boldsymbol{u}^k] \cdot \boldsymbol{n}]_-^{m_n}\boldsymbol{n}, \quad \text{on } \partial T \cap \Sigma$$

instead of (12.19) and to solve (12.20) for the velocity problem. Then, if we put

$$\mathcal{F}_v^{k+1} = \boldsymbol{v}^{k+1}, \quad \text{on } \partial T \cap \Sigma,$$

instead of (12.24), we have to solve the following equation for $\boldsymbol{\sigma}^{k+\frac{3}{2}}$

$$\int_{\mathcal{D}} \frac{1}{\Delta t}\mathcal{A}(\boldsymbol{\sigma}^{k+\frac{3}{2}} - \boldsymbol{\sigma}^{k+\frac{1}{2}}) : \boldsymbol{\psi} - \int_{\mathcal{D}} \boldsymbol{v}^k \cdot \mathrm{div}\boldsymbol{\psi} = \sum_{T\in\mathcal{T}_h} \int_{\partial T} \mathcal{F}_v^{k+1} \cdot \boldsymbol{\psi}\boldsymbol{n}$$

for all $\boldsymbol{\psi} \in W_h^{3\times 3}$.

12.3 Testing the numerical schemes

In order to test the above algorithms, we considered two examples for which we can construct an exact solution. In both problems, we have compared the results of our numerical schemes with the analytical solutions. Plane stress conditions (i.e $\sigma_{xz} = \sigma_{yz} = \sigma_{zz} \equiv 0$) in an isotropic homogeneous elastic body $\mathcal{D} = \Omega \times (-r, r)$ are assumed in all cases. The rectangular domain $\Omega = [0, L] \times [-b, b]$, has an internal interface $\Sigma = \{l\} \times [-b, b](\ l < L)$.

In all the computations we have chosen the degree of polynomials to be $d = 2$.

12.3.1 Unilateral Contact Problem

At $y = -b$ and $y = b$, vanishing shear stress and normal displacement are imposed, while a stress free condition is considered at $x = L$ (see Figure 12.1). For $x = 0$, we impose a pulse of time length 2δ and amplitude B on the velocity field $\boldsymbol{v}(t) = (V(t), 0, 0)$ with $V(t) = B\varphi_\delta(t - \delta)$ where $B > 0$ and $\varphi_\delta(s) = \frac{1}{2}(\cos(\frac{s\pi}{\delta}) + 1)$ if $|s| \leqslant \delta$ and $\varphi_\delta(s) = 0$ otherwise. At the inner boundary Σ, we impose a frictionless non penetration Signorini condition:

$$\boldsymbol{\sigma}_T = 0, \quad [\boldsymbol{u}] \cdot \boldsymbol{n} \geqslant 0, \quad \sigma_n[\boldsymbol{u}] \cdot \boldsymbol{n} = 0.$$

For the initial state $t = 0$, we suppose that the elastic body is at rest ($\boldsymbol{v}_0 = 0$) and stress free ($\boldsymbol{\sigma}_0 = 0$).

The initial and boundary conditions are chosen such that we deal with an unidimensional behavior

$$u_x = u_x(t, x), \quad \sigma_{xx} = \sigma_{xx}(t, x), \quad u_y \equiv 0, \quad \sigma_{xy} = 0, \quad \sigma_{yy} = \nu\sigma_{xx}.$$

Denoting by $\tau = \sigma_{xx}, \ v = v_x, \ u = u_x$, the problem is reduced to the following first order hyperbolic system:

$$\begin{cases} \rho^{mass}\dot{v} = \dfrac{\partial \tau}{\partial x}, \\ \dot{\tau} \qquad = \dfrac{E}{1-\nu^2}\dfrac{\partial v}{\partial x}. \end{cases}$$

The time interval of interest will be $[0, T]$ with $T = (3(L - l) + l)/c$ (here c is the wave propagation velocity given by $c = \sqrt{\frac{E}{\rho^{mass}(1-\nu^2)}}$), such that the wave which starts at $x = 0$ has the time to reflect at $x = L$ and then to reflect again at $x = l$.

The propagation of the compressive wave through the unilateral interface Σ is plotted in

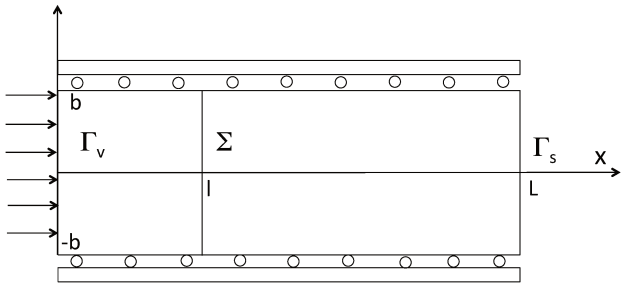

Figure 12.1: Schematic representation of the boundary value problem for testing the unilateral contact algorithm.

figure 12.2. In the fist frame, we see the propagation of a compressive wave generated by the loading boundary condition at $x = 0$. Later (frame 2) it reflects and becomes a traction wave that generates a jump in normal displacement on Σ (frame 3). Then, it is reflected again on Σ as a compressive wave which propagates in the right part of the interface (frame 4).

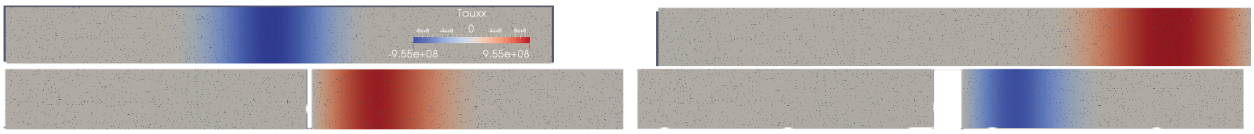

Figure 12.2: The propagation and reflexion of a compressive wave through the unilateral interface Σ with σ_{xx} in a color scale. First frame: the compressive pulse generated by the boundary condition. Second frame: reflexion on the right boundary as a tractional wave. Third frame: the jump of the displacement field on the interface Σ. Forth frame: reflection of the wave in the right side of the interface.

More precisely, we can compute the solution on the fault Σ using the method of characteristics (see figure 12.3 for a schematic representation). For $t \in [0, (2(L-l)+l)/c]$, i.e until the wave reflected at $x = L$ arrives on the fault there is no jump in the velocity field and we get:

$$v(t, l+) = v(t, l-) = V(t - \frac{l}{c}), \quad \tau(t, l) = -\sqrt{\frac{\rho E}{1-\nu^2}} v(t). \tag{12.28}$$

After that, for $t \in [(2(L-l)+l)/c, T]$ we deal with a tractional wave, velocity is positive on the right side of Σ and the stress is vanishing:

$$v(t, l+) = V(t - \frac{2(L-l)+l}{c}), \quad v(t, l-) = 0, \quad \tau(t, l) = 0.$$

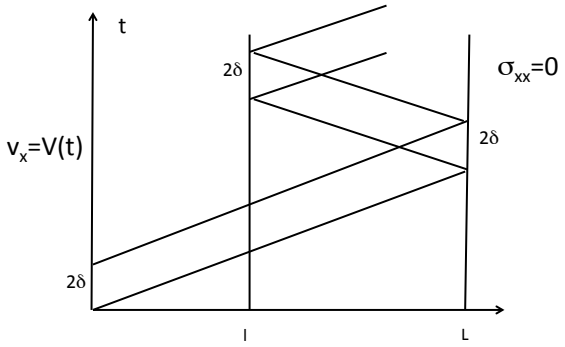

Figure 12.3: Representation of the method of characteristic for the considered contact problem

To test the two proposed methods (Uzawa and compliance), we have done several numerical computations and compared them with the exact solution.

First, we start with the compliance method. Choosing the power $m_n = 1$ in (11.9) we will analyze the parameter C_n and we will try to find an optimal C_n^{opt}, defined as the maximum C_n for which the algorithm is still convergent. For that we tested the compliance method on an uniform mesh with 8 nodes over the fault Σ ($h \simeq 2b/7$). We start by choosing $C_n = \dfrac{15G}{h}$, where h the mesh size and G is is the shear Lamé modulus. For CFL=$\dfrac{1}{15}$ (here CFL= $c_P \Delta t/h$) we have plotted in figure 12.4 the time evolution of the computed velocity on the fault versus the exact solution and in Figure 12.5 the time evolution of the absolute normalized velocity error

$$t \to E(t) = \frac{1}{B}\sqrt{\frac{\int_\Sigma (v_h(t) - v(t)^2)}{|\Sigma|}},$$

where v_h is the computed velocity and v is the exact solution. We noticed that, the numerical scheme captures very well the loading pulse but a numerical artifact appears later (see the zoom). Indeed, we remark the presence of a small (2%) amplitude "bump" having the same duration as the loading pulse. This bump is the reflection on the left boundary of the non-exact propagation of the loading wave through the fault. It can be explained by the fact that the compliance method allows a small interpenetration, related to the compliance (penalty) parameter C_n. Later, we tested $C_n = \dfrac{30G}{h}$ an we obtained an improvement of the error. For bigger values of C_n using the same CFL=1/15 the algorithm does not converge. Therefore,

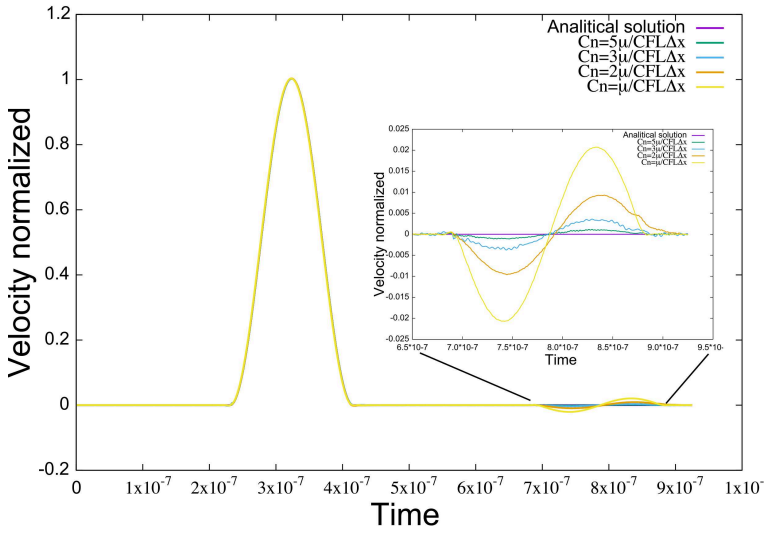

Figure 12.4: Time evolution of the computed normalized velocity $v(t, l-)$ on the fault versus the exact solution using compliance method. Zoom on the bump reflection for different choices of $C_n = 15G/h, 30G/h, 90G/h, 300G/h$ together with the analytical solution.

$C_n^{opt} = \dfrac{30G}{h}$ for this CFL. Later, using the same mesh we changed the time step Δt, by taking CFL=$\dfrac{1}{30}$ and we computed the solution for $C_n = 90G/h$ and a smaller bump. We also tested $C_n = \dfrac{120G}{h}$ and we obtained an improvement but for bigger values of C_n the algorithm diverges. Thus, $C_n^{opt} = \dfrac{120G}{h}$ for CFL=$\dfrac{1}{30}$. For our last test, having the same mesh but with CFL=$\dfrac{1}{60}$ we have chosen $C_n = \dfrac{300G}{h}$. We obtained that the maximum of the error is no longer at the bump but during the loading pulse. For bigger values of C_n the algorithm diverges hence $C_n^{opt} = \dfrac{300G}{h}$ for CFL=$\dfrac{1}{60}$. We conclude that the optimal compliance (penalty) parameter $C_n^{opt} = C_n^{opt}(h, c_P\Delta t, G)$ depends on the size of mesh, time step and the elastic coefficients. Globally, as expected, the error is decreasing for increasing C_n, but the computational cost, related to the number of time iterations, is quickly increasing if a very good accuracy is needed.

For the Uzawa algorithm we have considered the same mesh as before and the CFL was chosen to be CFL=$\dfrac{1}{60}$. Due to the fact that for both algorithms the maximal error is at the beginning and at the end of the pulse, we compared their computed solutions with the solution of the wave propagation problem computed without any unilateral conditions. In figure 12.6, we plotted the evolution of the absolute normalized error in velocity for both

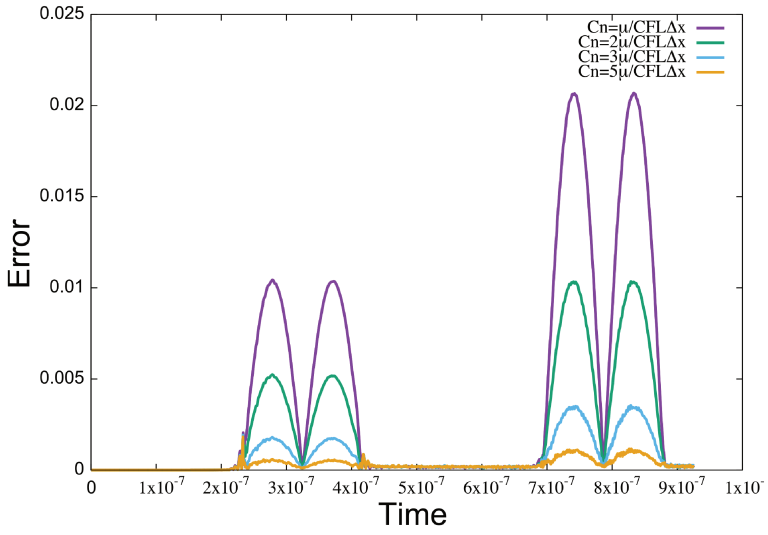

Figure 12.5: Time evolution of the absolute normalized velocity error for different values of $C_n = 15G/h, 30G/h, 90G/h, 300G/h$.

methods (Compliance in violet and Uzawa in green) together with the scheme (discontinuous Galerkin and leap frog) with no contact conditions on the fault (blue). We observe that, in all cases the error increases at the beginning and the end of the loading pulse and is larger for the compliance method than for the Uzawa method. Moreover, while for the Uzawa algorithm and for the "no contact problem" the error is decreasing during the pulse, for the compliance method some "bumps" appear and are reflected at the external boundaries. These last errors, due to the non-respect of the non-penetration condition are specific to the compliance method and are not present in the Uzawa approach.

For the Uzawa method the best choice we found for the numerical parameter r_v was $r_v = \dfrac{300G}{h}$, which is closed to the optimal compliance parameter C_n^{opt}. For this choice of r_v the convergence is rapid at a tolerance around 10^{-4}. If the tolerance is larger than 10^{-3} spurious oscillations could appear and the algorithm is no longer stable. For tolerance smaller that 10^{-4} the computational time increases without any significant decrease of the error.

We have further analyzed the mesh dependency of the numerical error. We have considered 3 different uniform meshes with different numbers of nodes over the fault: 5 nodes, 8 nodes and 11 nodes ($h \simeq 2b/4, 2b/7, 2h/10$). We have plotted the results in figure 12.7 for the compliance method (left) and the Uzawa method (right). As we can see, for all cases

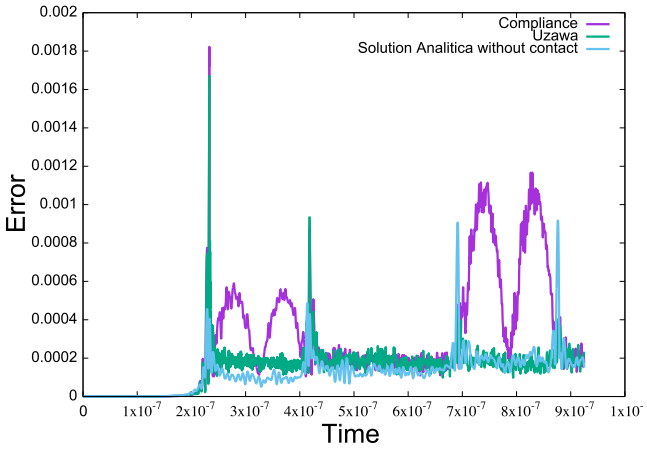

Figure 12.6: Time evolution of the absolute normalized error in velocity found using the compliance method (violet) and Uzawa method (green) compared with the scheme without contact (blue).

the maximal error occurs at the beginning of the pulse. Even if we do not study the rate of convergency, we observed that the error decrease with the refinement of the mesh.

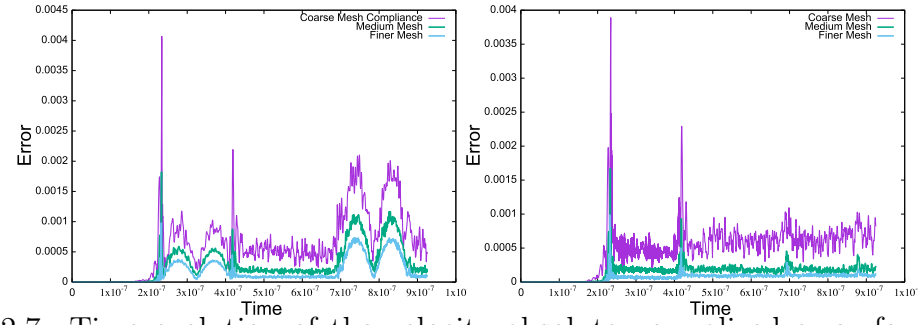

Figure 12.7: Time evolution of the velocity absolute normalized error for the compliance method (left) and Uzawa method (right) for three different meshes: coarse mesh (violet), medium mesh (green) and fine mesh (blue).

We conclude that the Uzawa and compliance methods give accurate results to the contact problem. Generally, the Uzawa scheme is more accurate but it requires a higher computational cost. If a high accuracy is required, the compliance method needs a large penalty parameter and a very small time step. This induces an important extra computational cost and it is not anymore attractive with respect to the Uzawa method. On the other hand, for low or medium accuracy the compliance method seems to be more convenient than the Uzawa method due to it is a good compromise between accuracy and computational cost.

12.3.2 Frictional Contact Problem

For the second test, the body is under a spherical compressive stress $p = B$ acting on all the boundaries, $\sigma_n = -B$ while at $y = -b$ and $y = b$ the tangential displacement is vanishing

$$\sigma_n = -B, \quad \boldsymbol{u}_T = 0 \quad \text{on } y = \pm b.$$

We also impose a vanishing tangential stress at $x = L$, while for $x = 0$ we consider a loading tangential pulse $F(t)$:

$$\sigma_n = -B, \quad \boldsymbol{\sigma}_T(t) = F(t)\boldsymbol{e}_y \quad \text{on } x = 0, \qquad \sigma_n = -B, \quad \boldsymbol{\sigma}_T(t) = 0 \quad \text{on } x = L,$$

with $F(t) = B\varphi_\delta(t - \delta)$ (here $B > 0$ and $\varphi_\delta(s) = \frac{1}{2}(\cos(\frac{s\pi}{\delta}) + 1)$ if $|s| \leqslant \delta$ and $\varphi_\delta(s) = 0$ otherwise). The inner boundary Σ is a frictional contact surface where a Coulomb friction law is considered

$$[\boldsymbol{u}] \cdot \boldsymbol{n} \geqslant 0; \quad \sigma_n \leqslant 0; \quad \sigma_n([\boldsymbol{u}] \cdot \boldsymbol{n}) = 0,$$

$$|\boldsymbol{\sigma}_T| + \mu_f \sigma_n \leqslant 0, \quad (|\boldsymbol{\sigma}_\tau| + \mu_f \sigma_n)[\dot{\boldsymbol{u}}_T] = 0 \text{ and } \quad \frac{[\dot{\boldsymbol{u}}_\tau]}{|[\dot{\boldsymbol{u}}_\tau]|} = -\frac{\boldsymbol{\sigma}_\tau}{|\boldsymbol{\sigma}_\tau|},$$

where μ_f is the frictional coefficient (chosen to be $\mu_f = 0.5$). At $t = 0$, the elastic body is at rest ($\boldsymbol{v}_0 = 0$) and under a spherical pressure $\boldsymbol{\sigma}_0 = -B\boldsymbol{I}$.

The tangential stress condition at $x = 0$ generates a shear wave which will propagate into the body arriving at the frictional interface Σ. Since the amplitude of the shear wave B is larger that the frictional threshold $\mu_f B$, the slab will start to slip and part of the pulse is transmitted on the right side, while the other part will be reflected on left side of the interface. The evolution of shear stress σ_{xy} is plotted in figure 12.8. Let us notice that the problem has an one-dimensional solution with

$$\sigma_{xx} = \sigma_{yy} = -B, \quad v_x = 0, \quad v_y = v(t, x), \quad \sigma_{xy} = \tau(t, x)$$

and the system can be reduced to the following first order hyperbolic system

$$\begin{cases} \rho\dot{v} = \dfrac{\partial \tau}{\partial x} \\ \dfrac{1}{G}\dot{\tau} = \dfrac{\partial v}{\partial x} \end{cases}$$

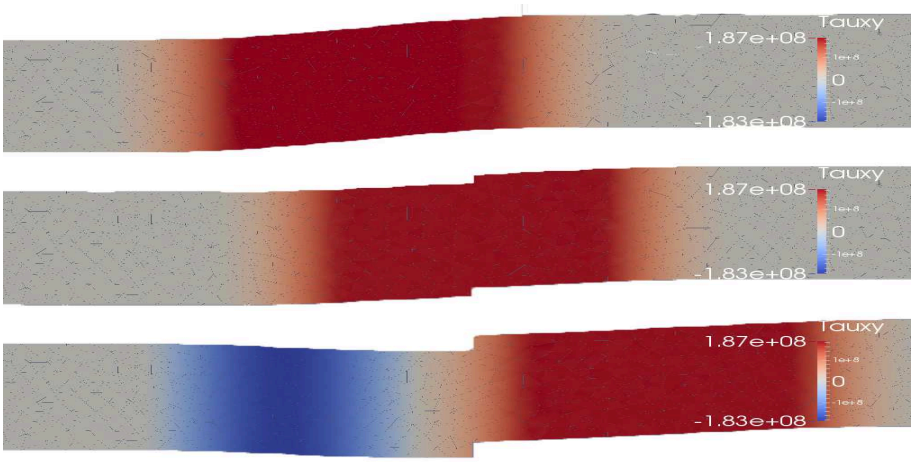

Figure 12.8: Propagation of a shear wave through an interface with friction with the shear stress σ_{xy} in a color scale. In the first frame we observe the loading shear wave propagating into the frictional surface without slipping, in the second frame we observe a frictional slip and in the third frame we observe the reflected wave generated by the frictional slip.

with the nonlinear boundary condition at $x = l$

$$\tau(t,l) \leqslant \mu_f B, \quad (\tau(t,l) - \mu_f B)[v(t,l)] = 0, \quad \text{and} \quad \tau(t,l)[v](t,l) \geq 0,$$

while the other boundary conditions and the initial conditions read

$$\tau(t,0) = F(t), \quad \tau(t,L) = 0, \quad v(0,x) = 0, \quad \tau(0,x) = 0.$$

We can compute the exact solution of the above problem on the fault Σ using the method of characteristics, see Figure 12.9 for a schematic representation. If we denote by t' and t'' the instances when $F(t' - l/c_s) = \mu_f B$ and $F(t'' - l/c_s) = \mu_f B$, with $t' < t''$, then the two slabs will slip ($[v](t,l) > 0$) during the time interval $[t', t'']$, while in the rest of the time no slip occurs ($[v](t,l) = 0$). The analytical solution can be computed for each time interval to be

$$\tau(t,l) = F(t - \frac{l}{c}), \quad v(t,l-) = v(t,l+) = \frac{1}{\sqrt{\rho G}} F(t - \frac{l}{c}),$$

for $t \in [0,t'] \cup [t'',T]$, while for $t \in [t',t'']$ we have

$$\tau(t,l) = \mu_f B, \quad v(t,l-) = \frac{-1}{\sqrt{\rho G}} \mu_f G, \quad v(t,l+) = \frac{1}{\sqrt{\rho G}} (\mu_f B - 2F(t - \frac{l}{c})).$$

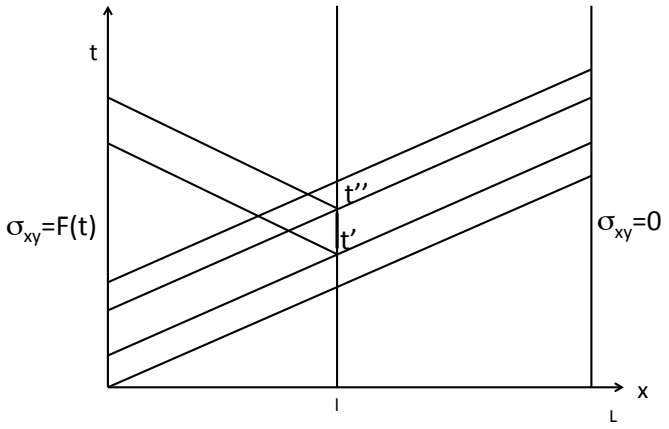

Figure 12.9: Representation of the method of characteristics for the frictional problem.

We have done several numerical tests and we compared the results with the analytical solution. In figure 12.10 we have plotted the time evolution of the normalized analytical stress versus the computed stress together with the loading pulse (analytical stress without friction) on the frictional interface. We observe a plateau in the loading pulse corresponding to the activation of the friction conditions, generating frictional slip and a wave reflection. We remark a very good approximation proving accuracy of the proposed numerical scheme (numerical and analytical solutions are superposed).

The best choice for the frictional Uzawa coefficient, r_f, was found to be $r_f = \dfrac{1}{\sqrt{G\rho}}$. For this choice of r_f the convergence is rapid at a tolerance around 10^{-5}. If the tolerance is larger than 10^{-4} spurious oscillations could appear. For tolerance smaller that 10^{-5} the computational time increases without any significant decrease of the error.

To study the convergence of the method with respect to the time step we have done several tests with different CFL. Although for contact problems we need a CFL=0.1 to have convergence, the frictional algorithm we need a much lower CFL=0.01. For higher values, we found that the algorithm is not convergent.

Secondly, we analyzed the mesh dependency of the numerical error. We considered three meshes $h, 1.6h$ and $0.6h$, with h having 9 nodes over the fault. We plotted the time evolution of the error in figure 12.11. As we can observe, there is an improvement for the finer mesh around 20%. We also plot in Figure 12.12 the time evolution of $\tau = \sigma_{xy}$ with respect to the

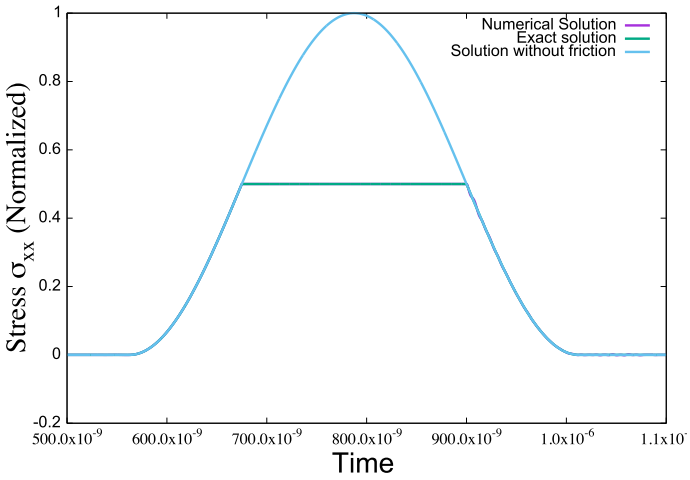

Figure 12.10: The time evolution of the normalized analytical shear stress (violet) versus the computed stress (blue) together with the loading pulse (analytical stress without friction, green) on the frictional interface Σ.

same three meshes. As before, we observe an improvement in the numerical solution with regard a mesh refinement. Though we do not analyze the convergence rate, we observe the convergence of the method with respect to the mesh size. Only small spurious oscillations are present in the frot of the wave.

12.4 Conclusions

We developed here a numerical scheme for the wave propagation in cracked solid. The internal boundary is a set of numerous cracks exhibiting nonlinear boundary conditions (unilateral contact and friction). For the time discretization is we have chosen the explicit leapfrog scheme in time while for the spatial discretization DG method was used. Since the "internal" discontinuities are already included in a DG formulation, the DG method is suitable for this kind of problems, involving numerous (micro) cracks. The switch between an edge lying on the crack and an edge lying on an internal finite element is done very simply by the flux choice. The centered flux scheme was chosen for the inner element faces while the flux on the cracks is the solution of nonlinear equations. To solve the non-linear equations associated to the non-penetration condition two techniques were used: the penalty method (based on the compliance approximation) and the Uzawa (Lagrangian) method. Even if both give accurate results, the Uzawa scheme is more accurate but it requires a higher

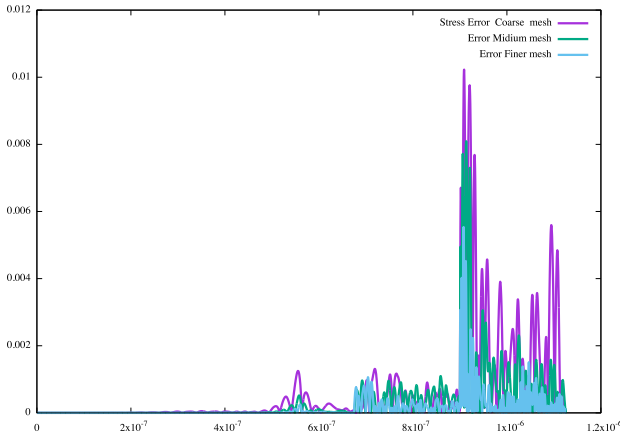

Figure 12.11: Evolution of the stress error for 3 meshes. Coarse mesh in violet, Medium Mesh in green and Finer Mesh in blue

computational cost. For low or medium accuracy the compliance method seems to be more convenient than the Uzawa method due to it is a good compromise between accuracy and computational cost. If a high accuracy is required, the compliance method it is not anymore attractive with respect to the Uzawa method. To solve the non-linear equations associated to friction an (augmented) Lagrangian algorithm is proposed. It exhibits excellent results and high accuracy but it requires a more important computational effort.

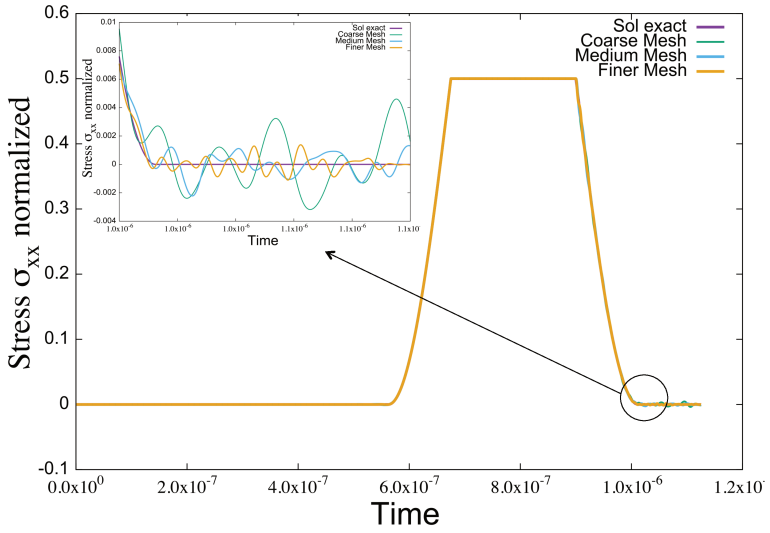

Figure 12.12: The time evolution of the normalized analytical shear stress (purple) versus the computed stress for three meshes: coarse mesh in green, medium mesh in blue and fine mesh in yellow. Zoom of the wave front.

CHAPTER 13

EFFECTIVE WAVE VELOCITY IN A CRACKED MATERIAL

The aim of this chapter is to use the discontinuous Galerkin (DG) method to find the effective properties of the damaged material via a *numerical upscaling homogenization* technique. We focus on the wave propagation (speed, amplitude, wavelength, etc.) in an isotropic cracked material to analyze how a loading pulse is affected by the presence of micro-cracks.

In the classical finite element technique an inner boundary condition requires a geometrical treatment; hence the computational effort became very important for a large number of micro-cracks. In contrast, in the DG method, the inner boundary conditions are modeled by the flux choice (see the previous section) without additional computational costs even for many micro-cracks.

13.1 Heterogeneous Problem

We consider the deformation of an elastic material occupying a bounded domain $\mathcal{D} \subset \mathbb{R}^3$, which is the union of cube cell $\mathcal{C}_j$, such that $\mathcal{C}_j \cap \mathcal{C}_k = \emptyset$ for $j \neq k$. $\mathcal{C}_j$ contains N types of circular micro-cracks of radius l_i oriented through the normals $\boldsymbol{n}_i, i = 1, \ldots, N$ (see figure 13.1). The union of all micro-cracks (internal boundary) will be denoted by Σ while the external boundary $\partial\bar{\mathcal{D}}$ of $\mathcal{D}$ will be supposed to be smooth and divided in two disjoint parts:

Σ_σ, Σ_v. We suppose that the material is isotropic, hence (11.2) becames

$$\boldsymbol{\varepsilon} = \boldsymbol{\varepsilon}(\boldsymbol{u}) = \frac{1+\nu_0}{E_0}\boldsymbol{\sigma} - \frac{\nu_0'}{E_0} tr(\boldsymbol{\sigma}) I \text{ in } \Omega. \tag{13.1}$$

where E_0 the Young's modulus and ν_0 the poisson's ratio of the undamaged material.

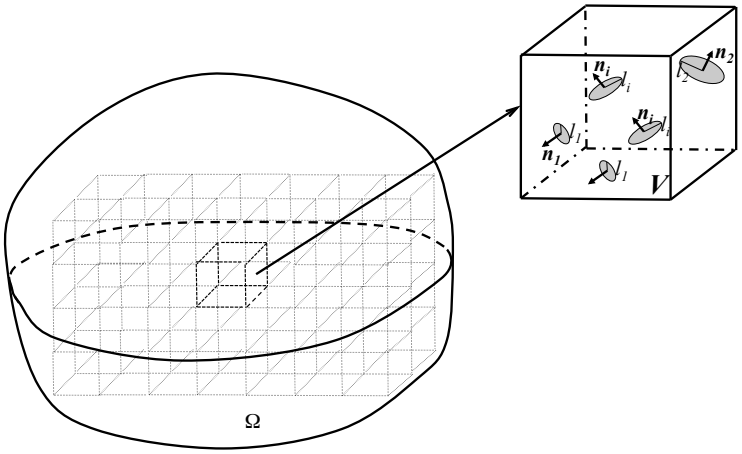

Figure 13.1: Representation of the domain Ω, its cells and zoom in a representative cell $\mathcal{C}_k$. $\mathcal{C}_k$ contains N types of circular micro-cracks of radius l_i oriented through the normals $\boldsymbol{n}_i, i = 1, \ldots, N$.

The wave propagation in the heterogeneous domain $\mathcal{D}$ consists in finding the displacement field $\boldsymbol{u} : [0,T] \times \mathcal{D} \to \mathbb{R}^3$ (or equivalently the velocity $\boldsymbol{v} = \dot{\boldsymbol{u}} : [0,T] \times \mathcal{D} \to \mathbb{R}^3$) and the stress field $\boldsymbol{\sigma} : [0,T] \times \mathcal{D} \to \mathbb{R}^{3\times 3}_S$, solution of (11.1)-(11.3) with the external boundary conditions (11.5), the nonlinear internal boundary conditions (11.6)-(11.8) (or (11.9) instead of (11.7)) and the initial conditions (11.12).

To simplify the general problem, we focus in the next section on the plane stress configuration, where $\mathcal{D} = \Omega \times (-h, h)$ and $\sigma_{xz} = \sigma_{yz} = \sigma_{zz} \equiv 0$.

13.1.1 Uniaxial Loading in Plane Stress

In order to construct a problem which has an analytical solution in the absence of the heterogeneities, we consider the wave propagation in a rectangular domain $\Omega^e = (0, L) \times (0, 2b)$ under a stress loading. More precisely, we suppose that the faces $y = -b$ and $y = b$ are in bilateral contact without friction with two rigid parallel plates (shear stress and normal

displacement are zero):

$$\boldsymbol{\sigma}_T(t) = 0, \quad \boldsymbol{u}(t) \cdot \boldsymbol{n} = 0, \quad \text{on } y = \pm b,$$

while the face $x = L$ is fixed (the displacement is zero) and on the face $x = 0$ we impose a traction pulse:

$$\boldsymbol{u}(t) = 0 \quad \text{on } x = L, \qquad \boldsymbol{\sigma n} = -S(t)\boldsymbol{e}_x \quad \text{on } x = 0$$

where $S(t) = B\varphi_\delta(t - \delta)$, with $B > 0$ the amplitude and 2δ the time length of the pulse ($\varphi_\delta(s) = \dfrac{cos(s\pi/\delta) + 1}{2}$ if $|s| \leqslant \delta$, and $\varphi_\delta(s) = 0$ elsewhere). The initial state is at rest in an unstressed configuration.

$$\boldsymbol{v}_0 = 0, \quad \boldsymbol{\sigma}_0 = 0.$$

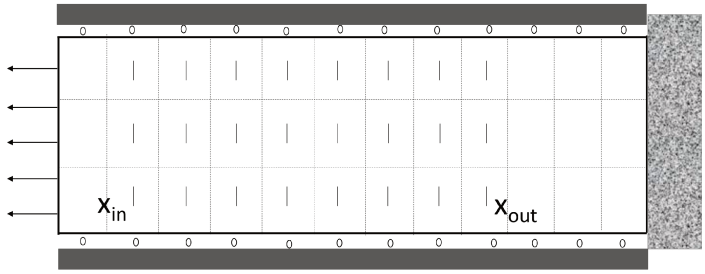

Figure 13.2: Representation of the domain Ω with parallel cracks vertically oriented.

Observe that if the material is not damaged ($\Sigma = \emptyset$), the exact solution in an one dimensional plane wave

$$\sigma^0_{xx}(t, x) = S(t - \frac{x}{c_0}), \quad v^0_x(t, x) = -\frac{S(t - \frac{x}{c_0})}{\rho^{mass} c_0}, \tag{13.2}$$

traveling with the non-damaged wave velocity:

$$c_0 = \sqrt{\frac{E_0}{\rho^{mass}(1 - \nu_0^2)}}. \tag{13.3}$$

In this subsection we consider only one family of micro-cracks, oriented following the normal $\boldsymbol{n} = (n_x, n_y)$. Since these micro-cracks will be solicited principally in mode I, we will neglect frictional effects and consider only frictionless contact boundaries conditions. At initial state the specimen is at rest ($\boldsymbol{v}_0 = 0$) and no initial pre-stresses are present ($\boldsymbol{\sigma}_0 = 0$).

13.1.2 Phenomenon description

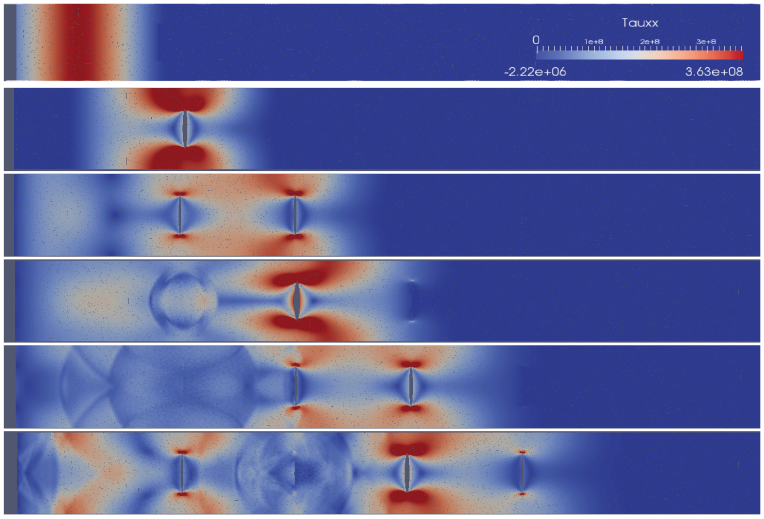

Figure 13.3: Propagation of an uniaxial traction pulse in a damaged zone with the σ_{xx} in color scale.

The figure 13.3 shows, from the top to the bottom, the propagation of the loading wave in a damaged zone. First, we focus on a geometry as presented in figure 13.2, where each crack is centered in a cell. For this configuration we plotted in figure 13.3 six snapshots of the uniaxial traction pulse propagation with σ_{xx} in color scale. Note that, the propagation of an uniaxial traction pulse is associated with a complex phenomenon. In the first snapshot, we plot the traction pulse before reaching the damaged zone. After reaching the first micro-crack, the stress field loses its homogeneity. We remark unloading zones around the micro cracks and high stress concentration on the crack tips. Moreover we note the presence of compressive waves that propagate in the opposite direction. We observe that when the pulse propagates in the domain, a scattering process is present near the micro cracks but the traction pulse still has an over-all front wave at each moment.

To analyze the micro-cracks interaction, we have zoomed in figure 13.4 the traction pulse of the figure 13.3 to a zone with two cracks. We observe how a traction pulse interacts with the micro cracks generating waves that propagates between the micro-cracks. When the traction pulse arrives near a crack, and it opens it (first snapshot), a high stress concentration at the crack tips is generated (σ_{xx} at the tips is larger than the pulse amplitude). When the first crack is closing, due to inertial effects, the unloading zone around the crack is followed by a compression wave that starts to grow around the first crack boundary (second and third

snapshots). In the same time, the pulse opens the second crack and the above scenario is repeated: the second crack closes with a compressive wave propagating is both directions (forth and fifth snapshots). At the end (sixth snapshots) we remark that the interaction between the micro-cracks continues a long period of time after the path of the main traction pulse.

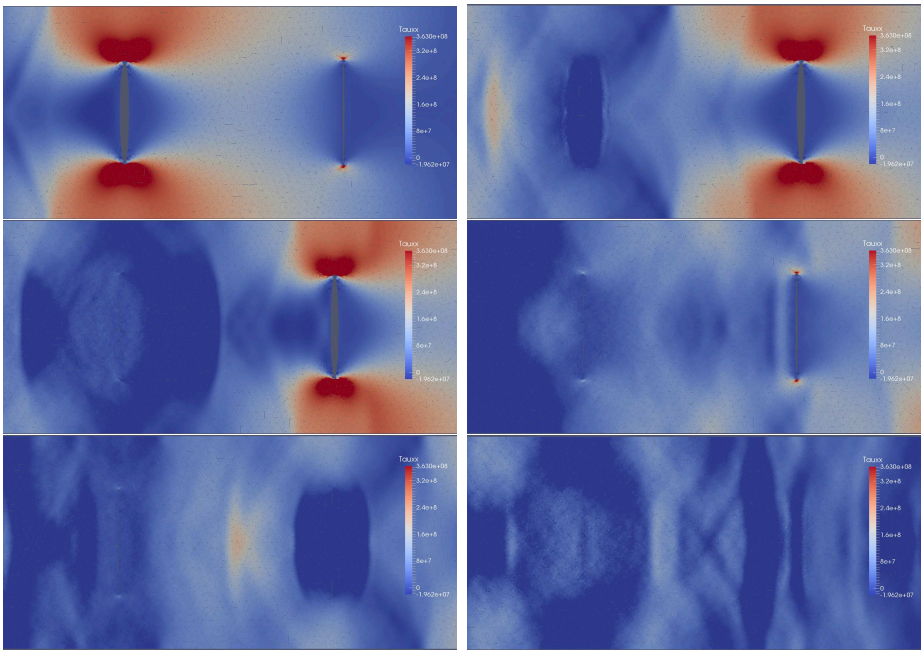

Figure 13.4: Propagation of an uniaxial traction pulse with σ_{xx} in color scale. Zoom of the figure 13.3 to a zone with two cracks.

The phenomenon becomes more complex when the micro cracks are closer. To observe it we have considered a new geometry consisting of four vertical cracks with one centered large crack, followed by two smaller aligned cracks and another large centered crack. In figure 13.5 we present six snapshots with the spatial distribution of σ_{xx} in color scale. In the first snapshot, the pulse arrives to the first crack and starts to open it. Then (second snapshot) the traction pulse opens the second crack-line generating a large stress intensity at the crack tips. The upper tip at the top crack and the bottom tip of the lower crack presents a higher stress concentration compared with the middle tips (third and forth snapshots). Later, the first crack closes generating a compression wave that propagates to the left (fifth and sixth snapshots) long time after the evacuation of main traction wave.

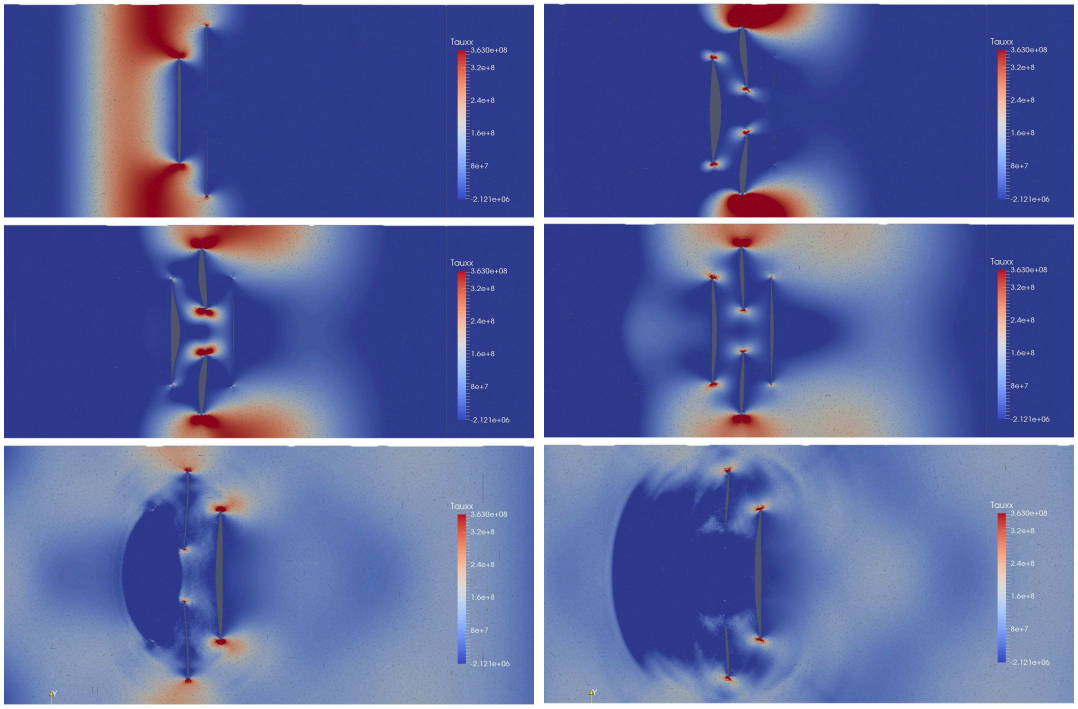

Figure 13.5: Propagation of an uniaxial traction pulse in a damaged zone (second crack distribution) with σ_{xx} in color scale.

13.2 Equivalent Problem

The equivalent problem consists in finding an *equivalent* (homogeneous) material able to describe the presence of micro-cracks on an *undamaged* (homogeneous, equivalent) elastic domain $\mathcal{D}^e = \mathcal{D} \cup \Sigma$ which does not have any micro-cracks. In order to achive this goal, we consider here the *homogenous* problem for an *anisotropic* elastic material

$$\boldsymbol{\varepsilon}^e = \mathcal{A}^e \boldsymbol{\sigma}^e \quad \text{in} \quad \mathcal{D}^e, \tag{13.4}$$

where $\mathcal{A}^e$ is the compliance tensor of the effective material. The equivalent wave propagation in the heterogeneous domain $\mathcal{D}^e$ consists in finding the displacement field $\boldsymbol{u}^e : [0,T] \times \mathcal{D}^e \to \mathbb{R}^3$ (or equivalently the velocity $\boldsymbol{v}^e = \dot{\boldsymbol{u}}^e : [0,T] \times \mathcal{D}^e \to \mathbb{R}^3$) and the stress field $\boldsymbol{\sigma}^e : [0,T] \times \mathcal{D}^e \to \mathbb{R}^{3\times 3}_S$, solution of (11.1), (13.4), (11.3) in $\mathcal{D}^e$ with the boundary conditions (11.5) and the initial conditions (11.12).

As for heterogeneous problem, we focus in the next section on the plane stress configuration, where $\mathcal{D}^e = \Omega^e \times (-h, h)$, and $\sigma^e_{xz} = \sigma^e_{yz} = \sigma^e_{zz} \equiv 0$.

13.2.1 Uniaxial loading in one dimensional propagation

In order to make a comparison with the heterogeneous problem, we consider the wave propagation in the same rectangular domain $\Omega^e = (0, L) \times (-b, b)$, under the same boundary conditions and under the same stress loading, but for an equivalent material. Due to the symmetry of our problem we will suppose that the equivalent material is orthotropic (two plane symmetries), i.e. the strain-stress relation for the plane stress configuration is reduced to

$$\begin{pmatrix} \varepsilon^e_{xx} \\ \varepsilon^e_{yy} \\ \varepsilon^e_{xy} \end{pmatrix} = \begin{pmatrix} \frac{1}{E_1} & -\frac{\nu_{12}}{E_1} & 0 \\ \frac{-\nu_{21}}{E_2} & \frac{1}{E_2} & 0 \\ 0 & 0 & \frac{1}{G_{12}} \end{pmatrix} \begin{pmatrix} \sigma^e_{xx} \\ \sigma^e_{yy} \\ \sigma^e_{xy} \end{pmatrix}, \tag{13.5}$$

where E_1, E_2 are the anisotropic Young modulus, ν_{21} and ν_{12} are the anisotropic Poisson coefficients, while G_{12} is the shear modulus. Under uniaxial loading, the presence of cracks does not cause any additional lateral strain (see [69]), hence we can suppose in the following that:

$$\frac{\nu_{12}}{E_1} = \frac{\nu_{21}}{E_2} = \frac{\nu_0}{E_0}. \tag{13.6}$$

Therefore, we are looking for a plane wave in the x-direction, such that:

$$u^e_x = u^e_x(t, x),\ u^e_y = 0 \text{ and } \sigma^e_{xy} = 0,$$

which is compatible with the boundary conditions. Hence, $\varepsilon^e_{yy} = 0$, and by replacing in (13.5), we get $\sigma^e_{yy} = \nu_{21}\sigma^e_{xx}$ and the following non-vanishing stress-strain relation yields

$$\sigma^e_{xx} = \frac{E_1}{1 - \nu_{12}\nu_{21}} \frac{\partial u^e_x}{\partial x}. \tag{13.7}$$

Let us compute the equivalent plane wave speed

$$c^e = \sqrt{\frac{E_1}{\rho^{mass}(1 - \nu_{12}\nu_{21})}},$$

which can be normalized with respect to the initial wave speed c_0

$$\frac{c^e}{c_0} = \sqrt{\frac{E_1}{E_0}\frac{1-\nu_0^2}{1-\nu_{12}\nu_{21}}} = \sqrt{\frac{1-\nu_0^2}{E_0/E_1 - \nu_0^2 E_2/E_0}}. \tag{13.8}$$

Therefore, the equivalent plane wave is given by

$$\sigma^e_{xx}(t,x) = S(t-\frac{x}{c^e}), \quad v^e_x(t,x) = -\frac{S(t-x/c^e)}{\rho^{mass}c^e}. \tag{13.9}$$

13.2.2 Micro-cracks orthogonal to the loading direction

When the cracks are oriented orthogonal to the loading direction (i.e. $\boldsymbol{n} = (1,0,0)$) they do not affect the wave propagation in the y-direction ($E_2 = E_0$) and the expression of the normalized speed wave depends only on the ratio E_1/E_0:

$$\frac{c^e}{c_0} = \sqrt{\frac{1-\nu_0^2}{E_0/E_1 - \nu_0^2}}. \tag{13.10}$$

Following the formulae given in the Appendix section 15.2 the expression of the normalized speed wave for the non-interacting cracks (NIC) scheme is

$$\frac{c^e_K}{c_0} = \sqrt{\frac{1-\nu_0^2}{1-\nu_0+2\pi\rho}}$$

while for the differential scheme (DS) we get

$$\frac{c^e_{DS}}{c_0} = \sqrt{\frac{1-\nu_0^2}{\exp(2\pi\rho)-\nu_0^2}}.$$

For the self consistent scheme (SCS) we cannot find an analytical expression of the normalized speed wave, but we can compute it numerically from the expressions of E_1 and G_{12}.

13.2.3 Micro-cracks with a miss-orientation

In order to study the influence of the micro-cracks orientation in the propagation of a plane wave we have considered a configuration with parallel micro-cracks which have a miss-fit with respect to the loading wave direction. We have denoted by $\boldsymbol{n} = (n_x, n_y, 0)$ the normal to the

cracks and we have considered only the non interacting cracks scheme (NIC). Following [69], one can compute the expressions of E_1 and E_2 and from (13.8) get the normalized speed wave in the loading direction

$$\frac{c_K^e}{c_0} = \sqrt{\frac{(1+2\pi\rho n_y^2)(1-\nu_0^2)}{(1+2\pi\rho n_x^2)(1+2\pi\rho n_y^2)-\nu_0^2}}. \tag{13.11}$$

13.3 Computed effective waves velocities

In this section we shall compare the effective wave velocity in a damaged material obtained by direct DG computation and by the analytical formula deduced form the effective elasticity of a cracked solid theory (non-interacting cracks (NIC), differential scheme (DS) and self consistent (SC) schemes). We have considered the plane-stress configuration on the domain $\Omega^e = [0, L] \times [0, 2b]$, where L is the characteristic (macro-scale) length, fixed for all numerical tests. For a simple evaluation of the speed wave, Ω^e contains a damaged zone, denoted by $\Omega^D = (x_{in}, x_{out}) \times [0, 2b]$, which is in-between two undamaged zones. In order to compute the speed wave, we denote by $t \to \sigma^{in}(t)$ and $t \to \sigma^{out}(t)$ the average (in y) of σ_{xx} at $x = x_{in}$ and at $x = x_{out}$:

$$\sigma_{xx}^{in}(t) = \frac{1}{2b}\int_0^{2b} \sigma_{xx}(t, x_{in}, y) d\, y, \quad \sigma_{xx}^{out}(t) = \frac{1}{2b}\int_0^{2b} \sigma_{xx}(t, x_{out}, y) d\, y, \tag{13.12}$$

The effective (average) wave velocity c^N of the heterogeneous media is not always simple to define. The choice which have been done here is to compute it form the following relation

$$c^N = \frac{x_{out} - x_{in}}{T_{out} - T_{in}}, \tag{13.13}$$

where T_{in} is the time when σ^{in} reaches its maximum at x_{in}, while T_{out} is the time when σ^{out} reaches its maximum at x_{out}.

The damaged zone contains square cells of size $L_c = L/15$ and each cell contains a vertical crack of length L_f. Since cell length L_c is fixed for all the tests, we have considered five different crack length: $L_f = 3L_c/5, L_c/2, L_c/3, L_c/4$ and $L_f = L_c/8$, which correspond to the following values of crack density parameter ρ ($\rho = (0.5L_f/L_c)^2$ in our case):

$$\rho_1 = 0.09, \quad \rho_2 = 0.0625, \quad \rho_3 = 0.02778, \quad \rho_4 = 0.0156, \quad \rho_5 = 0.0039. \tag{13.14}$$

The pulse duration is denoted by $T_P = 2\delta$, while the corresponding wave length is $L_P = 2\delta c_0$.

We have chosen the material data, associated to ceramic, to be $E_0 = 300\text{GPa}$, $\nu_0 = 0.24$ and $\rho^{mass} = 3673\ \text{kg m}^{-3}$ which gives $c_0 = 9309.63m/s$. The interval of time $[0, T]$ was chosen to be $T = 1.6L/c_P$, where $c_P = \sqrt{(\lambda_0 + 2G_0)/\rho^{mass}}$ is the P-wave speed and λ_0, G_0 are the Lamé coefficients.

Our first analysis will concern micro-cracks orthogonal to the loading direction (vertical cracks, i.e. $\boldsymbol{n} = e_x$). Firstly, we will test the influence of the chosen number of verticals cells and of the mesh choice. Using the conclusions of this first analysis we have chosen a geometrical setting and a mesh to compute the speed wave for different cracks lengths and pulse durations. Then, we compared these numerical results to the effective speed wave obtained by analytical expressions of three models (schemes) in each case. Our second analysis will be focused on the micro-cracks with a miss-orientation with respect to the loading direction, and we will follow the same steps as for the case of vertical micro-cracks.

13.3.1 Geometrical and mesh sensitivity tests

We analyze here if different geometrical configurations of Ω^D produce significant differences in the numerical results of the stress average. Yo this aim, we set the crack's length to be $L_f = L_c/2$ (corresponding to a crack density parameter $\rho = 1/16$) and we chose the pulse duration to be $T_P = 2\delta = T/12$ (corresponding to a wave length $L_P = 2\delta c_0 = Tc_0/12$). We consider three different geometries with 9 horizontal cells but with one, two or three vertical cells corresponding to $9 \times 3, 9 \times 2, 9 \times 1$ cells (see figure 13.6).

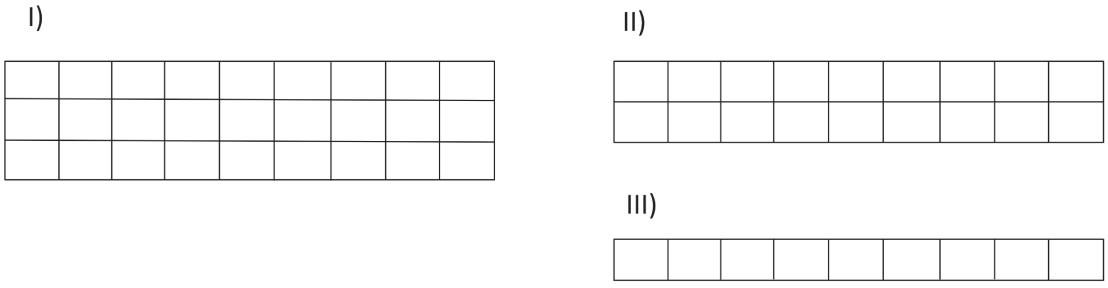

Figure 13.6: Geometrical configuration choice for Ω^D. The mesh I) represents 9×3, II) 9×2 and III) 9×1 cells.

In Figure 13.7 one can observe the evolution, in time of the averaged stress $t \to \sigma^{out}(t)$ at

$x = x_{out}$ for the three configurations and the undamaged case (purple). We remark that the pulse recorded at the end of the damaged zone is slower, has a smaller amplitude and larger duration in comparison with the loading pulse. The numerical results obtained for all the three geometrical configurations are very close. We conclude that, for this choice of crack orientation, the number of vertical cells does not influence the horizontal wave propagation and therefore, for the following tests, we consider only the third configuration.

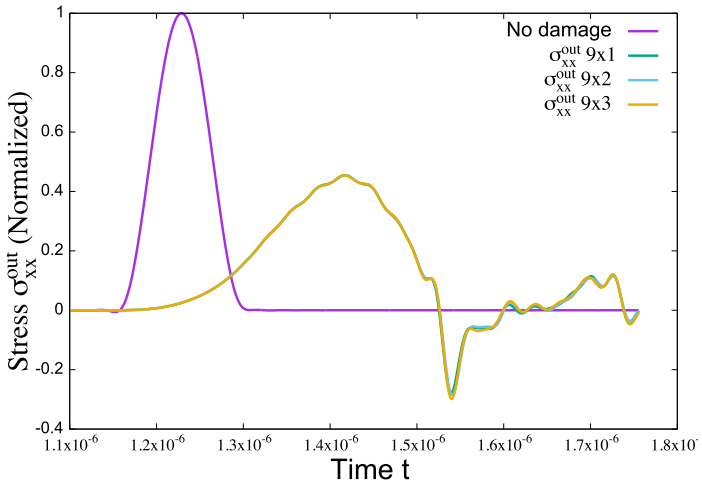

Figure 13.7: Comparison of the time evolution of the averaged stress $t \to \sigma^{out}(t)$ at $x = x_{out}$ for three configurations and the undamaged case (loading pulse).

Next, we study the mesh influence on the numerical results. For that, we consider two meshes: a coarse mesh and a fine one both with the polynomial degree $d = 2$. The coarse mesh has 773 number of vertex, 1356 number of triangles and 8100 number of degrees of freedom, while the fine mesh has 2877 number of vertex, 5364 number of triangles and 32184 number of degrees of freedom. The evolution in time of the averaged stress $t \to \sigma^{out}(t)$ at $x = x_{out}$, computed on these two meshes is shown in Figure 13.8. Since the differences are negligible in the result we have concluded that the mesh sensitivity is very small and we can trust the numerical results on the coarse mesh.

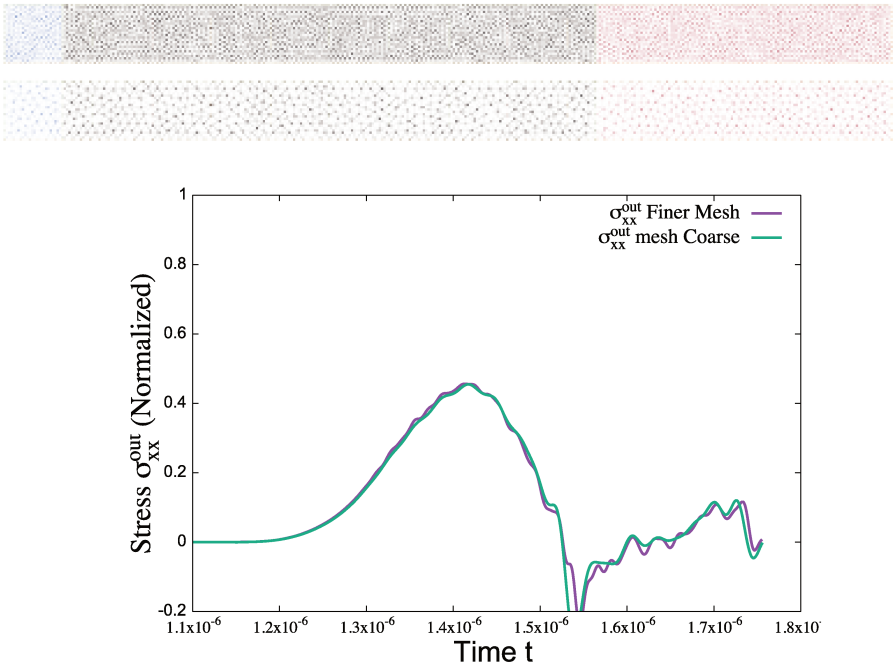

Figure 13.8: Evolution in time of the averaged stress $t \to \sigma^{out}(t)$ at $x = x_{out}$ for two different meshes: a coarse mesh (see the down plot) in green and a finer mesh (see the up plot) in purple.

13.3.2 Crack density dependence

In this section, we analyze the behavior of the outgoing pulse $\sigma^{out}(t)$ on five different geometries, corresponding to five values of the crack density parameter ρ. We also compare the speed wave obtained numerically with the speed predicted by the NIC, DS and SCS schemes. The pulse duration is fixed, as in the previous subsections, to be $T_P = 2\delta = T/12$ (corresponding to a wave length $L_P = 2\delta c_0 = Tc_0/12$).

We plotted in Figure 13.9 the time evolution of the averaged stress $t \to \sigma^{out}(t)$ for different crack density factor ρ and without damage. A general remark is that in all the cases, the pulse is slower and the amplitude is smaller for increasing crack density parameter ρ. Moreover, for $\rho > 0.02$, the pulse profile changes by losing its symmetry and for $\rho > 0.06$ there is a loss in the regularity. This is due to the fact that for large ρ, the crack length is of the same order as the wavelength and will be analyzed in detail in the next section.

In Figure 13.10 we show the normalized wave speed versus the crack density ρ. We compare the numerical results c^N/c_0, obtained with our DG numerical scheme, with three different theoretical formula given in the previous section: NIC, DS and SCS. These results

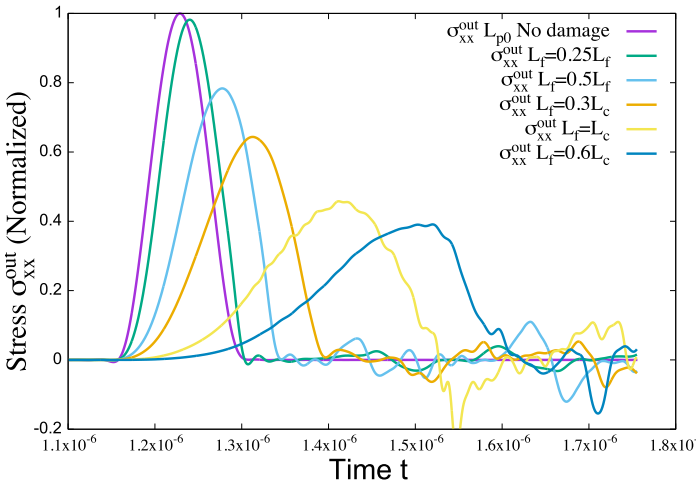

Figure 13.9: Evolution in time of the averaged stress $t \to \sigma^{out}(t)$ at $x = x_{out}$ for different crack density factors $\rho = 0.09, 0.0625, 0.02778, 0.0156, 0.0039$ and without damage (purple).

are also given in table 13.3.2. We note that, for small values of ρ ($\rho < 0.02$) the three theoretical formula and the computed speed wave are very close, but for $\rho \geqslant 0.02$ there is an important gap between them. The computed wave speed is placed between the curve given by the differential scheme (DS, top) and the self consistent scheme (SCS , bottom) and the best approximation is given by the differential scheme, followed by NIC. The bigger gap is given by the self consistent scheme, due to an under estimation of the effective Young modulus.

	$\rho_1 = 0.09$	$\rho_2 = 0.0625$	$\rho_3 = 0.02778$	$\rho_4 = 0.0156$	$\rho_5 = 0.0039$
c_K^e/c_0	0.79053	0.84016	0.91855	0.951658	0.98723
c_{DS}^e/c_0	0.74396	0.81369	0.91197	0.94947	0.98709
c_{SCS}^e/c_0	0.60291	0.71419	0.86875	0.92553	0.98124
c^N/c_0	0.70449	0.78625	0.89280	0.93323	0.98478

Table 13.1: Normalized wave speed for each crack density ρ : c_K^e/c_0 (NIC up), c_{DS}^e/c_0 (differential scheme second) , c_{SCS}^e/c_0 (self consistent scheme third) and c^N/c_0 (numerical computations bottom).

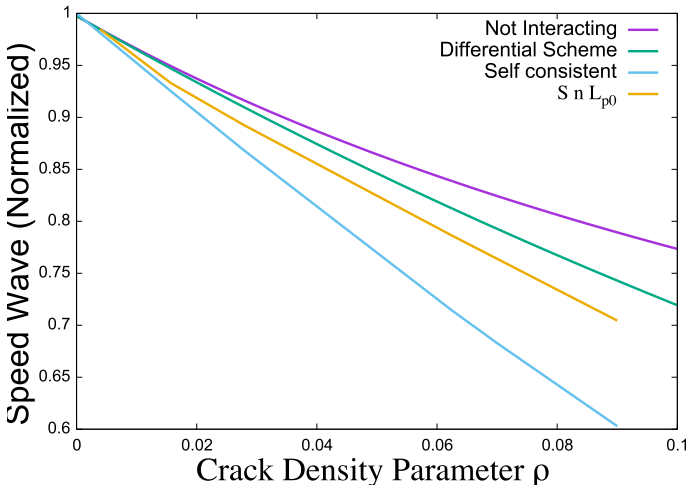

Figure 13.10: Normalized wave speed c/c_0 versus the crack density ρ: c^e_K/c_0 (NIC in magenta), c^e_{DS}/c_0 (differential scheme in green) , c^e_{SCS}/c_0 (self consistent scheme in blue) and c^N/c_0 (numerical computations in yellow).

13.3.3 Wave length influence

In this subsection we study the influence of the wave length on the wave propagation properties. In order to do so, we have made several computations using five different wave lengths, by changing each time the pulse duration 2δ. We denote the previous $\delta = T/6$ as δ_0 and we choose five different wave lengths $L_p = \dfrac{c_0\delta_0}{4}, \dfrac{c_0\delta_0}{2}, c_0\delta_0, 2c_0\delta_0, 4c_0\delta_0$. For each wave length we consider the same crack lengths as before, corresponding to the same crack densities $\rho_1, \rho_2, \rho_3, \rho_4$ and ρ_5.

	$\rho_1 = 0.09$	$\rho_2 = 0.0625$	$\rho_3 = 0.02778$	$\rho_4 = 0.0156$	$\rho_5 = 0.0039$
$L_p = c_0\delta_0/4$	0.7051	0.7823	0.8842	0.9528	0.9867
$L_p = c_0\delta_0/2$	0.7045	0.7905	0.8822	0.9421	0.9817
$L_p = c_0\delta_0$	0.7045	0.7863	0.8928	0.9332	0.9848
$L_p = 2c_0\delta_0$	0.7008	0.7709	0.8877	0.9392	0.9859
$L_p = 4c_0\delta_0$	0.7514	0.8187	0.9123	0.94551	0.9852

Table 13.2: Normalized wave speed c^N/c_0 for each crack density ρ and for five different wave lengths.

In the table 13.2, we present the normalized wave speed c^N/c_0 for each wave length and

each crack density. In the figure 13.11 we show the normalized wave speed c^N/c_0 versus the crack density ρ computed for different wave lengths and compared them with the theoretical results (NIC, DS and SCS), and c^N for each L_p considered. We remark that all the curves computed for different wave lengths are between NIC curve (upper-bound) and the SCS curve (lower-bound). For small ρ all the values for the ratio c^N/c_0 are very similar, approaching all the theoretical curves. For larger ρ there are important differences depending also on the wave length. For the largest wave length $L_P = 4c_0\delta_0$ the ρ-dependency curve is very close to the DS theoretical estimation but for smaller wave lengths the situation is different.

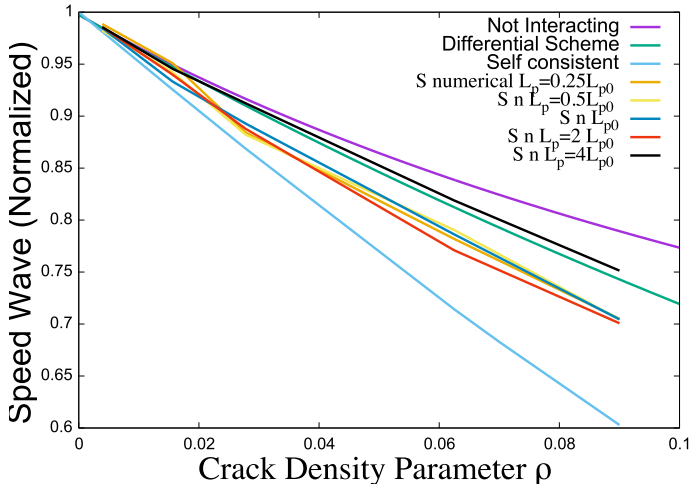

Figure 13.11: Normalized wave speed c/c_0 versus the crack density ρ: c^e_K/c_0 (NIC in magenta), c^e_{DS}/c_0 (differential scheme in green) , c^e_{SCS}/c_0 (self consistent scheme in blue) and c^N/c_0 (numerical computations) for different wave lengths $L_p = \dfrac{c_0\delta_0}{4}, \dfrac{c_0\delta_0}{2}, c_0\delta_0, 2c_0\delta_0, 4c_0\delta_0$.

In figure 13.12 we plotted the normalized wave speed c^N/c_0 versus ρ and versus the ratio between the wave length and the crack length L_p/L_f. We remark that, if the wave length L_p is of order of the crack length, the speed wave has an important variation with respect to ρ. Moreover, the speed wave is strongly dependent on wave length for $L_p/L_f \in [1, 5]$. On the other hand, for $L_p/L_f \in [5, 30]$, the speed wave c^N/c_0 depends only on ρ and for $L_p/L_f > 30$ and small crack density ρ, we recover the speed wave of the undamaged material. We conclude that, when the wave length L_p is smaller than the crack length L_f there is a

high impact in the speed wave for all ρ. This impact decreases notoriously when the wave length is at least four times the crack length. For $L_p/L_f \in [5, 30]$ we note that there is a small influence of the presence of the micro cracks in the speed wave. In the case that $L_p/L_f > 30$ we observe that the presence of micro cracks is almost negligible.

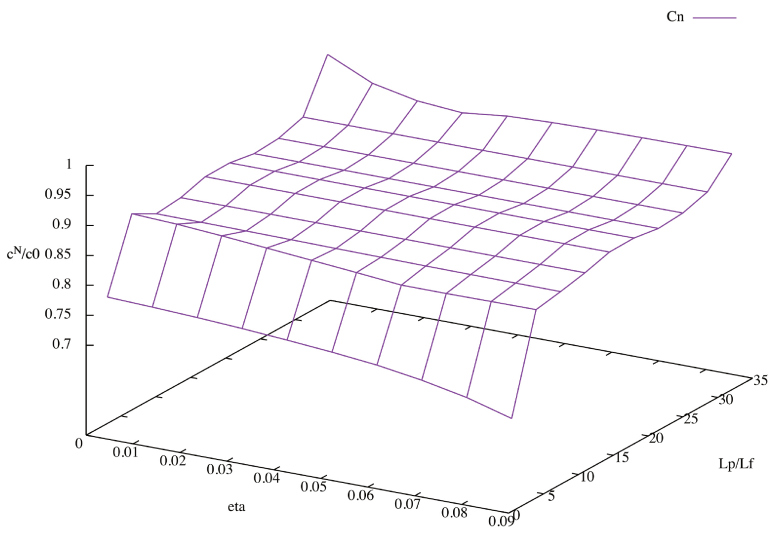

Figure 13.12: Normalized wave speed c^N/c_0 versus ρ and versus the ratio between the wave length and the crack length L_p/L_f.

Figure 13.13 shows the time evolution of the averaged stress $t \to \sigma^{out}(t)$ for different ρ and different wave lengths L_p. For the wave speed, the role played by wave length is important, but for the shape of the damaged pulse this role is crucial. Indeed, the upper left plots and the bottom right plots do not have at all the same shape and the behavior of the damaged pulse with respect to ρ is very different. For large wave length $L_p = 4L_c$, the damaged pulse is traveling slower and slower for ρ increasing, but the amplitude and the duration are not affected by the damage parameter ρ. For small L_p, the wave length is of order of the crack-length and the picture is quite different (left top). The pulse amplitude is decreasing and the pulse duration is increasing for increasing ρ.

Let us analyze now the pulse amplitude for different wave lengths and different ρ. We denote by A^N/A_0 the ratio between A^N, the amplitude obtained at the end of the damaged zone, and $A_0 = B$, the amplitude without damage. We present in Table 13.3 the variation of this ratio with respect to the wave length L_p for different ρ.

Let us analyze now the damaged wave shape with respect to ρ for each wave length L_p. For L_{p1}, most of the crack lengths considered have a bigger length than the wave length of

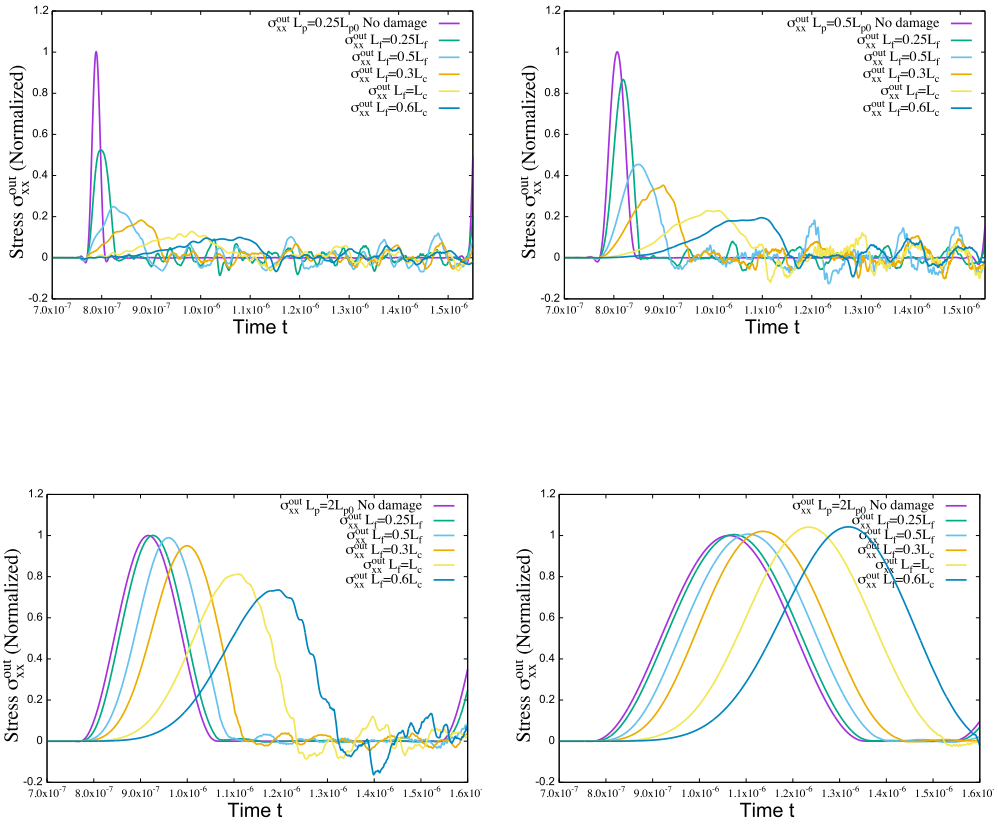

Figure 13.13: Role played by the wavelength L_p. Comparison of the time evolution of the averaged stress $t \to \sigma^{out}(t)$ for different ρ and the undamaged case (loading pulse). Up left $L_p = L_c$, up right $L_p = L_c/2$, left bottom $L_p = 2L_c$ and right bottom $L_p = 4L_c$.

	ρ_1	ρ_2	ρ_3	ρ_4	ρ_5
$L_{p1} = c_0\delta_0/4$	0.0991	0.1246	0.1824	0.2482	0.5236
$L_{p2} = c_0\delta_0/2$	0.1949	0.2287	0.3472	0.4541	0.8457
$L_{p3} = c_0\delta_0$	0.3903	0.4562	0.6439	0.7832	0.9822
$L_{p4} = c_0 2\delta_0$	0.7359	0.8109	0.9503	0.9893	1.0004
$L_{p5} = c_0 4\delta_0$	1.0423	1.0490	1.0202	1.0067	1.0046

Table 13.3: Variation of the ratio A^N/A_0 (between the amplitude of the damaged pulse A^N and the amplitude of the undamaged pulse A_0) with respect to the wave length L_p for different ρ.

L_{p1} and therefore the pulse is strongly perturbed. For ρ_1 and ρ_2, there is a extreme distortion in the shape and in the amplitude of the damaged pulse. For ρ_3 and ρ_4, the damaged pulse

gets more than four times the original time duration and there is a loss of symmetry. For ρ_5, the amplitude is around the half and the damaged pulse duration is longer. This is the only case that preserves its original shape.

For L_{p2}, the wave length is of the same order of the cracks length. For all ρ, except ρ_5, the pulse lose its symmetry. As before, when we consider ρ_1 and ρ_2 there is a big elongation of the pulse and some perturbation in the shape. For ρ_3, and ρ_4 the damaged wave duration is more than the double undamaged one. For ρ_5, the damaged pulse is a bit diminished and its duration is slightly longer.

For L_{p3}, the pulse shape is preserved for all ρ considered. For the ρ_1 to ρ_4 there is a loss in the symmetry. For ρ_1 and ρ_2 there is a loss of regularity and the damaged wave duration is longer. For ρ_3 and ρ_4 there is reduction in the amplitude and the damaged pulse duration is proportionally longer. For ρ_5, there is a small impact in the amplitude and the shape is preserved.

For L_{p4}, there is almost no impact in the profile for ρ_3 to ρ_5. For ρ_1 and ρ_2 the damaged pulse duration is longer wave length and there is a small loss of symmetry.

We conclude that the ratio L_p/L_f is a tool to estimate the role played by the wave length in the damaged pulse shape. If the ratio L_p/L_f is close to 1, there is a high loss in the amplitude, being less than the 40% of the undamaged amplitude. If the ratio L_p/L_f is around 3, there is a limited impact in the amplitude and for $L_p/L_f \geqslant 6$ an impact is barely visible, the loss is less than 10%. We also conclude, that for small L_p/L_f this parameter is crucial in the propagation of the loading pulse in a damaged zone while the damage parameter ρ plays a second role.

13.3.4 Micro-crack pattern influence

We analyze here the influence of micro cracks pattern in the wave propagation in a damaged zone. We test a new pattern, called "intercalated cracks" model. As we can see form Figure 13.3.4 in the half cells the micro-crack length is half of the entire cell's crack and therefore the value of ρ is preserved in all cells. In Figure 13.15 we show the time evolution of the averaged stress $t \to \sigma^{out}(t)$ for the initial pattern (green) and for "intercalated cracks" model (blue) and the undamaged pulse (magenta). The crack length was chosen to be $L_f = L_c/3$. For a large wave length $L_p = 2c_0\delta_0$ (Figure 13.15 right), the damaged pulses for the two geometries are very close. There is only slight differences between the speed waves and the

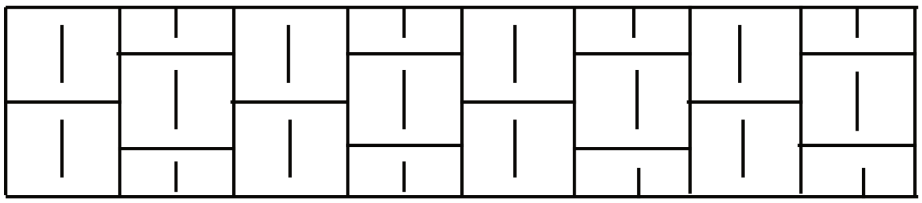

Figure 13.14: 9x2 pattern with intercalate cells with the same crack density ρ.

pulse amplitudes. More precisely, the relative gap for c^N/c_0 is of order of 0.5%, while the relative gap for A^N/A_0 is of order of 0.8%.

For small wave length $L_p =$ the damaged pulse is sharper and presents a loss in the symmetry compared with undamaged pulse. Nevertheless, the pulse where the cracks are intercalated is faster and and has higher amplitude, with a speed wave ratio $c^N/c_0 = 0.9142$ and amplitude ratio $A^N/A_0 = 0.239$. The relative gap between the pulses corresponding to these two geometries is 3.5% for the wave speed and 24% for the pulse amplitude. We have done the same numerical tests for $L_f = L_c/4$ and we remarked the same differences between the damaged pulses at small wave length.

We conclude that there is some influence of the distribution of the micro cracks in the damaged wave amplitude and a slight impact in the damaged wave velocity. However, in the cases we have investigated we haven't found a crucial influence of the micro-crack pattern in the propagation of the loading wave in a damaged region.

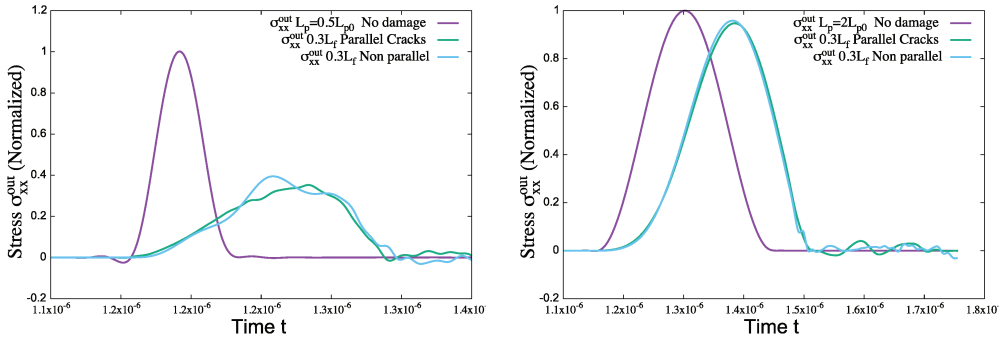

Figure 13.15: Role played by the micro cracks pattern with the same crack length $L_f = L_c/3$. The time evolution of the averaged stress $t \to \sigma^{out}(t)$ for the initial pattern (green) and for "intercalated cracks" model (blue) and the undamaged pulse (magenta). Left $L_p = L_c/2$ and right $L_p = 2L_c$.

13.3.5 Micro-cracks with a miss-orientation

We want to analyze here the role played by the miss-orientation of the micro-cracks with respect to the direction of the loading wave. To do that we have chosen the orientation of the micro-cracks to be $\theta = \pi/4$ i.e $\boldsymbol{n} = (\sqrt{2}/2, \sqrt{2}/2)$. As before, we begin by studying the geometrical and mesh dependency influences. Later, we analyze the speed wave obtained numerically and by the NIC approach. At the end, we compare the behavior of the pulse for different wave lengths.

Geometrical and mesh sensitivity analyse

First, we analyze the role played by the chosen number of vertical cells. As before, we consider three configurations: $9 \times 3, 9 \times 2$ and 9×1, with 9 horizontal cells, and $i = 1, 2$ and 3 vertical cells In figure 13.16 we have plotted the time evolution of the averaged stress pulse $t \to \sigma^{out}(t)$ for these three configurations. We note that all the stress pulses present the same delay with respect to the undamaged pulse, but the amplitudes are slightly different (the amplitude decreases when the number of vertical cell increases). These differences are much higher than the ones founded for the cracks with no miss orientation. This can be easily explained by the fact that the reflections of the incident wave on the micro-cracks are not anymore in the Ox direction and the number of vertical cells will play a more important role. Since the differences are rather small we choose the configuration 9×2 for further computations.

We continue by analyzing the mesh sensitively on the computed stress pulse by considering two meshes: the coarse mesh which has 3502 number of triangles, 1871 number of vertex and 21012 number of degrees of freedom, and the fine mesh which has 8160 number of triangles, 4261 number of vertex and 48960 number of degrees of freedom. In figure 13.17 we plotted the averaged stress $t \to \sigma^{out}(t)$ at $x = x_{out}$ computed with these two different meshes. We noticed that there are almost no differences between the two pulses and we conclude that and we can use the corse mesh in the further computations.

Crack Density and Speed Wave

We analyze here the computed outgoing pulse $\sigma^{out}(t)$ for five different geometries, corresponding to five values of the crack density parameter ρ (see (13.14)) and we will compare the speed wave obtained numerically with the speed predicted by the NIC scheme given by

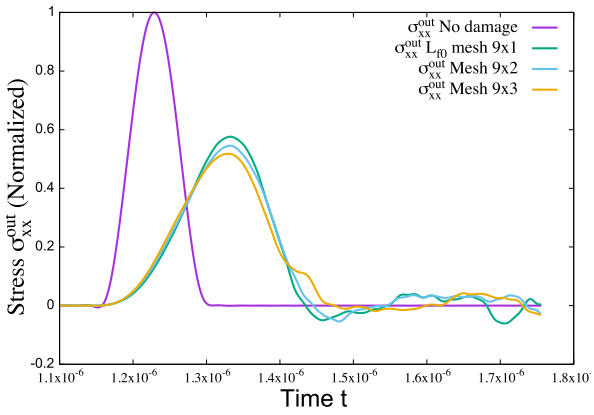

Figure 13.16: Micro-cracks with a miss-orientation. Comparison of the time evolution of the averaged stress $t \to \sigma^{out}(t)$ at $x = x_{out}$ for three configurations (9x1, 9x2 and 9x3) and the undamaged case (loading pulse).

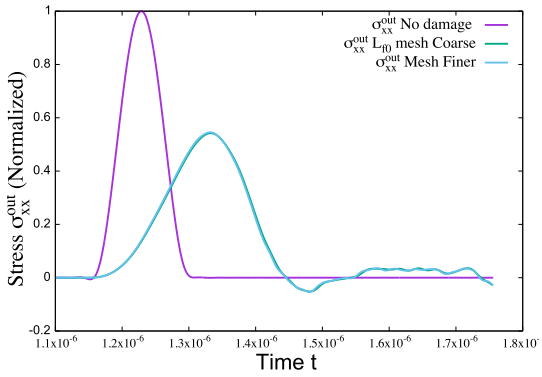

Figure 13.17: Micro-cracks with a miss-orientation. Time evolution of the averaged stress $t \to \sigma^{out}(t)$ at $x = x_{out}$ for two different meshes: a coarse mesh (in green)) and a fine mesh (in blue).

(13.11). The pulse duration will be fixed, as in the previous subsection, to be $T_P = 2\delta = T/12$ (corresponding to a the wave length $L_P = 2\delta c_0 = Tc_0/12$).

We have plotted in Figure 13.18 the time evolution of the averaged stress $t \to \sigma^{out}(t)$ for different crack density factor ρ and without damage. As for the vertical cracks the pulse is slower and the amplitude is smaller for increasing crack density parameter ρ. Moreover, for large ρ the crack length is of the same order as the wavelength and the pulse profile changes by losing its symmetry and its regularity. For small values of ρ there are not big differences in amplitude with respect the undamaged pulse but the delay of the wave is perceptible.

We present in table 13.3.5 the ratios of the wave speed in the Ox direction: c^K/c_0 given by the NIC approach (13.11) and c^N/c^0 obtained by numerical computations. As or the

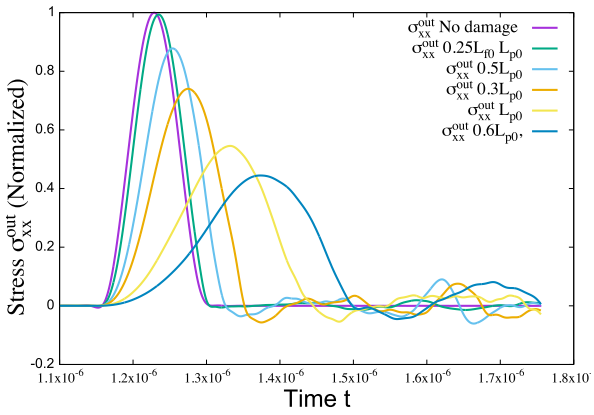

Figure 13.18: Micro-cracks with a miss-orientation. Time evolution of the averaged stress $t \to \sigma^{out}(t)$ at $x = x_{out}$ for different crack density factors $\rho = 0.09, 0.0625, 0.02778, 0.0156, 0.0039$ and without damage (purple).

	$\rho_1 = 0.09$	$\rho_2 = 0.0625$	$\rho_3 = 0.02778$	$\rho_4 = 0.0156$	$\rho_5 = 0.0039$
c^K/c_0	0.87254	0.90596	0.95455	0.97351	0.99319
c^N/c^0	0.82683	0.86977	0.93729	0.96463	0.99359

Table 13.4: Micro-cracks with a miss-orientation. Normalized wave speed for each crack density ρ : c^K/c_0 NIC scheme and c^N/c^0 numerical computations.

vertical cracks the wave speed obtained by NIC approach is larger than the computed one. However, c^K gives a better approximation than in the case with no miss-orientation, where for ρ_1, the relative gap is 5.5% and for ρ_5 the relative gap is 0.04%.

Wave length influence

To study the influence of the wave length on the wave propagation properties we will do here several computations using five different wave lengths by changing each time the pulse duration 2δ. We denote the previous $\delta = T/6$ as δ_0 and we chose five different wave lengths $L_p = \frac{c_0\delta_0}{4}, \frac{c_0\delta_0}{2}, c_0\delta_0, 2c_0\delta_0, 4c_0\delta_0$. For each wave length we have considered the same crack lengths as before, corresponding to the same crack densities $\rho_1, \rho_2, \rho_3, \rho_4$ and ρ_5.

In the table 13.3.5, we present the normalized wave speed c^N/c_0 for each wave length and each crack density and in Figure 13.19 we plotted the normalized wave speed c^N/c_0 versus the crack density ρ computed for different wave lengths and compared them with NIC theoretical results. We remark that all the computed curves for different wave lengths are under the NIC curve (upper-bound) . For small ρ all the values for the ratio c^N/c_0

	$\rho_1 = 0.09$	$\rho_2 = 0.0625$	$\rho_3 = 0.02778$	$\rho_4 = 0.0156$	$\rho_5 = 0.0039$
$L_{p1} = c_0\delta/4$	0.8316	0.8705	0.9410	0.9916	0.99553
$L_{p2} = c_0\delta/2$	0.8376	0.8712	0.9433	0.9735	0.99053
$L_{p3} = c_0\delta$	0.8259	0.8698	0.9373	0.9646	0.99219
$L_{p4} = c_0 2\delta$	0.8132	0.8646	0.9388	0.9673	0.99160
$L_{p5} = c_0 4\delta$	0.8460	0.8924	0.9493	0.9707	0.99231

Table 13.5: Micro-cracks with a miss-orientation. Normalized wave speed c^N/c_0 for each crack density ρ and for five different wave lengths.

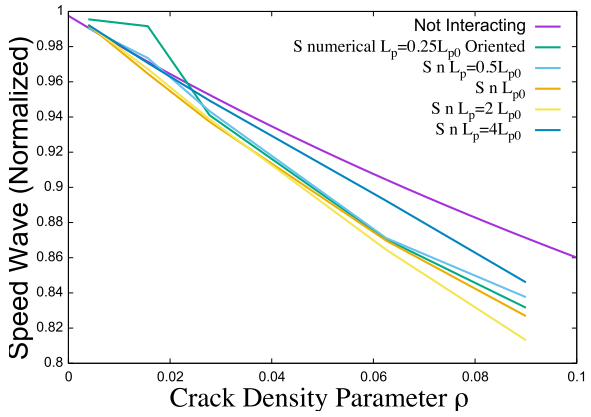

Figure 13.19: Micro-cracks with a miss-orientation. Normalized wave speed c^N/c_0 versus the crack density ρ: c^K/c_0 theoretical NIC in magenta, the numerical computations c^N/c_0 for different wave lengths $L_p = \dfrac{c_0\delta_0}{4}, \dfrac{c_0\delta_0}{2}, c_0\delta_0, 2c_0\delta_0, 4c_0\delta_0$.

are very similar, approaching all the theoretical curves while for larger ρ the are important differences.

As for vertical cracks the speed wave has an important variation with respect to ρ for wave lengths L_p of order of the crack length. Moreover, the speed wave is strongly dependent on wave length for $L_p/L_f \in [1, 5]$. We conclude that when the wave length L_p is smaller than the crack length L_f there is a high influence of the wave length on the speed wave for all ρ. This influence decreases a lot when the wave length larger that four times the crack length.

13.4 Conclusions

The proposed discontinuous Galerkin (DG) method was used find the effective properties of the damaged material via a *numerical upscaling homogenization* technique. We have analyzed how a loading pulse is affected by the presence of micro-cracks (speed, amplitude, wavelength, etc.).

The computations have been done in a plane stress configuration with frictionless cracks parallel or not to the loading direction. Only traction loading conditions have been tested.

Concerning the speed wave dependency on the micro-crack density ρ, the computed wave speed is placed between the curve given by the differential scheme (DS, upper bound) and the self consistent scheme scheme (SCS, lower bound) and the best approximation is given by the differential scheme (DS), followed by NIC scheme.

To see the role played by the wave length in the damaged pulse shape we have used the ratio L_p/L_f, between the the wave length L_p and the crack length L_f. If the ratio L_p/L_f is close to 1, there is a high loss in the amplitude, being less than the 40% of the undamaged amplitude. If the ratio L_p/L_f is around 3, there is a limited impact in the amplitude and for $L_p/L_f \geqslant 6$ an impact is barely visible, the loss is less than 10%.

We have analyzed also the role played by the micro-crack pattern. However, In the cases we have investigated we haven't found a crucial influence of the micro-crack pattern in the propagation of the loading wave in a damaged region.

CHAPTER 14

BLAST IMPACT ON A CRACKED MATERIAL

The aim of this chapter is to illustrate how the DG method can be used to investigate more complex wave propagation phenomena. To aim this, we consider a (compressive) blast-wave propagation in a ceramic block with an anisotropic crack distribution. Finally, we will compare the numerical results obtained for a cracked material, to the ones obtained from a micro-mechanics damage model (see first part).

The elastic domain $\Omega = (0, a) \times (0, 5a)$, in a stress plane configuration, is impacted at the left side $x = 0, y \in (2a, 3a)$ by a compressive pulse $t \to S(t)$ with an amplitude $-B$ and a time duration $2\delta = 0.5a/c_P$ (see Figure 14.1). The faces $y = 0$ and $y = 5a$ are fixed and the face $x = a$ is stress free. The numerical computations are over the interval $[0, T]$ with $T = 2a/c_p$ in a domain containing M micro-cracks inclined at the angle θ. The loading compressive wave is traveling into the cracked material till it reaches the stress free boundary, when it will be reflected as traction loading wave. We will consider two cases corresponding to frictionless and frictional contact on the micro-cracks.

14.1 Micro-cracks with frictionless contact

For our first numerical simulation consider $M = 72$ vertically oriented ($\theta = \pi/2$) micro-cracks. In Figure 14.2 we show the comparison between the propagation of the blast wave in a cracked material and an undamaged one with the stress deviator in the color scale. In the first frame, at $t = 0.5T$ we can observe the instance before the pulse reaches the boundary.

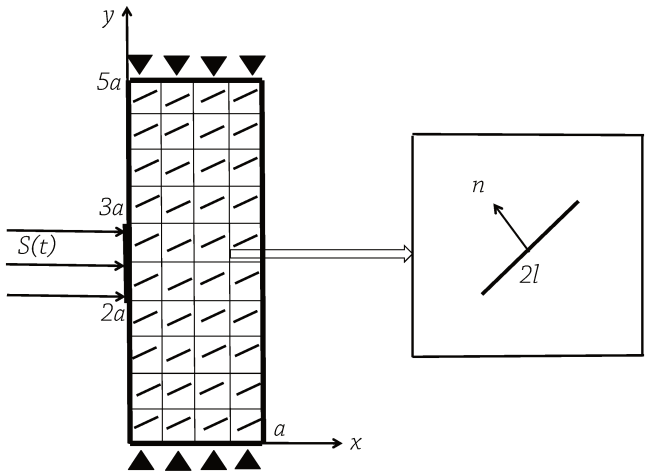

Figure 14.1: Schematic representation of the blast impact on a cracked solid.

We observe a high concentration of the stress in the middle of the pulse which is propagating as a P-wave. The micro-cracks are not opening and the P-wave is not really affected by the presence of the micro-cracks. At the tips of the impact zone, we remark two S-waves acting in mode II. In the following frames, at $t = 0.7T$ and $t = 0.8T$, just after the pulse is reflected by the stress boundary, we remark that the micro-cracks are opening generating stress concentration at the tips of the cracks, giving an irregular shape to the wave. The S-waves are perturbed, but an overall behavior can be observed. In the following frame, at $t = 0.9T$, we remark that the cracks near the right boundary begin to close. In all frames, we observe that the S-waves are not too scattered.

The same phenomenon is studied for $M = 76$ micro-cracks horizontally oriented ($\theta = 0$). In figure 14.3 one can see the blast wave propagation in a cracked block together with the undamaged case. In the first frame, at $t = 0.5T$ the S-waves are almost completely scattered but the P-wave is well represented. This is due to the fact that the horizontal micro-cracks are active in the shearing process (Mode II) but almost inactive in Mode I. At $t = 0.7T$ we found that the micro-cracks near the right boundary are opening, giving a high concentration of the the deviatoric stress but the P-wave are not as affected as in the vertical case. However, the overall shape of the wave is preserved. In the last two frames we remark that the loading wave is less scattered than in the previous case (vertical orientation), but in all frames we observe an important scattering of the S-waves.

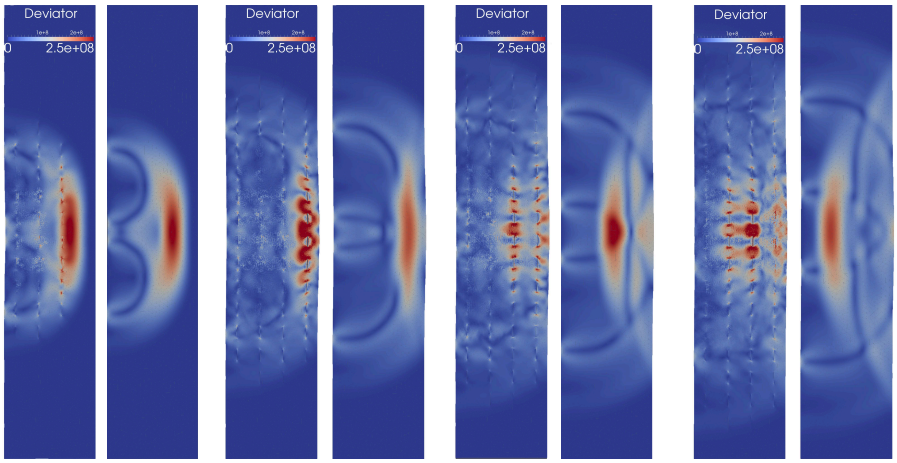

Figure 14.2: Vertical micro-cracks. Comparison between the propagation of the blast wave in a cracked material (left) and an undamaged one (right). Four snapshots of the stress deviator (color scale in Pa) at $t = 0.5T, 0.7T, 0.8T$ and $t = 0.9T$.

The third numerical simulation concerns micro-cracks oriented at $\theta = \pi/4$. We notice in the first frame of Figure 14.4 that the P-Wave is already perturbed due to cracks acting in mode II. After the reflection ($t = 0.7T$) we observe that more right cracks begin to open. In the last two frames the cracks are active in mode I and II and it is difficult to distinguish an overall behavior of the resulting scattered wave.

14.2 Micro-cracks with frictional contact

Since in the previous study the nonlinear behavior was related to the (frictionless) unilateral contact, we will analyze here the role played by the friction phenomena. In this aim, we have considered the last configuration with the cracks oriented at $\theta = \pi/4$. The two sides of the cracks are in frictional unilateral contact and the friction coefficient was chosen to be $\mu_f = 0.5$. Globally, we expect the friction to have a stabilized effect and waves less perturbed by the presence of the micro-cracks. This is due to the fact that the cracks have more resistance to slip in mode II. On the contrary, the mode I activation of the micro-cracks is not affected by the friction.

In Figure 14.5 we show several frames of the propagation of the blast wave in a cracked material with friction, without friction and in an undamaged one (with the stress deviator in the color scale). The first snapshot is done at $t = 0.5T$ and we remark a lose of symmetry

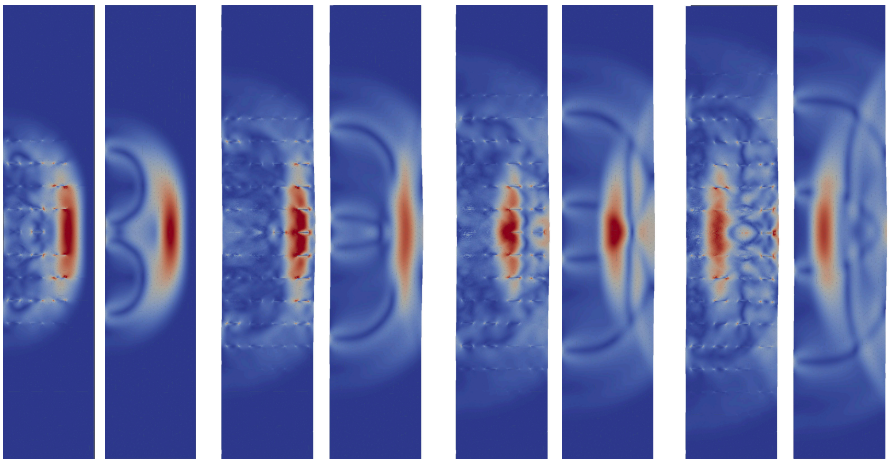

Figure 14.3: Horizontal micro-cracks. Comparison between the propagation of the blast wave in a cracked material (left) and an undamaged one (right). Four snapshots of the stress deviator (color scale in Pa) at $t = 0.5T, 0.7T, 0.8T$ and $t = 0.9T$.

in the horizontal plane. In the frictional case, the waves (P and S) are less scattered than in the frictionless case. Indeed all the micro-cracks are working in mode II at this stage, where friction imply a "damage decrease". For $t = 0.7T$, when the reflected wave is in traction we remark that in both cases the cracks next to the right boundary start to open, working in mode I. However the P-wave has a larger amplitude in the frictional case than in the other one. The other cracks are working in mode II and, as before, we remark that the S-waves are more scattered in the frictionless case. In the last two frames, we observe that in both cases the waves are spread out and it is difficult to distinguish between the frictional and frictionless propagation. This is due to the key role played by the mode I activation of the micro-cracks in the damage evolution, which affects the waves propagation.

14.3 Conclusions

In conclusion we studied the wave propagation in an anisotropic damaged material under an anisotropic loading. We pointed out that the cracks' orientation affects the wave propagation and their scattering. We illustrated the fact that the friction phenomena between the faces of the micro-cracks are affecting the wave propagation only for the mode II behavior. If the waves activate principally the mode I, the role played by the friction is negligible.

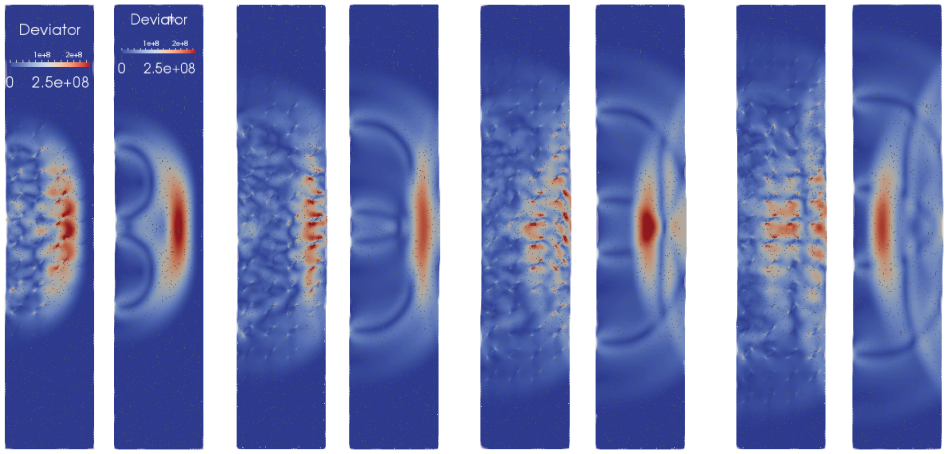

Figure 14.4: Micro-cracks oriented at $\theta = \pi/4$. Comparison between the propagation of the blast wave in a cracked material (left) and an undamaged one (right). Four snapshots of the stress deviator (color scale in Pa) at $t = 0.5T, 0.7T, 0.8T$ and $t = 0.9T$.

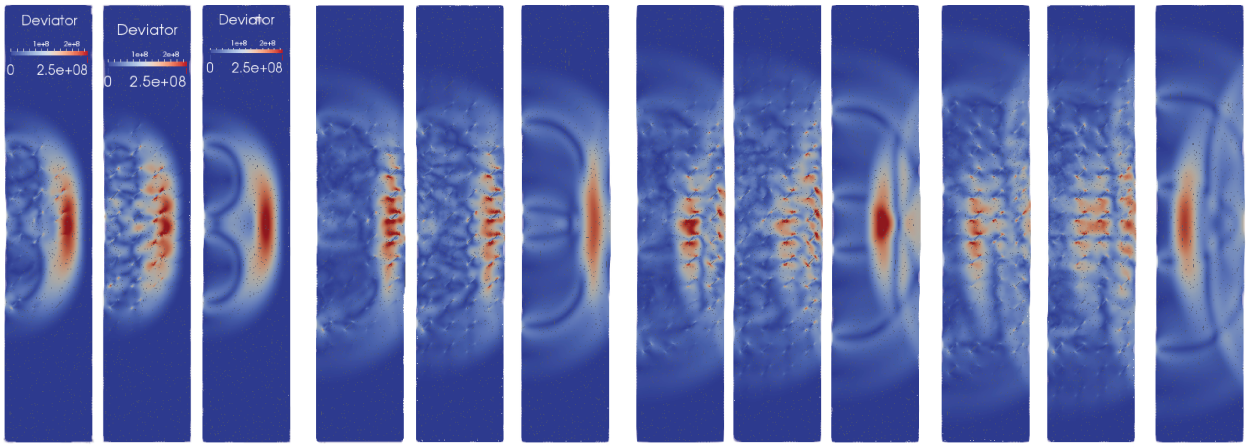

Figure 14.5: Micro-cracks oriented at $\theta = \pi/4$. Comparison between the propagation of the blast wave in a cracked material with friction (left), frictionless (middle) and an undamaged one (left). Four snapshots of the stress deviator (color scale in Pa) at $t = 0.5T, 0.7T, 0.8T$ and $t = 0.9T$.

CHAPTER 15

FINAL CONCLUSIONS AND PERSPECTIVES

The discontinuous Galerkin (DG) method is used here to investigate the dynamics of (damaged) materials with a nonlinear micro-structure (micro-cracks in frictional contact). In opposition to the classical finite element technique in the DG method the inner boundary conditions are modeled by the flux choice without additional computational costs, even for many micro-cracks.

The numerical scheme developed here makes use of the explicit leapfrog scheme in time and a centered flux choice for the inner element face. The nonlinear conditions on the micro-cracks are treated by using an augmented Lagrangian technique, with a reasonable additional computational cost.

This technique was used to compare the effective wave velocity in a damaged material obtained by direct DG computation and by the analytical formula, deduced form the effective elasticity of a cracked solid theory (NIC, DS and SCS approaches). Even if the stress field loses its homogeneity (unloading zones around the micro cracks and high stress concentration on the crack tips, compressive waves that propagates in the opposite direction, etc) the pulse has an over-all front wave at each moment. This is an important point which allowed us to compute the over-all wave speed. We found that, the over-all wave speed is slower than the theoretical speed and the difference is very important for large values of the crack density parameter. If the wave length is of order of the crack length, the speed wave is strongly dependent on wavelength, but for a large wavelength the speed wave depends only on the crack density parameter.

To illustrate the numerical scheme we have analyzed the wave generated by a blast in a cracked material (81 vertical, horizontal or inclined frictional or frictionless micro-cracks). We found that the cracks' orientation affects the wave propagation and their scattering. The friction phenomena between the faces of the micro-cracks are affecting the wave propagation only for the mode II behavior but if the waves activate principally the mode I, the role played by the friction is negligible.

For the future prospects related to the wave propagation in a cracked solid we want to mention that it will be of high interest to introduce constitutive cohesive laws on each micro-crack. The advantage of a DG approach is that the cohesive laws are very simple to be introduced as flux choices. Moreover, even the frictional contact could be introduced in a "cohesive" approach. Another possible development of the present work could be related to the 3-D development of the FreeFem++ codes.

CHAPTER 16

MODELS COMPARISON AND GENERAL CONCLUSIONS

First, we present here a comparison between the propagation of the blast wave in a "cracked solid" (see the second part of this thesis), and in a solid with a micro-mechanics based damaged model. The comparison is not natural because the two models make use of two different approaches. The micro-cracks in the "cracked material" model are introduced as a "geometric heterogeneity" in an isotropic and homogeneous elastic solid. The lengths (radius) of micro-cracks do not change (no crack growth) under the loading wave. In the micro-mechanics based damaged model the cracks are introduced through a damage parameter (crack density parameter) which could increase under the loading wave. The heterogeneity is a material one : the mechanical model looses its isotropy and its homogeneity but the geometric homogeneity is preserved. Even if we expect that the two models give very different results the comparison could be useful in understanding the role played by different assumptions in modeling damage processes.

In Figure 16.1 we have plotted four snapshots (at $t = 0.5T, 0.75T, 0.875T$ and $t = T$) for horizontal micro-cracks without friction. We note that even if there are a lot of differences between the two numerical results we have an overall similarity. The micro-mechanics based damaged model does not exhibit any S-waves scattering, present in the "cracked solid" model, but the P-waves are similarly represented in both models. Much more differences are in the case of vertical micro-cracks without friction plotted in Figure 16.2. Here the scattering of the P-wave in the cracked solid is important: the interplay of the micro-cracks is more

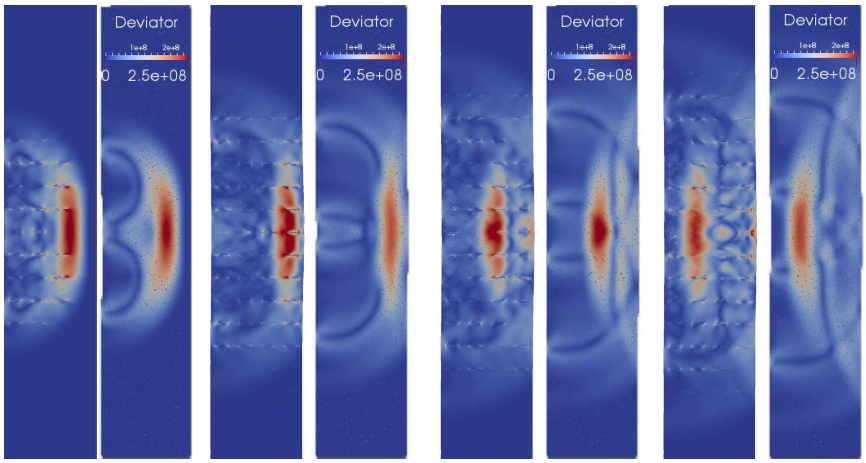

Figure 16.1: Blast wave propagation in a cracked solid (left) and in a solid with a micro-mechanics based damage model (right). Four snapshots of the stress deviator (color scale in Pa) at $t = 0.5T, 0.75T, 0.875T$ and $t = T$ for horizontal micro-cracks without friction.

present and there a lot of wave reflections between them. This fact is not captured with the a micro-mechanics based damaged model, where a non-interacting cracks' model is assumed.

In Figure 16.3 we plotted the blast wave in a "cracked solid" and in a solid with a micro-mechanics based damaged model with frictional micro-cracks oriented at $\theta = -\pi/4$. In all the frames the the blast the wave is scattered in the first model and it is not for the second. In both models we remark a lose of symmetry of the wave due to orientation the micro-cracks and due to the presence of the friction. The arrival times of the P-wave is almost the same, but the computed time period is too small to see important differences in the evaluation of the speed wave. That can also explain why the roles played the crack evolution model is not so important: the fixed crack length (cracked solid) and the micro-mechanics evolution crack-length model gives a similar overall behavior. Another explanation could be the fact that energy transfer in crack growth is not so important and the time length associated to the crack growth is very small.

We would like to point out the main characteristics of the wave propagation in a cracked solid and in a solid modeled by a micro-mechanics based damage constitutive law, what they have in common and what differentiate them. We have putted several features of the two models in the table 16.1 and we can see that they are rather complimentary. Indeed, the micro-mechanics based damage models seems to be more versatile but they require much more calibration (experimental or a micro-mechanics analysis). The cracked solid model

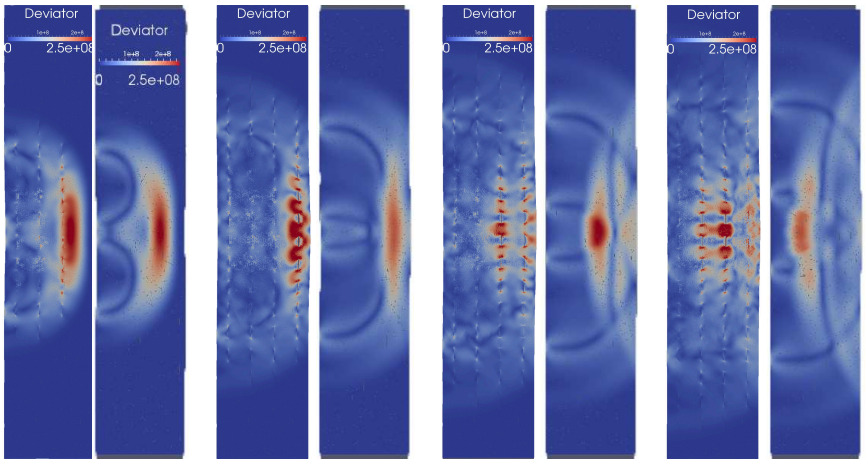

Figure 16.2: Blast wave propagation in a cracked solid (left) and in a solid with a micro-mechanics based damage model (right). Four snapshots of the stress deviator (color scale in Pa) at $t = 0.5T, 0.75T, 0.875T$ and $t = T$ for vertical micro-cracks without friction.

has a simple material description but it needs a complex geometrical implementation. The micro-mechanics based damage models are accurate in modeling the strain rate sensitivity of the material strength, while the cracked solid exhibits a wave length sensitivity. Even if there is some connections between them (a higher strain rate could correspond to a lower wave length) the two phenomena are complementary. The cracked solid response does not depend on the stress amplitude of the loading wave but it gives a very accurate description of the dynamic interaction of the micro-cracks. Finally the micro-mechanics based damage models are (generally) unstable and they require special numerical techniques (numerical fluxes, slope limiters, regularization, etc) for solving the associated boundary value problems.

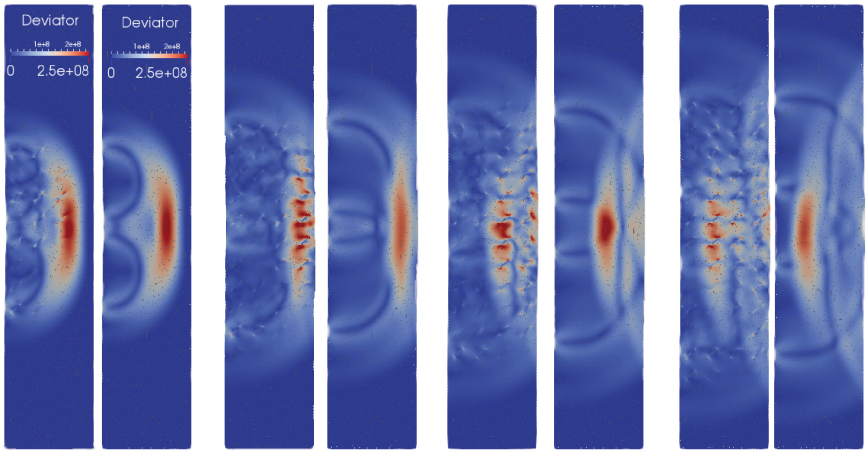

Figure 16.3: Blast wave propagation in a cracked solid (left) and in a solid with a micro-mechanics based damage model (right). Four snapshots of the stress deviator (color scale in Pa) at $t = 0.5T, 0.75T, 0.875T$ and $t = T$ for micro-cracks oriented at $\theta = -\pi/4$ with friction.

	Micro-mechanics model	cracked solid
geometric simplicity	yes	no
material modeling simplicity	no	yes
micro-cracks dynamic growth	yes	no
strain rate sensitivity	yes	no
wave length sensitivity	no	yes
stress amplitude sensitivity	yes	no
dynamic micro-cracks interaction	no	yes
stability	generally no	yes

Table 16.1: The main characteristics of the wave propagation in a cracked solid and in a micro-mechanics based damage solid.

Part III

Bibliography

BIBLIOGRAPHY

[1] S. Andrieux, Y. Bamberger, and J.-J. Marigo, *Un modèle de matériau microfissuré pour les bétons et les roches*, Journal de mécanique théorique et appliquée, 5 (1986), pp. 471–513.

[2] C. Annavarapu, M. Hautefeuille, and J. E. Dolbow, *Stable imposition of stiff constraints in explicit dynamics for embedded finite element methods*, International Journal for Numerical Methods in Engineering, 92 (2012), pp. 206–228.

[3] ——, *A nitsche stabilized finite element method for frictional sliding on embedded interfaces. part i: single interface*, Computer Methods in Applied Mechanics and Engineering, 268 (2014), pp. 417–436.

[4] D. N. Arnold, *An interior penalty finite element method with discontinuous elements*, SIAM journal on numerical analysis, 19 (1982), pp. 742–760.

[5] D. N. Arnold, F. Brezzi, B. Cockburn, and D. Marini, *Discontinuous galerkin methods for elliptic problems*, in Discontinuous Galerkin Methods, Springer, 2000, pp. 89–101.

[6] D. N. Arnold, F. Brezzi, B. Cockburn, and L. D. Marini, *Unified analysis of discontinuous galerkin methods for elliptic problems*, SIAM journal on numerical analysis, 39 (2002), pp. 1749–1779.

[7] M. Ashby and C. Sammis, *The damage mechanics of brittle solids in compression*, Pure and Applied Geophysics, 133 (1990), pp. 489–521.

[8] M. F. Ashby and S. Hallam, *The failure of brittle solids containing small cracks under compressive stress states*, Acta Metallurgica, 34 (1986), pp. 497–510.

[9] I. Babuška, *The finite element method with penalty*, Mathematics of computation, 27 (1973), pp. 221–228.

[10] I. Babuška and M. Zlámal, *Nonconforming elements in the finite element method with penalty*, SIAM Journal on Numerical Analysis, 10 (1973), pp. 863–875.

[11] G. A. Baker, *Finite element methods for elliptic equations using nonconforming elements*, Mathematics of Computation, 31 (1977), pp. 45–59.

[12] R. Bargellini, D. Halm, and A. Dragon, *Modelling of anisotropic damage by microcracks: towards a discrete approach*, Archives of Mechanics, 58 (2006), pp. 93–123.

[13] R. Bargellini, D. Halm, and A. Dragon, *Modelling of quasi-brittle behaviour: a discrete approach coupling anisotropic damage growth and frictional sliding*, European Journal of Mechanics-A/Solids, 27 (2008), pp. 564–581.

[14] F. Bassi and S. Rebay, *A high-order accurate discontinuous finite element method for the numerical solution of the compressible navier–stokes equations*, Journal of computational physics, 131 (1997), pp. 267–279.

[15] F. B. Belgacem, *The mortar finite element method with lagrange multipliers*, Numerische Mathematik, 84 (1999), pp. 173–197.

[16] F. B. Belgacem, P. Hild, and P. Laborde, *Extension of the mortar finite element method to a variational inequality modeling unilateral contact*, Mathematical Models and Methods in Applied Sciences, 9 (1999), pp. 287–303.

[17] G.-O. N. C.-A. V. BenJemaa, M. and J. Virieux, *Dynamic non-planar crack rupture by a finite volume method*, Geophys. J. Int., 171 (2007), pp. 271–285.

[18] ——, *3d dynamic rupture simulations by a finite volume method*, Geophys. J. Int., 178 (2009), pp. 541–560.

[19] M. Benjemaa, N. Glinsky-Olivier, V. M. Cruz-Atienza, and J. Virieux, *3-d dynamic rupture simulations by a finite volume method*, Geophysical Journal International, 178 (2009), pp. 541–560.

[20] H. Bhat, C. Sammis, and A. Rosakis, *The micromechanics of westerley granite at large compressive loads*, Pure and applied geophysics, 168 (2011), pp. 2181–2198.

[21] H. S. Bhat, A. J. Rosakis, and C. G. Sammis, *A micromechanics based constitutive model for brittle failure at high strain rates*, Journal of Applied Mechanics, 79 (2012), p. 031016.

[22] B. Budiansky and R. J. O'connell, *Elastic moduli of a cracked solid*, International journal of Solids and structures, 12 (1976), pp. 81–97.

[23] F. C. Carvalho and J. F. Labuz, *Experiments on effective elastic modulus of two-dimensional solids with cracks and holes*, International Journal of Solids and Structures, 33 (1996), pp. 4119–4130.

[24] P. P. Castañeda and J. R. Willis, *The effect of spatial distribution on the effective behavior of composite materials and cracked media*, Journal of the Mechanics and Physics of Solids, 43 (1995), pp. 1919–1951.

[25] D. Cereceda, L. Graham-Brady, and N. Daphalapurkar, *Modeling dynamic fragmentation of heterogeneous brittle materials*, International Journal of Impact Engineering, 99 (2017), pp. 85–101.

[26] G. Chavent and B. Cockburn, *The local projection $p^0 - p^1$-discontinuous-galerkin finite element method for scalar conservation laws*, RAIRO-Modélisation mathématique et analyse numérique, 23 (1989), pp. 565–592.

[27] B. Cockburn, G. E. Karniadakis, and C.-W. Shu, *The development of discontinuous galerkin methods*, in Discontinuous Galerkin Methods, Springer, 2000, pp. 3–50.

[28] B. Cockburn and C.-W. Shu, *The local discontinuous galerkin method for time-dependent convection-diffusion systems*, SIAM Journal on Numerical Analysis, 35 (1998), pp. 2440–2463.

[29] A. J.-P. de la Puente, J. and M. Kaser, *Dynamic rupture modeling on unstructured meshes using a discontinuous galerkin method*, J. Geophys. Res, 114 (2009), p. doi:10.1029/2008JB006271.

[30] F. L. Delcourte, S. and N. Glinsky-Olivier, *A high-order discontinuous galerkin method for the seismic wave propagation*, ESAIM: Proc., 27 (2009), pp. 70–89.

[31] S. Delcourte, L. Fezoui, and N. Glinsky-Olivier, *A high-order discontinuous galerkin method for the seismic wave propagation*, in ESAIM: Proceedings, vol. 27, EDP Sciences, 2009, pp. 70–89.

[32] H. Deng and S. Nemat-Nasser, *Dynamic damage evolution in brittle solids*, Mechanics of Materials, 14 (1992), pp. 83–103.

[33] C. Denoual and F. Hild, *A damage model for the dynamic fragmentation of brittle solids*, Computer methods in applied mechanics and engineering, 183 (2000), pp. 247–258.

[34] ——, *Dynamic fragmentation of brittle solids: a multi-scale model*, European Journal of Mechanics-A/Solids, 21 (2002), pp. 105–120.

[35] V. Deshpande and A. Evans, *Inelastic deformation and energy dissipation in ceramics: a mechanism-based constitutive model*, Journal of the Mechanics and Physics of Solids, 56 (2008), pp. 3077–3100.

[36] V. Deudé, L. Dormieux, D. Kondo, and V. Pensée, *Propriétés élastiques non linéaires d'un milieu mésofissuré*, Comptes Rendus Mécanique, 330 (2002), pp. 587–592.

[37] D. A. Di Pietro and A. Ern, *Mathematical aspects of discontinuous Galerkin methods*, vol. 69, Springer Science & Business Media, 2011.

[38] L. Dormieux, D. Kondo, and F. Ulm, *Microporomechanics*, Wiley, 2006.

[39] J. Douglas and T. Dupont, *Interior penalty procedures for elliptic and parabolic galerkin methods*, Computing methods in applied sciences, (1976), pp. 207–216.

[40] K. M. T. E. Dumbser, M., *An arbitrary high order discontinuous galerkin method for elastic waves on unstructured meshes v: local time stepping and p-adaptivity*, Geophys. J. Int., 171 (2006), pp. 695–717.

[41] M. Dumbser and M. Kaser, *An arbitrary high order discontinuous galerkin method for elastic waves on unstructured meshes ii: the three- dimensional isotropic case*, Geophys. J. Int., 167 (2006), pp. 319–336.

[42] N. El-Abbasi and K.-J. Bathe, *Stability and patch test performance of contact discretizations and a new solution algorithm*, Computers & Structures, 79 (2001), pp. 1473–1486.

[43] B. Erzar and P. Forquin, *Analysis and modelling of the cohesion strength of concrete at high strain-rates*, International Journal of Solids and Structures, 51 (2014), pp. 2559–2574.

[44] J. Eshelby, *Elastic inclusions and heterogeneities*, Progress in Solid, 2 (1961).

[45] J. D. Eshelby, *The determination of the elastic field of an ellipsoidal inclusion, and related problems*, in Proceedings of the Royal Society of London A: Mathematical, Physical and Engineering Sciences, vol. 241, The Royal Society, 1957, pp. 376–396.

[46] V. Etienne, E. Chaljub, J. Virieux, and N. Glinsky, *An hp-adaptive discontinuous galerkin finite-element method for 3-d elastic wave modelling*, Geophysical Journal International, 183 (2010), pp. 941–962.

[47] X.-Q. Feng and S.-W. Yu, *Micromechanical modelling of tensile response of elastic-brittle materials*, International Journal of Solids and Structures, 32 (1995), pp. 3359–3372.

[48] P. Forquin and F. Hild, *A probabilistic damage model of the dynamic fragmentation process in brittle materials*, Advances in applied mechanics, 44 (2010), pp. 1–72.

[49] L. Freund, *Crack propagation in an elastic solid subjected to general loading?i. constant rate of extension*, Journal of the Mechanics and Physics of Solids, 20 (1972), pp. 129–140.

[50] L. Freund, *Dynamic Fracture Mechanics*, Cambridge Monographs on Mechanics, Cambridge University Press, 1998.

[51] L. Gambarotta, *Friction-damage coupled model for brittle materials*, Engineering fracture mechanics, 71 (2004), pp. 829–836.

[52] L. Gambarotta and S. Lagomarsino, *A microcrack damage model for brittle materials*, International Journal of Solids and Structures, 30 (1993), pp. 177–198.

[53] L. Graham-Brady, *Statistical characterization of meso-scale uniaxial compressive strength in brittle materials with randomly occurring flaws*, International Journal of Solids and Structures, 47 (2010), pp. 2398–2413.

[54] R. Graves, *Simulating seismic wave propagation in 3d elastic media using staggered-grid finite differences*, Bull. seism. Soc. Am., 86 (1996), pp. 1091–1106.

[55] D. Halm and A. Dragon, *A model of anisotropic damage by mesocrack growth; unilateral effect*, International Journal of Damage Mechanics, 5 (1996), pp. 384–402.

[56] D. Halm and A. Dragon, *An anisotropic model of damage and frictional sliding for brittle materials*, European Journal of Mechanics-A/Solids, 17 (1998), pp. 439–460.

[57] P. Hansbo and M. G. Larson, *Discontinuous galerkin methods for incompressible and nearly incompressible elasticity by nitsche's method*, Computer methods in applied mechanics and engineering, 191 (2002), pp. 1895–1908.

[58] Z. Hashin, *The differential scheme and its application to cracked materials*, Journal of the Mechanics and Physics of Solids, 36 (1988), pp. 719–734.

[59] F. Hecht, *New development in freefem++*, J. Numer. Math., 20 (2012), pp. 251–265.

[60] F. Hild, C. Denoual, P. Forquin, and X. Brajer, *On the probabilistic–deterministic transition involved in a fragmentation process of brittle materials*, Computers & structures, 81 (2003), pp. 1241–1253.

[61] A. Hoenig, *Elastic moduli of a non-randomly cracked body*, International Journal of Solids and Structures, 15 (1979), pp. 137–154.

[62] H. Horii and S. Nemat-Nasser, *Overall moduli of solids with microcracks: load-induced anisotropy*, Journal of the Mechanics and Physics of Solids, 31 (1983), pp. 155–171.

[63] G. Hu, J. Liu, L. Graham-Brady, and K. Ramesh, *A 3d mechanistic model for brittle materials containing evolving flaw distributions under dynamic multiaxial loading*, Journal of the Mechanics and Physics of Solids, 78 (2015), pp. 269–297.

[64] J. Hudson, T. Pointer, and E. Liu, *Effective-medium theories for fluid-saturated materials with aligned cracks*, Geophysical Prospecting, 49 (2001), pp. 509–522.

[65] F. Huq, R. Brannon, and L. Graham-Brady, *An efficient binning scheme with application to statistical crack mechanics*, International Journal for Numerical Methods in Engineering, 105 (2016), pp. 33–62.

[66] M. Jeyakumaran and J. Rudnicki, *The sliding wing crack?again!*, Geophysical research letters, 22 (1995), pp. 2901–2904.

[67] T. Jiang, J. Shao, W. Xu, and C. Zhou, *Experimental investigation and micromechanical analysis of damage and permeability variation in brittle rocks*, International Journal of Rock Mechanics and Mining Sciences, 47 (2010), pp. 703–713.

[68] J. Ju and X. Lee, *Micromechanical damage models for brittle solids. part i: tensile loadings*, Journal of Engineering Mechanics, 117 (1991), pp. 1495–1514.

[69] M. Kachanov, *Elastic solids with many cracks and related problems*, Advances in applied mechanics, 30 (1993), pp. 259–445.

[70] M. L. Kachanov, *A microcrack model of rock inelasticity part i: Frictional sliding on microcracks*, Mechanics of Materials, 1 (1982), pp. 19–27.

[71] D. M. d. l. P. J. Kaser, M. and H. Igel, *An arbitrary high order discontinuous galerkin method for elastic waves on un- structured meshes iii: viscoelastic attenuation*, Geophys. J. Int., 168 (2007), pp. 224–242.

[72] H. V. Kaser, M. and J. de la Puente, *Quantitative accuracy analysis of the discontinuous galerkin method for seismic wave propagation*, Geophysical Journal International, 173 (2008), pp. 990–999.

[73] C. Katcoff and L. Graham-Brady, *Modeling dynamic brittle behavior of materials with circular flaws or pores*, International Journal of Solids and Structures, 51 (2014), pp. 754–766.

[74] B. Kostrov, *Unsteady propagation of longitudinal shear cracks*, Journal of applied Mathematics and Mechanics, 30 (1966), pp. 1241–1248.

[75] D. Krajcinovic, *Damage Mechanics*, North-Holland Series in Applied Mathematics and Mechanics, Elsevier Science, 1996.

[76] T. A. Laursen, M. A. Puso, and J. Sanders, *Mortar contact formulations for deformable–deformable contact: past contributions and new extensions for enriched and embedded interface formulations*, Computer methods in applied mechanics and engineering, 205 (2012), pp. 3–15.

[77] P. Lesaint, *Finite element methods for symmetric hyperbolic equations*, Numerische Mathematik, 21 (1973), pp. 244–255.

[78] P. Lesaint and P.-A. Raviart, *On a finite element method for solving the neutron transport equation*, Mathematical aspects of finite elements in partial differential equations, (1974), pp. 89–123.

[79] A. Lew, P. Neff, D. Sulsky, and M. Ortiz, *Optimal bv estimates for a discontinuous galerkin method for linear elasticity*, Applied Mathematics Research Express, 2004 (2004), pp. 73–106.

[80] J. Liu and L. Graham-Brady, *Effective anisotropic compliance relationships for wing-cracked brittle materials under compression*, International Journal of Solids and Structures, 100 (2016), pp. 151–168.

[81] R. Liu, M. F. Wheeler, and I. Yotov, *On the spatial formulation of discontinuous galerkin methods for finite elastoplasticity*, Computer Methods in Applied Mechanics and Engineering, 253 (2013), pp. 219–236.

[82] J. Martins and J. Oden, *A numerical analysis of a class of problems in elastodynamics with friction*, Computer Methods in Applied Mechanics and Engineering, 40 (1983), pp. 327–360.

[83] A. Masud, T. J. Truster, and L. A. Bergman, *A unified formulation for interface coupling and frictional contact modeling with embedded error estimation*, International Journal for Numerical Methods in Engineering, 92 (2012), pp. 141–177.

[84] G. Mavko, T. Mukerji, and J. Dvorkin, *The Rock Physics Handbook: Tools for Seismic Analysis of Porous Media*, Cambridge University Press, 2009.

[85] T. McDevitt and T. Laursen, *A mortar-finite element formulation for frictional contact problems*, International Journal for Numerical Methods in Engineering, 48 (2000), pp. 1525–1547.

[86] R. McLaughlin, *A study of the differential scheme for composite materials*, International Journal of Engineering Science, 15 (1977), pp. 237–244.

[87] T. Mori and K. Tanaka, *Average stress in matrix and average elastic energy of materials with misfitting inclusions*, Acta metallurgica, 21 (1973), pp. 571–574.

[88] T. Mura, *Micromechanics of Defects in Solids*, Mechanics of Elastic and Inelastic Solids, Springer Netherlands, 1987.

[89] S. Nemat-Nasser and M. Hori, *Micromechanics: Overall Properties of Heterogeneous Materials*, North-Holland Series in Applied Mathematics and Mechanics, Elsevier Science, 2013.

[90] S. Nemat-Nasser and H. Horii, *Compression-induced nonplanar crack extension with application to splitting, exfoliation, and rockburst*, Journal of Geophysical Research: Solid Earth, 87 (1982), pp. 6805–6821.

[91] V.-D. Nguyen, G. Becker, and L. Noels, *Multiscale computational homogenization methods with a gradient enhanced scheme based on the discontinuous galerkin formulation*, Computer Methods in Applied Mechanics and Engineering, 260 (2013), pp. 63–77.

[92] J. Nitsche, *On dirichlet problems using subspaces with nearly zero boundary conditions*, The mathematical foundations of the finite element method with applications to partial differential equations, (1972), pp. 603–627.

[93] L. Noels and R. Radovitzky, *A general discontinuous galerkin method for finite hyperelasticity. formulation and numerical applications*, International Journal for Numerical Methods in Engineering, 68 (2006), pp. 64–97.

[94] J. Oden and J. Martins, *Models and computational methods for dynamic friction phenomena*, Computer methods in applied mechanics and engineering, 52 (1985), pp. 527–634.

[95] B. Paliwal and K. Ramesh, *An interacting micro-crack damage model for failure of brittle materials under compression*, Journal of the Mechanics and Physics of Solids, 56 (2008), pp. 896–923.

[96] V. Pensée and D. Kondo, *Une analyse micromécanique 3-d de l'endommagement par mésofissuration*, Comptes Rendus de l'Académie des Sciences-Series IIB-Mechanics, 329 (2001), pp. 271–276.

[97] V. Pensee and D. Kondo, *Micromechanics of anisotropic brittle damage: comparative analysis between a stress based and a strain based formulation*, Mechanics of materials, 35 (2003), pp. 747–761.

[98] V. Pensée, D. Kondo, and L. Dormieux, *Micromechanical analysis of anisotropic damage in brittle materials*, Journal of Engineering Mechanics, 128 (2002), pp. 889–897.

[99] G. Pietrzak and A. Curnier, *Large deformation frictional contact mechanics: continuum formulation and augmented lagrangian treatment*, Computer Methods in Applied Mechanics and Engineering, 177 (1999), pp. 351–381.

[100] A. Popp and W. Wall, *Dual mortar methods for computational contact mechanics–overview and recent developments*, GAMM-Mitteilungen, 37 (2014), pp. 66–84.

[101] T. Poston and I. Stewart, *Catastrophe Theory and Its Applications*, Dover Publications, 2014.

[102] W. H. Reed and T. R. Hill., *Triangular mesh methods for the neutron transport equation*, Tech. Rep. LA-UR-73-0479, Los Alamos Scientific Laboratory, 1973.

[103] V. Renaud, D. Kondo, and J. Henry, *Computations of effective moduli for microcracked materials: a boundary element approach*, Computational materials science, 5 (1996), pp. 227–237.

[104] E. H. Saenger, N. Gold, and S. A. Shapiro, *Modeling the propagation of elastic waves using a modified finite-difference grid*, Wave motion, 31 (2000), pp. 77–92.

[105] E. H. Saenger, O. S. Krüger, and S. A. Shapiro, *Effective elastic properties of randomly fractured soils: 3d numerical experiments*, Geophysical Prospecting, 52 (2004), pp. 183–195.

[106] E. H. Saenger and S. A. Shapiro, *Effective velocities in fractured media: A numerical study using the rotated staggered finite-difference grid*, Geophysical Prospecting, 50 (2002), pp. 183–194.

[107] M. Schoenberg, *Elastic wave behavior across linear slip interfaces*, The Journal of the Acoustical Society of America, 68 (1980), pp. 1516–1521.

[108] M. Schoenberg and C. M. Sayers, *Seismic anisotropy of fractured rock*, Geophysics, 60 (1995), pp. 204–211.

[109] A. Schubnel and Y. Guéguen, *Dispersion and anisotropy of elastic waves in cracked rocks*, Journal of Geophysical Research: Solid Earth, 108 (2003).

[110] J. C. Simo and T. Laursen, *An augmented lagrangian treatment of contact problems involving friction*, Computers & Structures, 42 (1992), pp. 97–116.

[111] S. Sitzmann, K. Willner, and B. I. Wohlmuth, *A dual lagrange method for contact problems with regularized frictional contact conditions: Modelling micro slip*, Computer Methods in Applied Mechanics and Engineering, 285 (2015), pp. 468–487.

[112] K. Teferra and L. Graham-Brady, *Tessellation growth models for polycrystalline microstructures*, Computational Materials Science, 102 (2015), pp. 57–67.

[113] I. Temizer, *A mixed formulation of mortar-based contact with friction*, Computer Methods in Applied Mechanics and Engineering, 255 (2013), pp. 183–195.

[114] A. Ten Eyck and A. Lew, *Discontinuous galerkin methods for non-linear elasticity*, International Journal for Numerical Methods in Engineering, 67 (2006), pp. 1204–1243.

[115] L. Thomsen, *Elastic anisotropy due to aligned cracks in porous rock*, Geophysical Prospecting, 43 (1995), pp. 805–829.

[116] I. Toulopoulos and J. Ekaterinaris, *High-order discontinuous galerkin discretizations for computational aeroacoustics in complex domains*, AIAA J., 44 (2006), pp. 502–511.

[117] T. J. Truster, P. Chen, and A. Masud, *On the algorithmic and implementational aspects of a discontinuous galerkin method at finite strains*, Computers & Mathematics with Applications, 70 (2015), pp. 1266–1289.

[118] T. J. Truster and A. Masud, *A discontinuous/continuous galerkin method for modeling of interphase damage in fibrous composite systems*, Computational Mechanics, 52 (2013), pp. 499–514.

[119] ——, *Primal interface formulation for coupling multiple pdes: a consistent derivation via the variational multiscale method*, Computer Methods in Applied Mechanics and Engineering, 268 (2014), pp. 194–224.

[120] ——, *Discontinuous galerkin method for frictional interface dynamics*, Journal of Engineering Mechanics, 142 (2016), p. 04016084.

[121] G. B. van Baren, W. A. Mulder, and G. C. Herman, *Finite-difference modeling of scalar-wave propagation in cracked media*, Geophysics, 66 (2001), pp. 267–276.

[122] J. Virieux, *P-sv wave propagation in heterogeneous media: Velocity-stress finite-difference method*, Geophysics, 51 (1986), pp. 889–901.

[123] S. Vlastos, E. Liu, I. Main, and X.-Y. Li, *Numerical simulation of wave propagation in media with discrete distributions of fractures: effects of fracture sizes and spatial distributions*, Geophysical Journal International, 152 (2003), pp. 649–668.

[124] M. F. Wheeler, *An elliptic collocation-finite element method with interior penalties*, SIAM Journal on Numerical Analysis, 15 (1978), pp. 152–161.

[125] P. Wriggers, *Finite element algorithms for contact problems*, Archives of Computational Methods in Engineering, 2 (1995), pp. 1–49.

[126] P. Wriggers and G. Zavarise, *A formulation for frictionless contact problems using a weak form introduced by nitsche*, Computational Mechanics, 41 (2008), pp. 407–420.

[127] S.-W. Yu and X.-Q. Feng, *A micromechanics-based damage model for microcrack-weakened brittle solids*, Mechanics of Materials, 20 (1995), pp. 59–76.

[128] G. Zavarise, P. Wriggers, and B. Schrefler, *A method for solving contact problems*, International Journal for Numerical Methods in Engineering, 42 (1998), pp. 473–498.

[129] J. Zhang, *Elastic wave modeling in fractured media with an explicit approach*, Geophysics, 70 (2005), pp. T75–T85.

[130] Q. Zhu, D. Kondo, J. Shao, and V. Pensee, *Micromechanical modelling of anisotropic damage in brittle rocks and application*, International Journal of Rock Mechanics and Mining Sciences, 45 (2008), pp. 467–477.

[131] Q.-Z. Zhu, D. Kondo, and J. Shao, *Micromechanical analysis of coupling between anisotropic damage and friction in quasi brittle materials: role of the homogenization scheme*, International Journal of Solids and Structures, 45 (2008), pp. 1385–1405.

[132] Q.-z. Zhu, J.-f. Shao, and D. Kondo, *A micromechanics-based non-local anisotropic model for unilateral damage in brittle materials*, Comptes Rendus Mécanique, 336 (2008), pp. 320–328.

[133] J. Zinszner, B. Erzar, P. Forquin, and E. Buzaud, *Dynamic fragmentation of an alumina ceramic subjected to shockless spalling: an experimental and numerical study*, J. Mech. Phys. Solids, 85 (2015), pp. 112–127.

Part IV

Appendix

CHAPTER 17

EFFECTIVE ELASTICITY

17.1 The non-interacting cracks method

In the "non-interacting cracks method" (NIC) (see Gambarotta and Lagomarsino [52] and Kachanov [69] to cite only some) the strain $\boldsymbol{\varepsilon}$ will be expressed as the sum

$$\boldsymbol{\varepsilon} = \boldsymbol{\mathcal{A}}_0 \boldsymbol{\sigma} + \boldsymbol{\varepsilon}_n + \boldsymbol{\varepsilon}_T, \tag{17.1}$$

of the mean strain in the elastic matrix ($\boldsymbol{\mathcal{A}}_0 = \dfrac{1+\nu_0}{E_0}\boldsymbol{I}_4 - \dfrac{\nu}{E_0}\boldsymbol{I}_2 \otimes \boldsymbol{I}_2$, with E_0 the Young modulus and ν_0 the Poisson ratio) and $\boldsymbol{\varepsilon}_n, \boldsymbol{\varepsilon}_T$ representing the contributions of the normal and tangential discontinuities across the micro-crack faces:

$$\boldsymbol{\varepsilon}_n = C_n \sum_{i=1}^{N} \rho_i [\sigma_n^i - p]_+ \boldsymbol{n}_i \otimes \boldsymbol{n}_i, \quad \boldsymbol{\varepsilon}_T = C_T \sum_{i=1}^{N} \rho_i \left(\boldsymbol{\sigma}_T^i - \boldsymbol{f}^i\right) \otimes^S \boldsymbol{n}_i, \tag{17.2}$$

where $[x]_+ = 1/2(x+|x|)$ is the positive part and $\boldsymbol{a} \otimes^S \boldsymbol{b} = (\boldsymbol{a}\otimes\boldsymbol{b} + \boldsymbol{b}\otimes\boldsymbol{a})/2$ is the symmetrize tensorial product. Here σ_n^i and $\boldsymbol{\sigma}_T^i$ represent the normal and tangential decomposition of the stress vector ($\boldsymbol{\sigma}\boldsymbol{n}_i = \sigma_n^i \boldsymbol{n}_i + \boldsymbol{\sigma}_T^i$), $\boldsymbol{f}^i = \boldsymbol{f}(\boldsymbol{\sigma}, \boldsymbol{n}_i)$ is the Coulomb frictional force acting on the micro-crack faces

$$\boldsymbol{f}^i = \boldsymbol{\sigma}_T^i, \quad \text{if} \quad |\boldsymbol{\sigma}_T^i| \le \mu[-\sigma_n^i]_+, \qquad \text{else} \qquad \boldsymbol{f}^i = \frac{\mu[-\sigma_n^i]_+}{|\boldsymbol{\sigma}_T^i|}\boldsymbol{\sigma}_T^i,$$

	3-D	2-D plain stress	2-D plain strain	2-D anti-plain
C_n	$\frac{16(1-\nu_0^2)}{3E_0}$	$\frac{\pi}{E_0}$	$\frac{\pi(1-\nu_0^2)}{E_0}$	0
C_T	$\frac{32(1-\nu_0^2)}{3E_0(2-\nu_0)}$	$\frac{\pi}{E_0}$	$\frac{\pi(1-\nu_0^2)}{E_0}$	$\frac{2\pi(1+\nu_0)}{E_0}$

Table 17.1: Compliance coefficients C_n, C_T in different configurations.

and the two compliance parameters C_n, C_T have to be chosen following the choice of the configuration (see Table 17.1). Note that, due to the unilateral contact with friction on the micro-cracks faces, the above equation is nonlinear and not differentiable.

17.2 One family of parallel cracks

Let us consider here materials composed of an isotropic solid matrix (elastic coefficients E_0, G_0, ν_0) and one family ($N = 1$) of parallel non-frictional circular cracks of normal $\boldsymbol{n} = (1, 0, 0)$. Different models of effective elasticity will give the expressions of the Young modulus $E_1(\rho)$ acting in the direction of the normal and the shear modulus $G_{12}(\rho)$.

For the *non-interacting cracks method (NIC)*, the effective elastic coefficients (see [69]) in 3-D are

$$E_1(\rho) = E_0 \frac{1}{1 + \rho \frac{16(1+\nu_0)}{3}}, \quad \rho < \rho_{max} = +\infty \tag{17.3}$$

$$G_{12}(\rho) = G_0 \frac{1}{1 + \rho \frac{16(1-\nu_0^2)}{3(2-\nu_0)}}, \quad \rho < \rho_{max} = +\infty \tag{17.4}$$

while in 2-D we have

$$E_1'(\rho) = E_0 \frac{1}{1 + 2\pi\rho}, \quad \rho < \rho_{max} = +\infty \tag{17.5}$$

$$G_{12}(\rho) = G_0 \frac{1}{1 + 2\pi\rho \frac{G_0}{E_0'}}, \quad \rho < \rho_{max} = +\infty. \tag{17.6}$$

To model the crack interactions on a given crack family one can use the *self-consistent schemes* (SC), the effective elastic coefficients in 2-D were obtained by Hoening [61] as a

solution of the following nonlinear system of equations

$$\begin{cases} \dfrac{1}{E_1(\rho)} = \dfrac{1}{E_0} + \dfrac{2\pi\rho}{\sqrt{E_0 E_1(\rho)}}\sqrt{\left(\dfrac{E_0}{E_1(\rho)}\right)^{1/2} + \dfrac{E_1(\rho)}{2G_{12}(\rho)} - \nu_0}, \\ \dfrac{1}{G_{12}(\rho)} = \dfrac{1}{G_{12}(\rho)} + \dfrac{2\pi\rho}{E_0}\sqrt{\left(\dfrac{E_0}{E_1(\rho)}\right)^{1/2} + \dfrac{E_1(\rho)}{2G_{12}(\rho)} - \nu_0}. \end{cases} \tag{17.7}$$

Another way to model the crack interactions is to increase the crack density in small steps and to recalculate the effective matrix at each step, called *differential schemes* (DS) developed by MacLaughlin [86] and Hashin [58]). In 2-D the expression of the Young modulus (see [69]) is

$$E_1'(\rho) = E_0' \exp(-2\pi\rho).$$

The effective properties of cracked materials could also be obtained by following the method based on the *Eshelby inhomogeneous inclusion* solution (see Eshelby [45, 44], Mura [88]). Ponte-Castaneda and Willis [24] have improved the existing Eshelby-based inclusion models by introducing a new tensor which accounts for the spatial distribution of inclusions. This method was adapted by Zhu et al [131, 130, 132] to get effective properties of cracked materials and following the homogenization scheme they get (see [131]) for the 3-D configuration:

$$E_1(\rho) = E_0 \frac{3(1-2\nu_0) - 16\rho(1-\nu_0)^2}{3(1-2\nu_0) - 32\rho\nu_0^2(1-\nu_0)}, \quad \rho < \rho_{max} = \frac{3(1-2\nu_0)}{16(1-\nu_0)^2}$$

$$G_{12}(\rho) = G_0(1 - \rho\frac{16(1-\nu_0)}{3(2-[v-u]_0)}, \quad \rho < \rho_{max} = \frac{3(1-2\nu_0)}{16(1-\nu_0)}$$

for the *dilute scheme*,

$$E_1(\rho) = E_0' \frac{3(1-2\nu_0)}{16\rho(1-\nu_0-\nu_0^2)(1-\nu_0) + 3(1-2\nu_0)}, \quad \rho < \rho_{max} = +\infty$$

$$G_{12}(\rho) = G_0 \frac{3(2-\nu_0)}{3(2-\nu_0) + 16\rho(1-\nu_0)}, \quad \rho < \rho_{max} = +\infty$$

for Mori-Tanaka [87] scheme and

$$E_1(\rho) = E_0 \frac{45(1-2\nu_0) + 16\rho(7-14\nu_0+15\nu_0^2) - 240\rho(1-\nu_0)^2}{45(1-2\nu_0) + 16\rho(7-14\nu_0+15\nu_0^2) - 480\rho(1-\nu_0)\nu_0^2}, \quad \rho < \rho_{max} = \frac{45}{128}$$

$$G_{12}(\rho) = G_0 \frac{45(2-\nu_0) - 16\rho(7-5\nu_0)}{45(2-\nu_0) + 32\rho(4-5\nu_0)}, \quad \rho < \rho_{max} = \frac{45(2-\nu_0)}{16(7-5\nu_0)}$$

for Ponte-Casteneda and Willis [24] scheme.

17.3 Isotropic (random) orientated micro-cracks

Let us consider here materials composed of an isotropic solid matrix (elastic coefficients E_0, G_0, ν_0) with isotropic (random) orientated micro-cracks non-frictional circular cracks ($N = 1$). Different models of effective elasticity will give the expressions of the Young modulus $E(\rho)$, the shear modulus $G(\rho)$ and of the Poisson ratio $\nu(\rho)$ of the effective isotropic solid.

For the *non-interacting cracks method (NIC)*, the effective elastic coefficients (see [69]) in 3-D are

$$E(\rho) = E_0 \frac{1}{1 + \rho \dfrac{16(1-\nu_0^2(1-3\nu_0/10))}{9(1-\nu_0/2)}} \tag{17.8}$$

$$G(\rho) = G_0 \frac{1}{1 + \rho \dfrac{16(1-\nu_0)(1-\nu_0)(1-\nu_0/10)}{9(1-\nu_0/2)}} \tag{17.9}$$

$$\nu(\rho) = \nu \frac{E}{E_0} \left[1 + \rho \frac{8(1-\nu^2)}{45(1-\nu_0/2)}\right] \tag{17.10}$$

while in 2-D we have

$$E'(\rho) = E'_0 \frac{1}{1+\pi\rho}, \quad \rho < \rho_{max} = +\infty \tag{17.11}$$

$$\nu(\rho) = \nu_0 \frac{1}{1+\pi\rho}, \quad \rho < \rho_{max} = +\infty. \tag{17.12}$$

To model the crack interactions on a given crack family one can use the *self-consistent schemes* (SC), the effective elastic coefficients were obtained by by Budiansky and O'Connell [22] for random crack orientations as a solution of the following nonlinear system of equations

$$E(\rho) = E_0 \left[1 - \rho \frac{16(1-\nu^2)(10-3\nu)}{45(2-\nu)}\right] \tag{17.13}$$

$$G(\rho) = G_0 \left[1 - \rho \frac{32(1-\nu)(5-\nu)}{45(2-\nu)}\right] \tag{17.14}$$

$$\rho = \frac{45(\nu_0 - \nu)(2-\nu)}{16(1-\nu^2)(10\nu_0 - \nu(1+3\nu))} \tag{17.15}$$

in 3-D and

$$E(\rho) = E_0 \left[1 + \rho \frac{\pi^2}{30}(1+\nu)(5-4\nu)\right] \tag{17.16}$$

$$G(\rho) = G_0 \left[1 - \rho \frac{\pi^2}{60}(10 - 7\nu(\rho))\right] \tag{17.17}$$

$$\rho = \frac{60(\nu_0 - \nu)}{\pi^2(1+\nu)(10\nu_0 - \nu(1+8\nu_0))} \tag{17.18}$$

in 2-D.

CHAPTER 18

DAMAGE CRITERIA

18.1 Quasi-static processes

For not interacting and self similar micro-cracks of radius/length $l = l(\rho)$ and normal $\boldsymbol{n}$ under the stress far field $\boldsymbol{\sigma}$ (see Figure 18.1) the Griffith theory gives the following criterion for crack growth:

$$\mathcal{K}(\rho, \boldsymbol{\sigma}) = \frac{K(l(\rho), \boldsymbol{\sigma})}{K_c} - 1, \tag{18.1}$$

where K is the stress intensity factor (SIF) and K_c is the critical stress intensity factor. For instance $K(l, \boldsymbol{\sigma}) = K^I(l, \boldsymbol{\sigma})$ in mode I, $K(l, \boldsymbol{\sigma}) = K^{II}(l, \boldsymbol{\sigma})$ in mode II and $K(l, \boldsymbol{\sigma}) = K^{II}(l, \boldsymbol{\sigma})$ and $K(l, \boldsymbol{\sigma}) = K^{III}(l, \boldsymbol{\sigma})$ in mode III (see Table 18.1). The stress intensity factor depends on the stress through the normal and tangential stresses σ_n and $\boldsymbol{\sigma}_T$ ($\boldsymbol{\sigma}\boldsymbol{n}_i = \sigma_n \boldsymbol{n} + \boldsymbol{\sigma}_T$) and the Coulomb frictional force $\boldsymbol{f} = \boldsymbol{f}(\boldsymbol{\sigma}, \boldsymbol{n})$ acting on the crack faces

$$\boldsymbol{f} = \boldsymbol{\sigma}_T, \quad \text{if} \quad |\boldsymbol{\sigma}_T| \leq \mu[-\sigma_n]_+, \qquad \text{else} \qquad \boldsymbol{f}^i = \frac{\mu[-\sigma_n]_+}{|\boldsymbol{\sigma}_T|}\boldsymbol{\sigma}_T.$$

For the mixed mode the fracture criterion (see for instance Ju and Lee [68] and Yu and Feng [127]) reads

$$\mathcal{K}(\rho, \boldsymbol{\sigma}) = \sqrt{\left[\frac{K^I(l(\rho), \boldsymbol{\sigma})}{K_c^I}\right]^2 + \left[\frac{K^{II}(l(\rho), \boldsymbol{\sigma}))}{K_c^{II}}\right]} - 1. \tag{18.2}$$

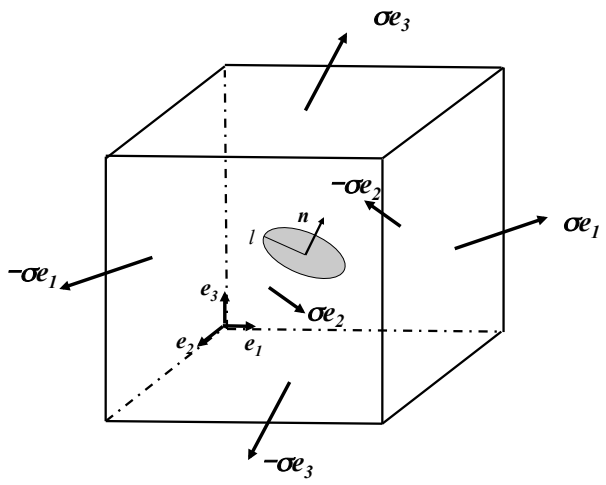

Figure 18.1: Schematic representation of a micro-crack of radius/length $l = l(\rho)$ and normal $\boldsymbol{n}$ under the stress far field $\boldsymbol{\sigma}$.

$K^I(l,\boldsymbol{\sigma})$ in 3-D	$K^I(l,\boldsymbol{\sigma})$ in 2D	$K^{II}(l,\boldsymbol{\sigma})$ in 2D	$K^{III}(l,\boldsymbol{\sigma})$
$\frac{\sqrt{2l}}{\pi}[\sigma_n]_+$	$\sqrt{\pi l}[\sigma_n]_+$	$\sqrt{\pi l}\,[\lvert\boldsymbol{\sigma}_T\rvert - \mu[-\sigma_n]_+]_+$	$\sqrt{\pi l}\,[\lvert\boldsymbol{\sigma}_T\rvert - \mu[-\sigma_n]_+]_+$

Table 18.1: The (static) stress intensity factors in different configurations.

When the micro-cracks propagate they can be arrested by energy barriers (or grains) with higher strength K_c. If the stress level is high enough the arrested micro-cracks could also propagate and pass the energy barriers till they are arrested by a higher barriers, and so on. A simple way to model that is to let the critical stress intensity factor K_c depending on the micro-crack radius/length l, i.e.

$$K_c = K_c(l).$$

18.2 Wing cracks modeling

In tension a single crack grows unstably, while in compression a population of small cracks extends stably, each growing longer as the stress is raised, until their length is comparable with their spacing when they interact. Then an instability develops, and the sample fails. To describe the geometry of a wing crack let us follow [7] and for the sake of the simplicity

let us analyze only the two dimensional case. We consider first the case of an isolated crack of normal $\boldsymbol{n}$ which contain an initial inclined flaw of half length $2a$, normal $\boldsymbol{n}^*$ and tangent $\boldsymbol{\tau}^*$ (we take the angle between $\boldsymbol{n}$ and $\boldsymbol{n}^*$ to be $\pi/4$) as in Figure 18.2 . In this case the dependence $\rho(l)$ of the crack density parameter ρ upon the wing crack half length l have to be replaced by

$$\rho^*(l) = \rho(l + a/\sqrt{2}), \quad l^*(\rho) = l(\rho) - a/\sqrt{2}.$$

Using the above expression of the crack density parameter one can use one of the effective elasticity formula (see the previous chapter) for describing the dependence of the elastic coefficients upon the damage. Moreover, more precise effective anisotropic compliance relationships for wing-cracked brittle materials under compression was obtained by Liu and Graham-Brady [80].

As it follows from Ashby and Sammis [7] the force acting at the midpoint of the inclined cracks produces a mode I stress intensity at the tips of their wing cracks and the mode I stress intensity factor K^I reads

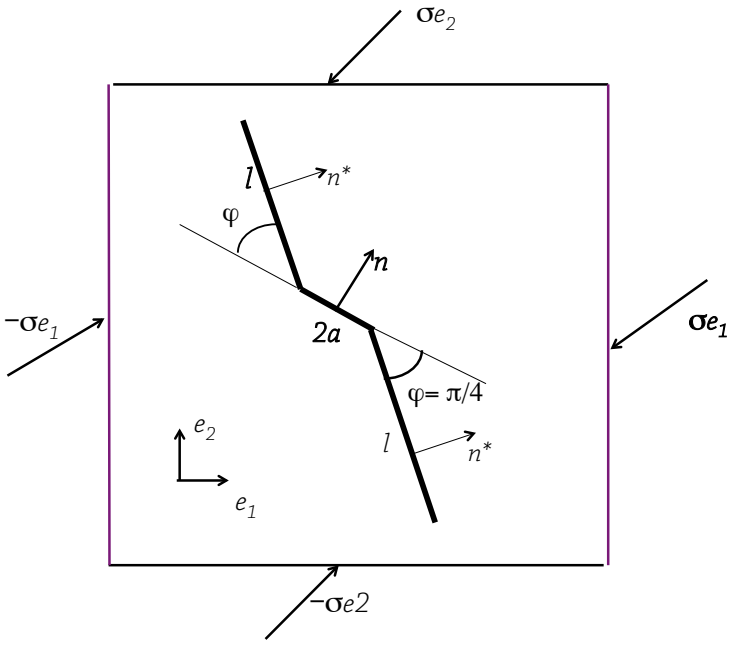

Figure 18.2: Schematic representation of a 2D wing micro-crack of length $l = l^*(\rho)$ and normal $\boldsymbol{n}^*$ under the stress far field $\boldsymbol{\sigma}$.

$$K(l,\boldsymbol{\sigma}) = \frac{a\left[A(\mu)(|\boldsymbol{\sigma}_{T^*}| - \sigma_{n^*}) + B(\mu)(|\boldsymbol{\sigma}_{T^*}| + \sigma_{n^*})\right]}{\sqrt{\pi(l+\beta a)}} + \sigma_{n^*}\sqrt{\pi l}, \tag{18.3}$$

where $\sigma_{n^*} = \boldsymbol{\sigma}\boldsymbol{n}^* \cdot \boldsymbol{n}^*$ and $\boldsymbol{\sigma}_{T^*} = \boldsymbol{\sigma}\boldsymbol{n}^* \cdot \boldsymbol{\tau}^*$ are the normal and tangential stress acting on the inclined flaw and the constants A, B are given by

$$A(\mu) = \frac{\pi\sqrt{\beta}}{\sqrt{3}}(\sqrt{1+\mu^2} - \mu), \quad B(\mu) = \frac{\pi\sqrt{\beta}}{\sqrt{3}}(\sqrt{1+\mu^2} + \mu).$$

The constant β was found to be $\beta = 0.1$ by comparing the equivalent expression for K in 2D with analytic and numerical results for small values of l. The second term is the reduction in K caused by the direct application of normal stress σ_n to the wing cracks. Notice that the criterion for the wing crack to nucleate is

$$K(0,\boldsymbol{\sigma}) = \frac{1}{\sqrt{\pi\beta}}\sqrt{a}\left[A(\mu)(\sigma_{T^*} - \sigma_{n^*}) + B(\mu)(\sigma_{T^*} + \sigma_{n^*})\right] = K_c^I.$$

Ashby and Sammis [7] estimated the interaction between the growing wing cracks in a global sense by requiring that the wedging force across any vertical section is balanced by an internal stress. This gives a more complicate expression of $K(l,\boldsymbol{\sigma})$.

Paliwal and Ramesh [95] and Hu et al. [63] have a different way to compute the stress intensity factor $K(l,\boldsymbol{\sigma})$ at the wing-crack tips, by using the superposition principle. The problem of a cracked inclusion in an effective medium subjected to remote uniform loading is decomposed into two problems: a homogeneous elliptical inclusion of the matrix material (without the crack) is embedded in the effective medium which is subjected to the same remote loading as in the original problem. The tractions $\boldsymbol{t}^r$ are the tractions on the planes corresponding to the cracks. In the second configuration only the crack surfaces are subjected to tractions $\boldsymbol{t}^{eff}$ that are derived from the first problem such that they satisfy the following traction boundary condition $\boldsymbol{\sigma}\boldsymbol{n}^* = \boldsymbol{t}^r + \boldsymbol{t}^{eff}$. The expression of the stress intensity factor $K(l,\boldsymbol{\sigma})$ is different from (18.3) but it has the same dependence on the wing crack length l.

To transform the anisotropic damage criterion (18.3), associated to parallel wing cracks, into an isotropic one, associated to an randomly orientated wing cracks, Deshpande and Evans [35] express (18.3) in terms of the stress invariants. For ease of numerical implementation they restrict their self to the first two invariants $\sigma_m = trace(\boldsymbol{\sigma})/3, \sigma_e = \sqrt{3\boldsymbol{\sigma}^D : \boldsymbol{\sigma}^D/2}$ (here $\boldsymbol{\sigma}^D$ is the stress deviator) of the stress tensor, neglecting the dependence on the third

stress invariant. They found the expression

$$K(l,\boldsymbol{\sigma}) = \sqrt{\pi a}c_1(l)\left[\left[(B(\mu)-A(\mu))c_2(l)+c_3(l)\right]\sigma_m + \left[c_2(l)(B(\mu)+A(\mu))+c_3(l)\right]\sigma_e/\sqrt{3}\right]_+, \tag{18.4}$$

where c_1, c_2 and c_3 are functions of l and a. Note that the above criterion has to be used in connection with an isotropic (random) orientated micro-cracks effective elasticity model.

18.3 Dynamic processes

The damage dynamic evolution could be deduced from the of the static criterion $\mathcal{K}(\rho,\boldsymbol{\sigma})$ (or equivalently from the SIF $K(l,\boldsymbol{\sigma})$). One way to do that is to introduce the "dynamic stress intensity factor" $K_d(l,\boldsymbol{\sigma},\dot{l})$ instead of the static stress intensity factor $K(l,\boldsymbol{\sigma})$ but to keep the same criterion $K_d(l,\boldsymbol{\sigma},\dot{l}) = K_c$ for the dynamic crack growth. For instance, in mode I the dynamic stress intensity factor of a growing crack, with an instantaneous speed $\dot{l}$, can be related to the static SIF through $K_d(l,\boldsymbol{\sigma},\dot{l}) = k(\dot{l})K(l,\boldsymbol{\sigma})$ (see Freund [49, 50]), where $k(\dot{l})$ is the universal function of the crack speed, representing the inertial effect on the crack growth. Deng and Nemat-Nasser [32] obtained a simplified approximate expression $k(\dot{l})$ in good accord with the computed solution $k(\dot{l}) = 2\dfrac{c_R-\dot{l}}{2c_R-\dot{l}}$ where c_R is the Rayleigh wave speed of the material. In mode III of the anti-plane configuration $k(\dot{l}) = \sqrt{1-\dfrac{\dot{l}}{c_S}}$ with c_S the S-wave speed. After some algebra one can find the expression of the micro-crack growth rate (3.5) with $c_m = c_R, \alpha = 1/2$ and $\varphi(x) = x$ in mode I, i.e.

$$\frac{d}{dt}l = c_R[\frac{\mathcal{K}(\rho(l),\boldsymbol{\sigma})}{\frac{1}{2}+\mathcal{K}(\rho(l),\boldsymbol{\sigma})}]_+, \tag{18.5}$$

and $c_m = c_S, \alpha = 1$ and $\varphi(x) = x$ in mode III, i.e.

$$\frac{d}{dt}l = c_S[\frac{\mathcal{K}(\rho(l),\boldsymbol{\sigma})}{1+\mathcal{K}(\rho(l),\boldsymbol{\sigma})}]_+, \tag{18.6}$$

The above expression of the micro-crack growth rate was obtained from the universal crack speed function by solving a self-similar dynamic crack growth problem under far-field uniform tension. It may be applicable for the case of compressive loading of a population of local tensile enclaves at the wing-crack tips. Paliwal and Ramesh [95] and Hu et al. [63]

assumed that a similar form of $k(\dot{l})$ exists for the wing-crack growth rate and they have considered (3.5) with $c_m = c_R/a, \alpha = 1/2$ and $\varphi(x) = x^\gamma$, i.e.

$$\frac{d}{dt}l = \frac{c_R}{a}[\frac{\mathcal{K}(\rho(l), \boldsymbol{\sigma})}{\frac{1}{2} + \mathcal{K}(\rho(l), \boldsymbol{\sigma})}]_+^\gamma, \tag{18.7}$$

where $a \geq 1$ and $\gamma > 0$ are fitting parameters characterizing the toughness-velocity relation.

The evolution law (3.5) has the advantage that it contains the quasi-static criterion for small growth rate, and it compatible with the quasi-static evolution, i.e. $\mathcal{L}(\rho, \boldsymbol{\sigma}) = 0$ for $\mathcal{K}(\rho, \boldsymbol{\sigma}) \leq 0$. But this compatibility can be done asymptotically by using a power law. For instance, for the wing-crack growth rate Deshpande and Evans [35] have considered

$$\frac{d}{dt}l = \min\left\{c_0(\mathcal{K}(\rho(l), \boldsymbol{\sigma}) + 1)^m, c_S\right\}, \tag{18.8}$$

with m a large rate sensitivity exponent ($m \in [10, 20]$) and c_0 the reference crack growth rate, to investigate the events occurring in the timescale when the dynamic effects on the stress intensity factor have subsided.

.

Modélisation Galerkin-discontinue de la propagation des ondes dans un milieu endommagé

Dans cette thèse on utilise une méthode de Galerkin discontinue (GD) pour modéliser la propagation des ondes dans un matériau endommagé. Deux modèles différents pour la description de l'endommagement ont été considérés. Dans la première partie de la thèse on utilise un modèle d'endommagent assez général, basé sur une modélisation micromécanique. Pour ce modèle on établit un critère de stabilité basé sur une densité critique de fissuration. On développe aussi une méthode numérique GD capable de capturer les instabilités au niveau microscopique. On construit une solution exacte pour analyser la précision de la méthode proposée. Plusieurs résultats numériques vont permettre d'analyser la propagation des ondes dans les configurations planes et anti-planes. Dans la deuxième parte de la thèse on étudie la propagation des ondes dans un milieux fissuré (microfissures en contact avec frottement). La méthode numérique développée utilise une technique GD et la méthode du Lagrangien augmenté. En utilisant cette méthode on a pu calculer numériquement la vitesse de propagation moyenne dans un matériau endommagé. On a pu comparer les résultats obtenus avec les formules analytiques obtenues avec des approches micromécaniques. Finalement, on a utilisé les calculs numériques pour étudier la propagation des ondes après un impact sur une plaque céramique pour les deux modèles mécaniques considérés.

Discontinuous Galerkin Modeling of Wave Propagation in Damaged Materials

A discontinuous Galerkin (DG) technique for modeling wave propagation in damaged (brittle) materials is developed in this thesis. Two different types of mechanical models for describing the damaged materials are considered. In the first part of the thesis general micro-mechanics based damage models were used. A critical crack density parameter, which distinguishes between stable and unstable behaviors, was computed. A new DG-numerical scheme able to capture the instabilities and a micro-scale time step were proposed. An exact solution is constructed and the accuracy of the numerical scheme was analyzed. The wave propagation in one dimensional and anti-plane configuration was analyzed through several numerical computations. In the second part of the thesis the wave propagation in cracked materials with a nonlinear micro-structure (micro-cracks in frictional contact) was investigated. The numerical scheme developed makes use of a DG-method and an augmented Lagrangian technique. The effective wave velocity in a damaged material, obtained by a numerical upscaling homogenization method, was compared with analytical formula of effective elasticity theory. The wave propagation (speed, amplitude and pulse length) in micro-cracked materials in complex configurations was studied. Finally, numerical computations of blast wave propagation, for the both models, illustrate the role played by the micro-cracks orientation and by the friction.

Keywords: discontinuous Galerkin, Lagrangian method, wave propagation, damage modeling, cracked solid, frictional contact, anisotropy, numerical homogenization